

AD-A259 745

PAGE

Form Approved  
OMB No. 0704-0189

(2)

Public reporting  
burden for this  
collection of  
information is  
estimated to  
average 1 hour  
per response, including the time for reviewing  
instructions, searching existing data sources,  
gathering the data, reviewing the collected  
information, and completing and reviewing  
the collection of information. Send comments  
regarding this burden estimate or any other  
aspect of this collection of information,  
including suggestions for reducing the  
burden, to Washington Headquarters  
Services, Directorate for Information  
Operations and Reports, 1215 Jefferson  
Avenue, Suite 1204, Arlington, VA 22202-4302,  
and Budget Paperwork Reduction Project (0704-0189),  
Washington, DC 20503.Public reporting  
burden for this  
collection of  
information is  
estimated to  
average 1 hour  
per response, including the time for reviewing  
instructions, searching existing data sources,  
gathering the data, reviewing the collected  
information, and completing and reviewing  
the collection of information. Send comments  
regarding this burden estimate or any other  
aspect of this collection of information,  
including suggestions for reducing the  
burden, to Washington Headquarters  
Services, Directorate for Information  
Operations and Reports, 1215 Jefferson  
Avenue, Suite 1204, Arlington, VA 22202-4302,  
and Budget Paperwork Reduction Project (0704-0189),  
Washington, DC 20503.

1. AGENCY USE ONLY (Leave blank)		2. REPORT DATE November 19, 1992		3. REPORT TYPE AND DATES COVERED Final Technical - 9/89 - 8/92	
4. TITLE AND SUBTITLE (U) Vortex Simulation of Turbulent Combustion				5. FUNDING NUMBERS PE - 61102F PR - 2308 SA - BS G - AFOSR 89-0491	
6. AUTHOR(S) Ahmed F. Ghoniem					
7. PERFORMING ORGANIZATION NAME(S) AND ADDRESS(ES) Massachusetts Institute of Technology 77 Massachusetts Avenue Cambridge, MA 02139				8. PERFORMING ORGANIZATION REPORT NUMBER AFOSR-TR-92-18	
9. SPONSORING, MONITORING AGENCY NAME(S) AND ADDRESS(ES) AFOSR/NA Building 410 Bolling AFB DC 20332-6448				10. SPONSORING/MONITORING AGENCY REPORT NUMBER 93-01514	
11. SUPPLEMENTARY NOTES 132/PP					
12a. DISTRIBUTION / AVAILABILITY STATEMENT Approved for public release; distribution is unlimited.				12b. DISTRIBUTION CODE	
13. ABSTRACT (Maximum 200 words) During the course of this work, we focused on the extension of the vortex method and the transport element method to three-dimensional flows and to reacting flow with finite heat release, density variation and volumetric expansion. Problems explored in detail include the formation of streamwise vorticity in uniform-density and variable density flow, the effect of this vorticity on the rate of product formation and the effect of volumetric expansion due to heat release on shear layer growth rate.					
14. SUBJECT TERMS Numerical Simulation, Turbulent Combustion, Vortex Methods				15. NUMBER OF PAGES 113	
				16. PRICE CODE	
17. SECURITY CLASSIFICATION OF REPORT Unclassified		18. SECURITY CLASSIFICATION OF THIS PAGE Unclassified		19. SECURITY CLASSIFICATION OF ABSTRACT Unclassified	
				20. LIMITATION OF ABSTR UL	

**FINAL REPORT**  
**ON**  
**VORTEX SIMULATION OF TURBULENT COMBUSTION**

**(AFOSR Grant No. 89-0491)**

**Principal Investigator: Ahmed F. Ghoniem**

**Department of Mechanical Engineering  
Massachusetts Institute of Technology  
Cambridge, MA 2139**

**SUMMARY**

During the course of this work, we focused on the extension of the vortex method and the transport element method to three-dimensional flows and to reacting flow with finite heat release, density variation and volumetric expansion. Problems explored in detail include the formation of streamwise vorticity in uniform-density and variable density flow, the effect of this vorticity on the rate of product formation and the effect of volumetric expansion due to heat release on shear layer growth rate.

# TABLE OF CONTENTS

PERSONNEL	3
PUBLICATIONS DURING 1989-1992	4
INVITED LECTURES AND SEMINARS	6
INTERACTIONS DURING 1989-1992	8
TECHNICAL REPORT	9
APPENDIX I	
APPENDIX II	
APPENDIX III	

DTIC QUALITY INSPECTED 5

Accession For	
NTIS GRA&I	<input checked="" type="checkbox"/>
DTIC TAB	<input type="checkbox"/>
Unannounced	<input type="checkbox"/>
Justification	
By	
Distribution/	
Availability Codes	
Dist	Avail and/or Special
A-1	

## PERSONNEL

Three graduate students, partially or fully supported by this grant, have completed their theses during the period of performance of this work. Their names and theses titles are:

1. Knio, Omar, "Three-dimensional Vortex Simulation of Reacting Shear Flow," Ph.D., June 1990.
2. Martins, L-F., "Vortex Computations of Axisymmetric High Reynolds Number Flows in Complex Models," Ph.D., June 1990.
3. Loprinzo, Anthony, "Numerical Simulation of Turbulent Jet Diffusion Flames," M.Sc., June 1990.

Three graduate students are currently pursuing their degrees under partial or full support of the new grant. The names and theses titles are:

1. Soteriou, M., "Compressible Vortex Methods for the Simulation of Reacting Flow and Combustion," Ph.D. thesis, expected date 1993.
2. Petrov, C., "Reaction Zone Models for the Simulation of Turbulent Combustion," M.Sc. thesis, expected date 1993.
3. Luu, V. "The Flow Structure and Turbulent Statistics in Complex Combustion Flow," Ph.D., starting date, September 1992.

Publications During 1989 - 1992.

1. Krishnan, A. and Ghoniem, A.F., "Numerical Simulation of the Structure of a Heated Jet in Cold Atmosphere," *the 27th AIAA Aerospace Sciences Meeting*, Reno, Nevada, January 9-12, 1989, **AIAA-89-0485**.
2. Ghoniem, A.F. and Krishnan, A., "Vorticity-combustion Interactions in a Turbulent Reacting Jet," *Dynamics of Deflagration and Reactive Systems: Flames*. Published in Progress in Astronautics and Aeronautics, **131**, ed. by Kuhl, Leyer, Borisov and Sirignano, 1991, pp. 237-256.
3. Ghoniem, A.F., Knio, O.M. and Heidarinejad, G., "The Structure of the Reaction Zone in a Reacting Shear Layer," *Dynamics of Deflagration and Reactive Systems: Flames*, Progress in Astronautics and Aeronautics, **131**, ed. by Kuhl, Leyer, Borisov and Sirignano, 1991, pp. 220-236.
4. Knio, O. M. and Ghoniem, A.F., "Numerical Study of a Three-dimensional Vortex Method," *J. Comput. Phys.*, **86**, 1990, pp. 75-106.
5. Knio, O.M. and Ghoniem, A.F., "Three-dimensional Vortex Simulation of Roll-up and Entrainment in a Shear Layer," *J. Comput Phys.*, **97**, pp. 172-223, Nov. 1991.
6. Ghoniem, A.F. and Heidarinejad, G., "Effect of Two-dimensional Shear Layer Dynamics on Mixing and Combustion at Low Heat Release," *Combust. Sci. and Tech.*, Vol. **72**, pp. 79-99, March 1990.
7. Ghoniem, A.F. and Heidarinejad, G., "Effect of Damkohler Number on the Reaction Zone in a Reacting Shear Layer," *Combust. Flame*, **83**, pp. 1-17, 1991.
8. Krishnan, A. and Ghoniem, A.F., "Simulation of the Roll-up and Mixing in Rayleigh-Taylor Flow using the Vortex/Transport Element Method," *J. Comput. Phys.*, **99**, 1992, pp. 1-27.
9. Ghoniem, A.F., "Vortex Simulation of Reacting Shear Flow," *Chapter 10 in Numerical Approaches to Combustion Modelling*, Ed by E. Oran and J. Boris, Progress in Aeronautics and Astronautics, Vol. **135**, 1991, pp. 305-348.
10. Ghoniem, A.F., "Numerical Simulation of Turbulent Combustion using Vortex Methods," *Fluid Mechanical Aspects of Combustion*, ed by M. Onofri and A. Resei, Pitman, 1991, pp. 305-326.
11. Knio, O.M. and Ghoniem, A.F., "Vortex Simulation of a Three-dimensional Reacting Shear Layer with Infinite-Rate Kinetics," *AIAA Journal*, **30**, January 1992.
11. Ghoniem, A.F., Knio, O.M. and Krishnan, A., "Lagrangian Simulation of the Initial Stages in a Reacting Jet," *The 23rd Symposium (International) on Combustion*, The Combustion Institute, Pittsburgh, PA, pp. 699-705, 1990.
13. Ghoniem, A.F., Knio, O.M. and Soteriou, M., "Manipulation of the Growth Rate of a Variable-Density, Spatially Developing Mixing Layer via External Modulation," presented at the *29th AIAA Aerospace Sciences Meeting*, Reno, NV, January 1991, **AIAA-91-0081**.

14. Soteriou, M.C., Knio, O.M., Ghoniem, A.F. and Cetegen, B.M., "Simulation of Flow-Combustion Interactions in a Spatially Developing Mixing Layer," presented at 30th Aerospace Sciences Meeting and Exhibit, January 6-9, 1992, Reno, Nevada, AIAA-92-0081.
15. Ghoniem, A.F. and Knio, O.M., "The Development and Application of the Transport Element Method to 3D Reacting Shear Layers," in *Vortex Dynamics and Vortex Methods*, ed. by C.R. Anderson and C. Greengard. *Lectures in Applied Mathematics*, Vol. 28, pp. 165-218, 1991.
16. Ghoniem, A.F., Soteriou, M.C. and Knio, O.M., "Effect of Steady and Periodic Strain on Unsteady Flamelet Combustion,": *Proceedings of the 24th Symposium (International) on Combustion*, July 5-10, 1992, Sydney, Australia, the Combustion Institute, Pittsburgh, PA, in press.
17. Knio, O.M. and Ghoniem, "The Three-dimensional Structure of Periodic Vorticity Layers under Non-symmetric Conditions," *J. Fluid Mech.*, in press, 1992.

The P.I. delivered a number of invited lectures and seminars in national and international conferences, universities, government laboratories and industrial organizations in the United States, Japan, Italy, France, Soviet Union, Australia, Norway, and Egypt. A partial list is presented below.

1. 1989, University of Rome Workshop on Fluid Mechanics of Combustion, a five lecture series (by invitation only).
2. 1989, Brown University (seminar).
3. 1989, National Institute of Standards and Technology.
4. 1989, Ford Motor Company Meeting on Flow Visualization (invited speaker).
5. 1990, University of California, Berkeley, CA (seminar).
6. 1990, California Institute of Technology, (seminar).
7. 1990, University of Southern California, (seminar).
8. 1990, NASA Ames Research Center, (seminar).
9. 1990, Sandia National Laboratories, (seminar).
10. 1990, Lawrence Livermore National Laboratories, (seminar).
11. 1990, Five-lecture condensed course, Nagoya University, Japan
12. 1990, Institute of Computational Fluid Dynamics, Tokyo, Japan, one-day professional course.
13. 1990, Honda Motor Co. Wako, Japan, (lecture).
14. 1990, Toyota Motor Co., Nagoya, Japan, (lecture).
15. 1990, Nissan Motor Co., Yokosaka, Japan, (lecture).
16. 1990, Mitsubishi Heavy Industries, Nagoya, Japan.(talk and discussion).
17. 1990, Mazda Motor Co., Yokohama, Japan, (talk and discussion).
18. 1990, American Math Society Meeting on Vortex Dynamics (by invitation only), Seattle.
19. 1990, SIAM National Meeting (invited talk), Chicago.
20. 1990, USSR academy of Sciences, Novosibirsk, USSR.
21. 1990, USSR academy of Sciences, Moscow, USSR.
22. 1991, Gas Research Institute, Chicago, IL.
23. 1991, National Center for Supercomputer Applications, Champaign, IL.
24. 1991, ASME Local Chapter, Boston, MA.

25. 1991, Northeastern University, Boston, MA.
26. 1991, Ch. Michelson Institute, Bergen, Norway.
27. 1992, Egyptian Environmental Affairs, (by invitation) Cairo, Egypt.
28. 1992, Carnegie Mellon University (seminar).
29. 1992, University of Massachusetts, Amherst (seminar).
30. 1992, Institute of Advanced Studies Workshop on Statistical Physics and Fluid Mechanics, Princeton, NJ (invited lecture).
31. 1992, University of Tennessee Space Institute Summer Course on High Angle of Attack and Unsteady Flow Phenomena (2 lectures).



## **INTERACTIONS WITH INDUSTRIAL AND GOVERNMENT LABORATORIES 1989-1992**

1. General Electric Research Center; with Dr. Sanjay Correa on the study of turbulent premixed flames and their instability.
2. Sandia National Laboratory; with Drs. R. Schefer, M. Namazian, and J. Kelly and their associates on the study of bluffbody diffusion flames.
3. Gas Research Institute; with Dr. J. Keizerle, on the numerical simulation of bluffbody flame burners and lean premixed combustion.
4. Ford Motor Company; with Drs. J.C. Kent and L. Ramai, on numerical simulation of flame propagation in enclosures and flow during intake processes.
5. Allison Gas Turbine; with Dr. H. Mongia, on numerical simulation of streamwise vortex structures in thrust augmentor sections.
6. Army Atmospheric Research Laboratory; with Mr. R. Meyers, on numerical simulations of flow over complex terrains.

## TECHNICAL REPORT

The transport element method has been extended to three dimensions to study the evolution of scalar fields in a flow with high vorticity concentration. The numerical scheme is based on following Lagrangian computational elements employed in the transport of vorticity and local scalar gradients, and is a direct generalization of the three-dimensional vortex element method. The numerical algorithms required to implement this scheme have been developed. Problems associated with severe distortion of the flow map due to the growth of perturbations were shown to cause difficulties including loss of numerical accuracy and resolution. Means to overcome these problems were developed and were shown to yield accurate solutions. Two grid-based and two grid-free methods for the computation of vorticity stretching were implemented, and the accuracy of the methods was investigated in light of numerical results. Solutions reveal the need for a careful treatment of the discrete form of the vorticity transport equation. The methods were applied to study the evolution of an initially two-dimensional shear layer, perturbed in the streamwise and spanwise direction, with attention focused on the role of the spanwise instability and how it enhances the rate of scalar entrainment into the large-scale structures which form as the streamwise instability develops. Two mechanisms, associated with the onset of three-dimensional instability, are found to be responsible for this enhancement: vorticity intensification within the large eddy core due to spanwise stretching which delays its collapse; and generation of transverse entrainment currents towards the eddy core due to the formation of streamwise vortex structures within the core and along the braids between neighboring cores. Preferential entrainment is detected along the spanwise direction due to the streamwise vorticity. Details of this work are presented in the paper on, "Three-dimensional Vortex Simulation of Rollup and Entrainment in a Shear Layer," by Omar M. Knio and Ahmed F. Ghoniem.<sup>(1)</sup>

Numerical simulations of a three-dimensional temporally-growing shear layer were then obtained at high Reynolds number for a variable density flow using the transport element method. Attention was focused on the effect of initial vorticity and density distributions on the interaction between the instability modes which lead to the generation and intensification of streamwise vorticity. Results showed that the three-dimensional instabilities evolve following the formation of concentrated spanwise vorticity cores. The deformation of each core along its span resembles the amplification of the transverse instability. The generation of vortex rods which wrap around individual cores while stretching between neighboring cores, suggested a mode similar to the Corcos instability. The instability modes leading to the formation of both

---

<sup>(1)</sup> Journal of Computational Physics, Vol 97, No. 1, November 1991.

structures, energized by the extensional strain generated by the cores, grow simultaneously. A similar series of events occurred in variable-density shear layers and in shear layers which start with an asymmetric vorticity distribution. Baroclinic vorticity generation in the variable-density layer lead to the formation of asymmetric cores whose volumetric composition is biased towards the lighter fluid. The structures are propelled, by their asymmetric vorticity distribution, in the direction of the heavier stream while their eccentric spinning forces an uneven stretching of the vortex rods. The origin of the asymmetry was established by comparing the results of variable density shear layers with the results of a shear layer with an initially asymmetric vorticity distribution in a uniform-density flow. The strong late-stage asymmetry exhibited by the former is not observed in the latter. Thus, baroclinic vorticity generation is responsible for the observed asymmetry. We also find that initially asymmetric vorticity distribution does not, as suggested before, lead to asymmetric spacing between the streamwise rods. It is concluded that the experimentally observed asymmetric spacing must arise after pairing. Details of this study are presented in this report as Appendix I.<sup>(2)</sup>

The three-dimensional transport element method was then extended to solve the conservation equations for reacting flow. The numerical scheme maintained its adaptive, Lagrangian nature in which computational effort is concentrated in zones of finite vorticity and chemical reaction. The method utilized an accurate discretization of vorticity and species concentrations among a number of spherically-symmetric reacting transport element and the advection of these elements along particle trajectories. We used the low Mach number approximation of combustion in open domains and restricted our attention to the case of diffusion flames with no heat release. A single-step, second-order, infinite-rate kinetics chemical reaction model was employed. The scheme was applied to study the effect of flow-induced instabilities on the reaction zone and product distribution in a temporal shear layer. Results were obtained in the high Peclet number regime for a wide range of Damkohler numbers. Changes in the reaction field were related to either the entrainment or the strain field associated with the saturation of the instabilities. With increasing Damkohler number, the structure of the reaction region changed from a distributed zone embedded within spanwise and streamwise vortices to a thin sheet surrounding their cores. However, the product concentration exhibited strong similarity to the vorticity, falling rapidly in regions where the vorticity magnitude was small. Variation of the Peclet number yields minor changes in the product distribution and in the reaction zone structure but strongly affects product formation rates. Details of this study are printed in this report as Appendix II.<sup>(3)</sup>

---

<sup>(2)</sup> The paper has been accepted for publication in the Journal of Fluid Mechanics.

<sup>(3)</sup> The paper has appeared in the AIAA Journal, Vol 30, pp. 105-116, January 1992.

Finally, the transport element method has been extended to simulate a spatially developing, reacting shear layer with unmixed reactants and finite heat release. In the case of a reacting flow, vorticity changes due to density variation, scalar gradients change due to the chemical reaction, and volumetric expansion adds an expansion field. Solutions were obtained for a forced shear layer at different Damkohler numbers and enthalpy of reaction to study the effect of combustion heat release rate on the development of the large scale structures. Forcing was used to ensure roll-up within the computational domain. We showed that heat release enlarges the size of the fundamental eddies, stretching their streamwise dimension and slightly reducing their cross stream dimension, while their overall size remains almost the same. Along with forcing at the fundamental and subharmonic frequencies, heat release increases/decreases the size of the in-phase/out-of-phase eddies. The non-uniform acceleration of the eddies in the streamwise direction causes their relative locations to deviate from that of a uniform-density layer and thus modifies the pairing process into a tearing/gulping process. Results also show that the enthalpy of reaction is more important than the reaction frequency factor in affecting the flow dynamics. For the same parameters, the variable-density layer grows slower than its uniform-density counterpart. Details of this work are presented in Appendix III in this report.<sup>(4)</sup>

---

<sup>(4)</sup> Presented at the 30th Aerospace Sciences Meeting and Exhibit, Jan 6-9, 1992, Reno, NV, AIAA-92-0081.

## APPENDIX I

# THE THREE-DIMENSIONAL STRUCTURE OF PERIODIC VORTICITY LAYERS UNDER NON-SYMMETRIC CONDITIONS

Omar M. Knio<sup>†</sup> and Ahmed F. Ghoniem  
Department of Mechanical Engineering  
Massachusetts Institute of Technology  
Cambridge, MA 02139

## ABSTRACT

Numerical simulations of a three-dimensional temporally-growing shear layer are obtained at high Reynolds number and zero Froude number using a vortex scheme modified for a variable density flow. Attention is focused on the effect of initial vorticity and density distributions on the interaction between instability modes which lead to the generation and intensification of streamwise vorticity. Results show that the three-dimensional instabilities evolve following the formation of concentrated spanwise vorticity *cores*. The deformation of each core along its span resembles the amplification of the translative instability. The generation of vortex *rods*, which wrap around individual cores while stretching between neighboring cores, suggest a mode similar to the Corcos instability. The instability modes leading to the formation of both structures, energized by the extensional strain generated by the cores, grow simultaneously. A similar series of events occurs in variable-density shear layers and in shear layers which start with an asymmetric vorticity distribution. Baroclinic vorticity generation in the variable-density layer leads to the formation of asymmetric cores whose volumetric composition is biased towards the lighter fluid. The structures are propelled, by their asymmetric vorticity distribution, in the direction of the heavier stream while their eccentric spinning forces an uneven stretching of the vortex rods. The origin of the asymmetry is established by comparing these with the results of a shear layer with an initially asymmetric vorticity distribution in a uniform-density flow. The strong late-stage asymmetry exhibited by the former is not observed in the latter. Thus, baroclinic vorticity generation is responsible for the observed asymmetry. We also find that initially asymmetric vorticity distribution does not, as suggested before, lead to asymmetric spacing between the streamwise rods. It is concluded that the experimentally observed asymmetric spacing must arise after pairing.

---

<sup>†</sup> Present Address: Department of Mechanical Engineering, The Johns Hopkins University, Baltimore, MD 21218

## 1. INTRODUCTION

The formation of large vortical structures has long been observed in free shear layers at high Reynolds numbers (Crow & Champagne, 1970; Brown & Roshko, 1974). Analysis of experimental results shows that the evolution of these structures and their mutual interactions, governed essentially by inviscid flow dynamics, play an important role in the growth of the layer, the distribution of turbulent statistics, scalar transport and mixing (Winant & Browand (1974); Ho & Huerre, 1984; Dimotakis, 1989; Hussain, 1986). Without external forcing, the early stages of the layer are dominated by 2D motion, where spanwise vortex structures are formed, followed by a transition to 3D motion. Within and after the transition region, the spanwise vortices are deformed, and secondary streamwise vortices are generated (Konrad, 1976; Breidenthal, 1981; Jimenez, 1983; Bernal, 1981). Experimental investigations yielded striking visualizations of the streamwise structures, and how they modify scalar transport (Jimenez, Cogollos & Bernal, 1985; Bernal & Roshko, 1986). In recent work, Lasheras, Cho & Maxworthy (1986) and Lasheras & Choi (1988) examined the possibility of manipulating the location of the "transition" region by 3D forcing (see also Breidenthal, 1980), thereby emphasizing the practical aspect of such studies.

The 3D response of vorticity layers is complex and determining the origin and shape of the secondary structures poses considerable difficulties to analytical studies. So far, a limited number of theoretical investigations have dealt with this problem. Pierrehumbert and Widnall (1982) used a periodic array of Stuart vortices to represent the spanwise eddies formed by the roll-up of the Kelvin-Helmholtz instability. The linear stability analysis of this configuration revealed the presence of a "translative" instability, which was then proposed as a possible mechanism leading to the formation of the observed secondary vortices in shear layers. Another mechanism, discovered by Corcos & Lin (1984) in their study of the stability of the layer by linearizing 3D perturbations around the evolving 2D flow (Lin & Corcos, 1984), was also suggested. They showed that, for sufficiently low diffusion (Neu, 1984), the strained streamwise vorticity is unstable, and the instability causes the redistribution of the latter into round, concentrated vortex rods. These streamwise rods lead to the generation of "mushroom" structures similar to those experimentally observed (Bernal & Roshko, 1986; Lasheras, Cho & Maxworthy, 1986; Lasheras & Choi, 1988). Manifestation of both instability mechanisms has been reported in experimental studies, however, the broad-band nature of the 3D modes predicted in both theories complicates the task of verifying their validity or determining flow conditions under which one mode dominates the other.

The 3D motion of shear layers has also been the subject of numerical investigations. Ashurst & Meiburg (1988) used a vortex filament scheme to compute the development of a temporal shear layer at high Reynolds number. The shear layer was modeled by a single desingularized vortex sheet or two vortex sheets of opposite sign. Results of both models showed

evidence of both the translative and the Corcos instability modes. When two sheets of opposite signs were used, an asymmetric distribution of streamwise vortices (Lasheras & Choi, 1988), was apparently reached through a non-linear interaction between two counter-rotating streamwise vortex rods, each originating in a distinct vorticity layer. While a similar asymmetric distribution of vortices was observed experimentally in shear layers, the initial vorticity profile used in this simulation was more representative of that of a wake. The difference between the stability and long-time behavior of wakes and shear layers could be seen by comparing the results of Ashurst & Meiburg and of Grinstein et al. (1989), who used a finite-difference scheme to simulate the evolution of a spatially-developing shear layer at moderate Reynolds number. Results of the latter indicate that the asymmetric distribution of streamwise vortices develops as a result of the merging of pairs of streamwise rods of the same sign of circulation, and that this interaction only occurs after pairing between neighboring spanwise eddies.

The "sequential" nature of the growth of several forms of 2D and 3D instabilities was investigated in the spectral calculations of Metcalfe et al. (1987). They considered temporal vorticity layers at low Reynolds number, and performed a detailed study of the energy content of the distinct modes. Their results show that, for small perturbations, 2D Kelvin-Helmholtz waves grow first. During their growth, 3D activity is suppressed and the layer maintains a 2D character. Following the non-linear growth of the Kelvin-Helmholtz waves and the formation of ("primary") spanwise eddies, 3D perturbations are amplified. Saturation of the Kelvin-Helmholtz and 3D instabilities is reached soon after the flattening of the (primary) spanwise cores and the "maturation" of 3D modes. They also show that pairing of spanwise cores, during which 3D activity is suppressed, is necessary for further growth of the layer. Following pairing, the growth of 3D modes is resumed. Amplification of 3D disturbances is thus restricted to windows separating periods of otherwise 2D growth.

The dependence of the response of the shear layer on initial conditions and forcing levels was investigated by Inoue (1989), who performed a vortex filament simulation of a spatially-developing layer modeled by a single vortex sheet. His results show that the 3D transition strongly depends on 3D forcing, and that the flowfield tends towards 2D behavior once this forcing is interrupted. This was contradicted by the numerical experiments of Grinstein et al. (1989) which indicate that the transition to 3D motion persists despite the absence of a continuous forcing function. This result was verified in the simulations of Lowery et al. (1987), who employed a hybrid finite difference - spectral method to track the evolution of a passive scalar in a developing layer at low Reynolds number. While the study focused on asymmetric entrainment patterns in 2D and 3D (Dimotakis 1989, 1986), it also emphasized the fact that distributions of spanwise and streamwise vorticity are weakly dependent on the strength and shape of the forcing function. As indicated below, vortex simulations, similar to those of Inoue (1989) and Ashurst & Meiburg



(1988), which do not allow the number of computational elements to increase as the material elements are stretched, may lose accuracy and contaminate the computations with numerical diffusion errors.

Despite these efforts, a clear and unified interpretation of the role of the various modes in the formation of vortical and scalar structures, a crucial step towards a better understanding of 3D transition, has not been reached. Moreover, several important issues, summarized next, cast some doubt on the conclusions of these simulations. Using desingularized vortex sheets to model shear layers, as in Ashurst & Meiburg (1989), may lead to spurious results since, as shown by the detailed numerical study of Knio & Ghoniem (1991), the properties of the 3D modes of a vortex structure are strongly dependent on the vorticity distribution within the cross section of the structure. The use of vortex filaments to resolve vorticity within the shear layer is not recommended since the corresponding schemes, although accurate for short times, do not maintain their accuracy as vortex elements tend to move apart due to stretching in the direction normal to that of the main flow. This violates an important accuracy condition in vortex methods, namely that the cores of neighboring vortex elements must, at all times, overlap.

Another source of inaccuracy in the simulations presented in Ashurst & Meiburg (1988) is the enforcement of the periodic boundary conditions. A small number of images was used on either side of the computational domain, which was not enough to capture the correct value of the free stream velocity. On the other hand, the conclusions of the spectral simulations of Metcalfe et al (1987), particularly those concerning the onset of and the interaction between the 2D and 3D modes described above, may be dependent on some diffusive-convective balance achieved only at low Reynolds number. This balance, which is a function of the Reynolds number, can lead to an early saturation of the instability. We believe that a high Reynolds number simulation is necessary to determine whether the interaction between the different modes of the 3D instability is, as widely suspected, an essentially inviscid mechanism.

The large number of mechanisms governing the evolution of shear layers, and the complexity of the resulting vortical and scalar structures underscore the need for accurate numerical methods which can carefully treat the vorticity transport equation. Successful implementation of numerical schemes depends on the proper account of the vorticity stretching term, and, if present, vorticity source terms. Another crucial ingredient lies in the ability of the method to accommodate the large strain associated with high concentrations of vorticity. The latter have been shown to result in the deterioration of the discretization accuracy in both Eulerian computations, through the creation of small scale structures which may not be well represented on a grid of fixed mesh size and the accumulation of numerical diffusion which may dissipate these structures at their early stages, and Lagrangian computations where zones of high strain may be depleted of computational elements. Finally, questions regarding the dynamic effect of density gradients, in

the absence of gravity, which impact mixing of gases at different molecular weight and/or density, have not been tackled before.

In this work, an adaptive, Lagrangian numerical scheme is used in the simulation of vorticity layers. Two main ingredients are incorporated in the construction of the scheme, which was analyzed in our previous effort (Knio & Ghoniem, 1991). The first relates to its adaptive nature, a feature which avoids the loss of spatial resolution and allows the accommodation of high strain rates by increasing the number of computational elements as the flow evolves. The second, a property found in most Lagrangian methods, consists of ensuring a minimal effect of numerical diffusion which may lead to excessive smearing of the vorticity. We also apply a vortex scheme extended to variable-density flows to analyze the dynamic effect of finite density gradients on the evolution of the shear layer.

Computed results are used to accurately portray the severe deformation of the flow map and the evolution of the flow vorticity. We focus on the relationship between the deformation of material surfaces, the generation and intensification of vorticity and the associated scalar entrainment patterns. The results are used to characterize the 3D instabilities of the vorticity layer. Instability modes leading to the generation of streamwise vortex rods joining neighboring eddies are identified and distinguished from those affecting the vortex cores. A generalized perspective of the latter is given; the similarity between vorticity patterns found in the late stages of spanwise vortex cores in the shear layer and those observed in the development of vortex rings is discussed. Finally, we investigate some of the mechanisms leading to the onset of asymmetry in an otherwise symmetric flow. In particular, a variable-density layer is contrasted with a uniform-density asymmetric layer, in order to study the roles of density variation and asymmetric strain field on the development of the vorticity field.

The numerical scheme used in the computations is summarized in Section 2. In Section 3, we review the evolution of a uniform-density symmetric layer, then present results of variable-density and asymmetric vorticity layer computations. The results are further discussed in Section 4; concluding remarks are given in Section 5.

## 2. FORMULATION AND NUMERICAL SCHEME

### 2.1. FORMULATION AND GOVERNING EQUATIONS

We start with the incompressible, isentropic, variable-density form of the governing equations in the low Mach number limit (Rehm & Baum, 1978; Majda & Sethian 1987, Ghoniem & Krishnan, 1989). By choosing an appropriate combination of characteristic length, time and velocity scales as normalizing parameters, these equations are written as:

$$\frac{D\rho}{Dt} = 0 \quad (1)$$

$$\rho \frac{Du}{Dt} = -\nabla p \quad (2)$$

where  $x = (x, y, z)$  is the position vector,  $u = (u, v, w)$  is the velocity,  $t$  is time,  $\nabla = (\partial/\partial x, \partial/\partial y, \partial/\partial z)$  is the gradient operator, and  $D/Dt = \partial/\partial t + u \cdot \nabla u$  is the material derivative. Since the pressure and density variations are decoupled, we can supplement Eqs. (1) and (2) with:

$$\nabla \cdot u = 0 \quad (3)$$

By taking the curl of Eq. (2) and using the solenoidality condition, Eq. (3), we get the vorticity transport equation:

$$\frac{D\omega}{Dt} = \omega \cdot \nabla u + \frac{\nabla \rho}{\rho^2} \times \nabla p \quad (4)$$

where  $\omega = \nabla \times u$  is vorticity. A more suitable form of the vorticity transport equation is derived by substituting Eq. (2) for  $\nabla p$  into Eq. (4) thus yielding:

$$\frac{D\omega}{Dt} = \omega \cdot \nabla u - \frac{\nabla \rho}{\rho} \times \frac{Du}{Dt} \quad (5)$$

The vorticity associated with a material particle changes due to tilting and stretching under the action of the strain,  $\nabla u$ , and due to the particle acceleration in a non-uniform density field. Equation (5) is preferred over Eq. (4) because the baroclinic source term is written in terms of the kinematics of the flowfield rather than being treated as a dynamic effect associated with pressure forces. Buoyancy effects have been neglected in the vorticity transport equation since we intend to focus on high-speed flows in which fluid acceleration is much larger than gravitational acceleration. Under these conditions, gravity effects are negligible whenever the Richardson number,

$$Ri = \frac{g \Delta \rho \Delta l}{\rho_0 U^2} \quad (6)$$

written in terms of the gravity constant,  $g$ , and characteristic density,  $\rho_0$ , length,  $\Delta l$ , density difference,  $\Delta\rho$ , and velocity difference,  $U$ , is small (Koop & Browand, 1979).

The presence of the baroclinic source term requires the accurate estimation of the density gradient. To this end, we derive a transport equation for the scalar gradient (the density in this case), by taking the gradient of Eq. (1) to obtain:

$$\frac{Dg}{Dt} = -g \cdot \nabla u - g \times \omega \quad (7)$$

where  $g = \nabla\rho$ . Thus, while density remains constant along a material path, its gradient is affected by the local strain and the vorticity. Working with Eq. (7) instead of Eq. (1) is of similar nature as using the vorticity transport equation in place of the momentum equation. Both substitutions are motivated by the observation that, in most high Reynolds number flows, the supports of the vorticity and scalar gradient are small subsets of the supports of the primitive variables. Thus, computational effort is concentrated into smaller regions of the domain of study, and the numerical differentiation of the density field is avoided, thereby minimizing a loss of resolution.

## 2.2. NUMERICAL SCHEME

The transport element method is used to compute the evolution of the shear layer. The numerical scheme solves the time-dependent, inviscid, incompressible, vorticity, scalar and scalar gradient transport equations given above. Variants of the numerical scheme which accommodate gravity, compressibility, chemical reactions and diffusion have been extensively used in 2D (Ghoniem & Krishnan, 1988), and in a limited number of applications in three-dimensions (Knio & Ghoniem, 1992), but will not be required in this study.

The numerical method is the product of the combination of a series of refinements of 3D vortex methods with the scalar transport techniques developed in the 2D transport element method (Ghoniem et al., 1988). It is based on the discretization of the vorticity and scalar gradient fields into a finite number of Lagrangian elements, called transport elements. Transport elements carry discrete scalar, vorticity and scalar gradient values, and are distributed along elementary rectangular areas which are used to divide entire material surfaces. The Lagrangian mesh defines the location of the elements, while vector quantities are not restricted to lie within elementary rectangular areas. Discrete quantities are smoothed in a small spherical neighborhood of the center of the element. A third order Gaussian core function,  $\psi_\delta = 3/(4\pi\delta^3) \exp(-r^3/\delta^3)$ , is used as smoothing function, and its standard deviation  $\delta$  is used as characteristic core radius (Knio & Ghoniem, 1991). This yields a continuous version of the vorticity field which induces a desingularized velocity field, expressed in terms of the Biot-Savart law (Batchelor, 1967). The material surfaces are tracked by moving the

vertices of the elements with the local velocity vector, using a second-order, predictor-corrector time integration scheme.

The construction of the transport element method closely mimics conventional vortex element schemes. Numerical analysis of these schemes reveals that the smoothing functions control the order of the spatial resolution and that strong overlap among the cores of neighboring elements is required to guarantee convergence (Beale & Majda, 1982a,b; Beale, 1986). While the third-order Gaussian functions have been shown to yield second-order schemes (Leonard, 1985; Beale & Majda, 1985), it is the overlap condition that first motivated the modification of the 3D vortex method, in which vortex elements are distributed along vortex tubes. In vortex methods and vortex filament methods, vortex elements are redistributed along vortex tubes whenever the strain causes the separation distance between neighboring elements to exceed the core radius. However, the overlap condition cannot be enforced if the elements (or filaments) are strained in a direction normal to the local vorticity vector. As a result, deterioration in the spatial resolution may occur at long times as large discretization errors pollute the solution. In the present computations, a scheme of local mesh refinement which subdivides computational elements along two directions of strain is employed. This scheme, which is described below, has been shown to yield significant improvement in the accuracy of the computations over vortex element computations (Knio & Ghoniem, 1991).

Another advantage of the transport element method lies in the fact that tracking material surfaces greatly simplifies the task of integrating the equation of motion of the density gradient. This is achieved by associating with each transport element an elementary surface area  $\delta A_i(t)$  and a unit normal to the surface area at the center of the element  $n_i(t) = \delta A_i(t) / |\delta A_i(t)|$ . In the computations, this is done by requiring that material surfaces effectively constitute iso-scalar surfaces, and adopting linear interpolation functions to describe the shape of the material surface within each transport element. We take advantage of kinematical relationships which relate the evolution of the gradient of a non-diffusive scalar in an incompressible fluid at a material point  $\chi(t)$ ,  $g(t, \chi)$ , to that of an elementary surface area centered around  $\chi$ ,  $\delta A(t, \chi)$ , initially having same sense and direction as  $g$ . This relationship, which constitutes the analogue of the Helmholtz vorticity theorem, may be expressed as:  $g(t, \chi) = \alpha \delta A(t, \chi)$ , where  $\alpha = |g(0, \chi)| / |\delta A(0, \chi)|$ . In view of the preceding, we avoid integrating Eq. (7) simply by following the evolution the elementary surface areas.

The description of the method is completed by specifying a technique for updating the discrete values of vorticity associated with the transport elements. Two techniques are used in the computations. In the absence of density variation, direct integration of the vorticity transport equation is avoided. In this case, substantial computational savings are achieved by taking advantage of the Helmholtz and Kelvin theorems since vorticity lines, identified by their

circulation, evolve as material lines. In this variant of the scheme, vorticity changes according to the stretching and tilting of elementary material segments lying in its direction, while the circulation associated with a transport element remains constant. This procedure avoids the evaluation of the velocity gradient, and retains the conservation of the volume of vorticity property possessed by vortex filament methods (Greengard, 1986).

When dealing with a variable density flows, we can no longer apply the Helmholtz vorticity theorem. Therefore, we are not able to avoid the integration of Eq. (5), and, in doing so, the evaluation of the velocity gradient. The procedure suggested here is to split that task in two fractional steps, by first numerically integrating:

$$\frac{D\omega}{Dt} = \omega \cdot \nabla u \quad (8)$$

and, in a second step, integrating:

$$\frac{D\omega}{Dt} = - \frac{\nabla \rho}{\rho} \times \frac{Du}{Dt} \quad (9)$$

This procedure is similar to the "viscous splitting" of the viscous vorticity transport equation (Chorin, 1973), and thus may be termed "baroclinic splitting" of the equation of motion. In the numerical integration of Eq. (8),  $\nabla u$  is found by analytically differentiating the desingularized Biot-Savart law, while the same predictor-corrector employed to advance the computational mesh is used to perform the time integration. Equation (9) is integrated in a single step, by estimating the baroclinic torque from the knowledge of (i)  $\rho$  which is constant for each element, (ii)  $\nabla \rho$  which is computed according to the deformation of the elements, and (iii)  $Du/Dt$  which is approximated by a first-order, backward finite difference in time,  $Du/Dt \equiv (u(t) - u(t - \Delta t)) / \Delta t$ .

In the non-linear evolution of the flowfield, a strong and rapid deformation of the Lagrangian computational mesh is experienced. This deformation causes the depletion of computational elements in some regions of the domain where the separation distance between neighboring elements becomes excessively large. In this work, we employ a local mesh refinement scheme which splits a transport element into two whenever the average value of opposing sides of the rectangles exceeds the value of the core radius. The scheme has been described in detail in (Knio & Ghoniem, 1991). It essentially ensures that core overlap among neighboring elements is satisfied and amounts to redistributing the vorticity and scalar fields into a larger number of elements due to strong strain.

### 2.3. INITIAL AND BOUNDARY CONDITIONS

A variable-density temporal vorticity layer of finite thickness is assumed at  $t = 0$ . A right-handed rectangular coordinate system  $(x, y, z)$  is chosen so that the initial vorticity distribution is aligned with the positive  $y$ -axis, the flow being uniform in the streamwise  $x$ -direction. A second-order Gaussian vorticity distribution with standard deviation  $\sigma$  is adopted to describe the variation of vorticity within the layer. The thickness of the vorticity layer,  $\sigma$ , and the free stream velocity are chosen as length and velocity scales. The initial vorticity and velocity field are given, respectively, by:  $\omega_y(x, 0) = 2/(\sigma \sqrt{\pi}) \exp(-z^2/\sigma^2)$ ,  $\omega_x(x, 0) = \omega_z(x, 0) = 0$ ,  $u(x, 0) = \text{erf}(z/\sigma)$ ,  $v(x, 0) = w(x, 0) = 0$ . For  $\sigma = 1$ , the velocity initial flowfield satisfies:  $u(z \rightarrow \pm\infty) = \pm 1$ . Furthermore, the layer is assumed periodic in the streamwise  $x$ - and spanwise  $y$ -directions, with periodicity lengths  $\lambda_x$  and  $\lambda_y$  respectively, and is unbounded in the cross-stream  $z$ -direction. The initial density distribution is an error-function profile, and the reference density scale is chosen so that the low-density fluid has  $\rho = 1$ .

The periodicity boundary conditions introduce some difficulties in the evaluation of the flowfield and of its gradient since we must consider the image system of the transport elements. This system yields an additional term which must be added to the velocity induced by the elements in the domain. Unlike the 2D case, this term may not be deduced from a potential flow, and closed form expressions to include its effect are not known (Ashurst & Meiburg, 1988). In the computations, we have adopted the procedure described in (Knio & Ghoniem, 1991), which consists of computing directly the effect of the eight immediate neighbors of the elements, and approximating the induced velocity of the images which lie within a square of side  $400 \lambda_x$  by interpolation on a fixed grid. While previous studies have only included the contribution of a small number of images (Ashurst & Meiburg, 1988), the procedure suggested in Knio & Ghoniem (1991) is preferred because it yields more accurate representations of the velocity and velocity gradient fields, and avoids the generation of numerical boundary layers at the spanwise boundaries of the domain (Inoue, 1989).

### 3. RESULTS

In this section, we focus on the deformation of the primary (essentially two-dimensional) structure due to the 3D instabilities, and on the formation of secondary structures as these instabilities evolve into their non-linear stages. We attempt to unify the various postulates on the origin and mechanisms of the 3D motion. By comparing our results to available experimental evidence (Breidenthal, 1980, 1981; Jimenez, 1983; Jimenez et al., 1985, Bernal, 1981, Lasheras & Choi, 1988; Lasheras et al., 1986) and to numerical solutions (Ashurst & Meiburg, 1988, Metcalfe et al., 1987, Lowery et al., 1987; Grinstein et al., 1989), we proceed to clarify some of the aforementioned issues, and point to strengths and deficiencies of previously proposed models. Another objective is to provide a base solution which, in turn, is used to highlight the baroclinic effects in the variable-density layer.

#### 3.1. SYMMETRIC, UNIFORM-DENSITY SHEAR LAYER

A temporal shear layer with streamwise periodicity length  $\lambda_x = 13.2$ , which matches the wavelength of the most unstable 2D mode (Ghoniem & Krishnan, 1989) and spanwise periodicity length  $\lambda_y = \lambda_x/2$ , which lies close to the most amplified 3D mode of the transverse instability (Pierrehumbert & Widnall, 1982), was computed. The initial scalar distribution has a zero mean and a unit difference across the layer. The shear layer is initially discretized among elements distributed on a grid of  $20 \times 14 \times 5$  points along the  $x$ -,  $y$ -, and  $z$ -directions respectively. Thus, computational elements are distributed on five material or iso-scalar surfaces. The selection of the number of material surfaces is chosen as the minimum number required for accurate representation of the eigenfunctions of the Kelvin-Helmholtz instability (Ghoniem et al., 1988). The core radius of the smoothing functions is chosen so that strong overlap among the cores of neighboring elements is ensured, and the vorticity of the elements is obtained by minimizing the integral error between assumed and discretized vorticity profiles (Knio & Ghoniem, 1991). In the computations, we set  $\delta = 0.89$  and the time step  $\Delta t = 0.1$ . The layer is initially perturbed in both the streamwise and spanwise directions by displacing the computational elements in the cross-stream direction using sinewaves of amplitude  $\varepsilon = 0.02\lambda_x$ , i.e. by using the transformation  $z_i \rightarrow z_i + \varepsilon \sin(2\pi x_i/\lambda_x) + \varepsilon \sin(2\pi y_i/\lambda_y)$  (see figure 1.)

##### 3.1.1. DEFORMATION OF MATERIAL SURFACES

Figures 2 and 3 depict perspective views of the iso-scalar surfaces initially located at  $z = 0$ , and  $-1.32$  respectively. The surface initially lying at  $z = 0$  represents the middle surface where most of the vorticity is concentrated, while increasing or decreasing the value of  $z$  corresponds to



motion towards the top or bottom streams. The plots are generated from the point of view of an observer located at (48,24,48).

Due to rollup of the layer, computational elements accumulate in the core which forms during  $4.0 < t < 8.0$ . Previous analysis of the 2D solution indicates that, for the present amplitude of the streamwise perturbation, the linear stages of the evolution of the primary 2D instability end between  $t = 4.0$  and  $8.0$ , followed by roll-up. The amplitude of the spanwise perturbation remains small for  $t < 8.0$ , i.e. its amplification is essentially suppressed during the growth of the 2D mode.

The growth of the eddy core in the mid-section of the domain continues while its spanwise waviness amplifies. The amplitude of the spanwise perturbation increases significantly along the core, an indication of the evolution of the translative instability (Pierrehumbert & Widnall, 1982). This uneven axial displacement of the spanwise core is accompanied by an out-of phase deformation of the braids under the influence of the streamwise vorticity generated within the cores. The growth of the translative instability is shown by plotting the row of elements initially aligned along the core centerline in figure 3b. Vortex lines aligned with the axis of the spanwise core suffer a mild net deformation in the streamwise direction. The evolution of the spanwise core instability occurs such that vortex lines constantly re-align with the direction of strain while being stretched along their axial direction.

The fluid motion along the braids is illustrated in figure 3c. The stretching of the braids leads to the intensification of streamwise vorticity produced as the braids are deformed by the growth of the "translative" instability along the core, and strained by the 2D flowfield. Vortex rods, which extend throughout the braids and are wrapped around the spanwise cores, form as streamwise vorticity rolls into coherent eddies. The material surfaces spin around the streamwise axes of these eddies, which are located at the streamwise boundaries and middle of the domain. This motion is accompanied by the thinning of the strip in the region separating neighboring streamwise vortices, thus producing a "hairpin" vortex configuration. The resulting deformation of the flow map is captured by the mesh refinement algorithm which can also be observed in the surface plots. Since the flow is inviscid, the division and change of shape of the transport elements describes the strain field, especially when the elements approach the spanwise core or when they are attracted towards the axes of the vortex rods.

The adaptive response of the numerical scheme is illustrated in Table 1 where the surface area,  $A$ , and of the number of elements,  $N$ , used along individual material surfaces are given. While both grow rapidly following the roll-up of the vorticity layer, the increase in the number of transport elements occurs at a higher rate than that of the surface. Though the middle surface deforms at higher rate and carries a larger number of transport elements than the remaining surfaces, small zones of high strain exist along all material surfaces. These zones necessitate the introduction of new elements, an effect which precedes the severe deformation of the surfaces.

Table 1  
Normalized surface area,  $A$ , and number of elements,  $N$ , for the individual material layers.

	$t = 4.0$	$t = 8.0$	$t = 12.0$	$t = 16.0$
Material Layer: 1 Location: $z = -1.32$	$A = 1.03$ $N = 1.00$	$A = 1.12$ $N = 1.20$	$A = 1.62$ $N = 1.68$	$A = 3.26$ $N = 3.80$
Material Layer: 2 Location: $z = -0.66$	$A = 1.04$ $N = 1.00$	$A = 1.22$ $N = 1.33$	$A = 2.31$ $N = 2.54$	$A = 4.79$ $N = 7.05$
Material Layer: 3 Location: $z = 0.0$	$A = 1.04$ $N = 1.00$	$A = 1.43$ $N = 1.49$	$A = 2.71$ $N = 3.24$	$A = 5.41$ $N = 9.53$
Material Layer: 4 Location: $z = 0.66$	$A = 1.04$ $N = 1.00$	$A = 1.22$ $N = 1.33$	$A = 2.31$ $N = 2.54$	$A = 4.79$ $N = 7.05$
Material Layer: 5 Location: $z = 1.32$	$A = 1.03$ $N = 1.00$	$A = 1.12$ $N = 1.20$	$A = 1.62$ $N = 1.68$	$A = 3.26$ $N = 3.80$

Figure 4 shows cross-sections through all the material (computational) surfaces at the time the computations are stopped,  $t = 18.0$ . (As indicated below, the structure of the flow field does not vary appreciably for  $t \geq 16$  due to saturation of the instabilities. This additional frame is provided to emphasize this feature of the computed flow; the subsequent discussion will be limited to results obtained for  $t \leq 16$ ). We take streamwise cross-sections through the braid and core in the planes located at  $x = 2.0$  (d) and  $x = 6.6$  (c), respectively, and spanwise sections along the planes  $y = 1.6$  (b) and  $y = 3.3$  (a). Small circles, whose radii are chosen smaller than the core radius, are drawn to mark the intersection points with the transport elements. The streamwise sections, (c) and (d), show how the streamwise rods, resulting from the roll-up of the braids, give rise to the formation of the mushroom structures (Bernal & Roshko, 1986; Lasheras, Cho & Maxworthy, 1986; Lasheras & Choi, 1988). They also depict how the extension of these rods around the spanwise cores results in the establishment of a double mushroom structure (Lasheras & Choi, 1988). The results show that the deformation of the material surfaces within the core is due to the combined effect of three rows of streamwise vortex structures: two rows resulting from the extension of vortex rods towards the core, and a third generated by the deformation of the core itself under the action of the translativ instability. This is shown schematically in figure 5.

The spanwise sections illustrate the effect of the translativ instability on the cross-stream position of the core and the shape of its cross-section. Figure 4 shows that the core is pushed upwards and in the flow direction of the top stream in the "left" half of the domain,  $0 < y < \lambda_y/2$ , while it suffers an antisymmetric deformation in the other half, as can be seen in figures 2 and 3. The core loses its symmetry at most spanwise stations, as computational elements migrate in the

direction opposite to that of the core translation. The distribution of material particles in the plane  $y = 3.3$ , which intersects the central streamwise vortex rod, shows that the braids significantly thicken at this critical spanwise location by entraining irrotational fluid from one side of the layer to the other. This is be verified by simultaneously examining the streamwise cut through the plane  $x = 6.6$ , which illustrates the entrainment of the mushrooms around the spanwise core.

### 3.1.2. VORTICITY AND SCALAR DISTRIBUTIONS

The motion of the material surfaces follows the evolution of the vorticity field. This motion establishes entrainment patterns within the shear layer. Both are displayed in figures. 6-9 in the form of vorticity and scalar contours plotted, respectively, on two spanwise sections,  $y = 3.3$ , and  $5.0$ , and on two streamwise sections,  $x = 2.0$  and  $6.6$ . The vorticity and scalar contours, generated using different techniques, are generated at times  $t = 4.0, 8.0, 12.0$ , and  $16.0$ . Vorticity contours are generated by using the core smoothing function  $s$  to compute the vorticity on a mesh of  $40 \times 40$  points and processing the data with the NCAR contouring software. A considerable amount of smoothing is introduced in this procedure, and the resulting plots are mainly used to deduce the large-scale features of the vorticity field. A different approach, in which shaded areas of constant scalar concentration are generated by interpolating the discrete scalar values on a  $135 \times 135$ -cells grid, is adopted in the representation of scalar distribution.

#### A. Early Stages of the 3D Motion

At early stages, and until  $t = 8.0$ , the vorticity and scalar contours plotted at various spanwise sections are similar, indicating that the growth of the 3D perturbations is suppressed during the early stages of the 2D instability and that the spanwise vorticity remains essentially uniform across the layer (Metcalf et al., 1987). Weak streamwise structures which change their form between different streamwise stations develop, but have not yet gained enough strength to alter the flow significantly. Meanwhile, a single row of counter-rotating vortices is found to repeat itself at all streamwise locations of the domain. These structures are generated by tilting of the vortex lines which, at  $t = 0$ , do not possess a streamwise vorticity component. The tilting of the vortex lines into the streamwise direction(s) leads to the creation of zones of alternating streamwise vorticity whose locations and signs follow the shape of sinewave perturbation. For  $t > 4$ , the streamwise vorticity is slowly intensified under the 2D strain field, producing higher values in the braids of the eddy. With the roll-up of the vorticity layer and the formation of a spanwise core, the edges of the core are stretched up and down towards the free streams, giving rise the top and bottom rows of counter-rotating vortices which appear in figure 8a. These two rows are separated by a third, which appears as a small circle whose vorticity is of the opposite sign to the previous

two. As shown before, the latter is generated as a result of the growth of perturbations on the core itself by the translative instability mechanism.

### B. Late Stages of 3D Motion

For  $8.0 < t < 12.0$ , the flowfield suffers a rapid transition to 3D motion leading to an intensification of the streamwise vorticity in the braids. The total circulation of the streamwise vortices,  $\Gamma_{tot} = \int / \omega_x / dA$  in the plane  $x = 2.0$ , increases from  $\Gamma_{tot}(8) = 2.617$  to  $\Gamma_{tot}(12) = 4.492$ . The streamwise vorticity grows under the action of the strong strain exerted by the large spanwise cores in the neighborhood of the stagnation "lines" which anchor the braids (Lasheras & Choi, 1988). Meanwhile, the deformation of the core, which is attributed to the growth of the translative instability, changes the alignment of the vorticity from predominantly spanwise into spanwise and streamwise components. Although the maximum value of streamwise vorticity occurs within the braids, the streamwise eddies generated by the core deformation have higher total circulation. At  $t = 12.0$ , the middle row of streamwise vortices in figure 8a accounts for 65% of the total circulation in the plane of the core. This is because the growth and maturation of the primary 2D instability, which precede the 3D motion, force the migration of the spanwise vorticity from the thinning braids into the core.

The total streamwise circulation in the plane dividing the core,  $x = 6.6$ , used as a measure of the 3D effects in the flow, is shown in figure 10. It confirms the early observation that 3D effects are small during the linear stages of the 2D instability and grow rapidly after roll-up. The behavior of the curve changes from an algebraic growth for  $t < 9$ , to an exponential growth between  $9 < t < 13$ . At later stages, a non-linear regime characterized by a drop in the rate of increase of the total circulation is observed. This is expected since the strain field induced by the spanwise eddy leads to continuous intensification of the streamwise vorticity. For  $t > 16.0$ , no qualitative changes in the structure of the vorticity and scalar fields is observed, an indication that the instabilities tend to saturate (Metcalf et al., 1987).

At late stages, the streamwise vortices induce a strong secondary motion. As previously indicated, this motion can be easily analyzed in the braids of the eddy where scalar mushroom structures are generated. However, the scalar distribution is more complex in the core, where the flow is under the combined influence of spanwise and streamwise vortices. The top and bottom mushrooms, which form due to the roll-up of the braid vorticity and are identified in figure 8b, originate in the braids and are then entrained towards the cores. Near the axis of the core, the scalar distribution is affected by the flowfield induced by the three rows of alternating streamwise vortices shown schematically in figure 5. The superposition of the fields of these vortices, whose axes are deformed under the action of the translative instability, leads to the generation of "W-shaped" scalar structures.

The spanwise vorticity contours at  $t = 12.0$ , although similar to those encountered in a 2D flow, exhibit a more compact core than in 2D due to stretching along the axis of the core. The stretching of spanwise vorticity is accompanied by a non-uniform deformation of the cores at different spanwise locations. The corresponding variation of the spanwise vorticity is depicted in the last frames of figures 6 and 7. The core is shifted downwards and in the direction of the bottom stream for  $\lambda_y/2 < y < \lambda_y$ , while it suffers an antisymmetric displacement for  $0 < y < \lambda_y/2$  (see also figures 2-3). This confirms the results of the linear stability theory of perturbed vortex cores which predicts a "translative" instability of the cores in the manner described above (Pierrehumbert & Widnall, 1982). We also note that the point of maximum vorticity within the core, which moves in the direction opposite to that of the outer boundaries of the core, no longer coincides with its geometric center. This configuration resembles that observed in the evolution of the eigenfunctions of the linear stability problem of vortex rings, which also predicts a similar behavior for any locally curved vortex filament (Widnall and Tsai, 1977). We recall that the most amplified mode of the translative instability mechanism is characterized by an eigenfunction which changes sign within the vorticity core. This property also arises in the linear stability of vortex rings as a necessary condition for eigenfunction instability. In both cases, the amplification of the instability forces the migration of the "inner" core in the direction opposite to the motion of its outer boundaries.

This mechanism appears to be connected to convective currents within the core and not to a uneven vorticity stretching. This is verified by inspecting the scalar distribution in the same cross-sections which shows that the scalar field follows a similar redistribution and loses its symmetry. This motion leads to preferential entrainment of irrotational fluid from the free streams. The section of the core which is displaced upwards,  $0 < y < \lambda_y/2$ , entrains more fluid from the bottom stream, while the section which is pushed downwards consists mainly of the top-stream fluid. This form of preferential entrainment resembles that reported experimentally (Bernal & Roshko, 1986).

The symmetry of the vorticity and scalar distributions is preserved at the spanwise mid-section of the domain, since, as predicted by the theory, the curvature of the core vanishes at that location. Nevertheless, this plane is of interest since it intersects the streamwise vortex rod centered in the domain (see figures. 2-3). This rod appears in the form of a "tongue" of negative vorticity which extends through the braids to the top and bottom edges of neighboring cores (figure 6a,  $t = 16.0$ ). At this plane of zero curvature, the action of the translative instability is manifested by the presence of two vorticity maxima. A similar vorticity distribution is obtained in unstable vortex rings at azimuthal stations where the curvature of the axis of the core vanishes (Knio & Ghoniem (1988). In the shear layer, these stations lie within the planes  $y = 0$ ,  $\lambda_y/2$ , and  $\lambda_y$ , while, in the vortex ring, the local curvature vanishes whenever the curvature induced by the

growth of azimuthal bending waves cancels that of the undisturbed vortex ring. The resemblance between the two cases bears important implications regarding the implementation of numerical schemes and the modeling of the vorticity layer. The numerical study in Knio & Ghoniem (1990) shows that the dynamics within concentrated vortices may not be properly predicted unless a sufficiently large number of computational elements is used to discretize the the vortex cores. As a result, the computations could have missed or spuriously predicted the evolution of the translative instability, had we chosen to simulate the vorticity layer by distributing the transport elements on a single material layer, or to model the layer as a thin vortex sheet, as in Ashurst & Meiburg (1988) and Inoue (1989).

### 3.1.3. ENTRAINMENT ENHANCEMENT

The development of the 3D instabilities promotes shear layer entrainment (Knio & Ghoniem, 1991). To quantify this effect, the shear layer entrainment is measured by introducing an "eddy size" parameter,  $S$ , in 2D and 3D. In 2D, the eddy size is defined by the measure of the region enclosed between the surfaces where the normalized scalar first deviates by 3% from the corresponding free stream value. This yields a local height of the eddy,  $Z_{2D}(x)$ , which, when integrated over the streamwise length of the domain, gives a mean eddy size,

$$S_{2D} = \int_0^{\lambda_x} Z_{2D}(x) dx \quad (10)$$

According to this definition, the eddy consists of the union of the rotational fluid and the irrotational fluid trapped between the braids and the core (see figure 11). In 3D, two similar definitions are considered. The first is obtained by measuring the height of the eddy at each spanwise and streamwise location,  $Z_{3D}(x,y)$ , and then integrating over the spanwise and streamwise periodicity length to get an eddy size,

$$S_{3D} = \int_0^{\lambda_x} \int_0^{\lambda_y} Z_{3D}(x,y) dy dx \quad (11)$$

While this definition is a natural extension of that in 2D, the contribution of the irrotational fluid trapped by the mushroom structures is neglected in the averaging process. To account for this additional entrainment mechanism, we define a third measure,  $S'_{3D}$ , by:

$$S'_{3D} = \lambda_y \int_0^{\lambda_x} Z'_{3D}(x) dx \quad (12)$$

where  $Z'_{3D}(x) = \max_y(Z_{3D}(x,y))$ .

The eddy size is normalized by the spanwise and streamwise periodicity lengths in 3D computations and by the streamwise periodicity length in 2D, so that the resulting values represent an average thickness of the scalar distribution. The entrainment enhancement is shown in figure 12 by comparing the eddy size for 2D and 3D computations. With the roll-up of the layer,  $t \sim 8.0$ , entrainment curves start to grow with the curves in 3D acquiring a higher growth rate. The deviation in the behavior of the 2D and 3D solutions coincides with the 3D transition depicted in figure 10. Thus, the transition to 3D motion is accompanied by an "entrainment transition." By the end of the simulation, the total entrainment  $S'_{3D}$  increases by 75% over its 2D counterpart, while comparison of  $S'_{3D}$  and  $S_{3D}$  indicates that the formation of the mushroom structures contributes significantly to entrainment enhancement.

The eddy size parameters are also used to quantify the preferential entrainment of fluid at various sections of the domain. This form of entrainment reverses itself every half spanwise wavelength so that the composition of the eddy does not favor either free stream. However, in the region  $0 < y < \lambda_y/2$ , preferential entrainment of lower stream fluid is observed. Preferential entrainment may be estimated by subdividing the integrals in Eqs. (10-12) over the regions defined by:  $s > s_{av}$ , and  $s < s_{av}$ , thus yielding:  $(S_{3D})^+$ ,  $(S_{3D})^-$ ,  $(S'_{3D})^+$ , and  $(S'_{3D})^-$ . At  $t = 16.0$ , the entrainment ratios in the area  $0 < y < \lambda_y/2$ ,  $(S_{3D})^-/(S_{3D})^+ = 1.787$ , and  $(S'_{3D})^-/(S'_{3D})^+ = 3.487$ . These ratios are reversed in the area  $\lambda_y/2 < y < \lambda_y$ , so that unit net entrainment ratios are obtained. The difference between the two ratios is a manifestation of the role of streamwise vortices in inducing preferential entrainment patterns (Bernal & Roshko, 1986).

### 3.1.4 DISCUSSION

The results of the computations show that the evolution of the shear layer from a perturbed steady state using monochromatic 3D disturbances consists of three stages: (1) In the first stage, an essentially 2D growth of the perturbations, in the form of linear amplification of the Kelvin-Helmholtz instability modes, is observed. During this phase, all 3D activity is suppressed. This is followed by a non-linear 2D growth of the fundamental mode, leading to roll-up and the formation of a concentrated spanwise eddy core. (2) The roll-up is accompanied by a rapid growth of the 3D modes, in the form of a deformation of the spanwise eddy and an instability in the braids. (3) The 3D modes undergo a non-linear growth which results in the redistribution of the streamwise vorticity into vortex rods and in the generation of the scalar mushroom structures.

While the 2D instability is relatively simple to describe, the 3D motion in the cores and braids of the vortex structures are more involved. The stability of the rolled layer was examined by Pierrehumbert and Widnall (1982) using a periodic array of Stuart vortices. They found that this array was linearly unstable to a mode they called the translative instability, which leads to a deformation of the spanwise eddies according to the strain field induced by the eddy and by its image vortices. The instability appearing in the braids was studied in the work of Corcos & Lin (1984), who proved the fundamental nature of the instability of a strained streamwise vorticity and showed that the growth of this mode is suppressed during the amplification of the 2D instability. The translative instability is fundamentally different from the Corcos mechanism since the braids of the spanwise vortices, observed in the case of a shear layer, are not well represented by the Stuart vortices. Thus, the two instabilities differ in form. The translative mode is an instability of the spanwise cores, that is of large concentrated vortices subject to strain normal to their axes, while the Corcos mechanism predicts the instability of streamwise vorticity when subjected to strong extensional strain.

The absence of braids does not preclude the formation of vortex rods by the strain field which may cause the vorticity within the core to migrate outwards preferentially (Grinstein et al., 1989). On the other hand, the ability of the streamwise vortex rods generated by the Corcos mechanism to impart a core deformation similar in shape to that obtained by the development of the translative instability (Corcos and Lin, 1984) complicates the task of separating the role of these two instabilities. This difficulty has led researchers (Ashurst & Meiburg, 1988; Lasheras & Choi, 1988) to emphasize the importance of a non-linear interaction between the spanwise cores and the streamwise vortices. Our results, however, indicate that the translative instability within the cores grows simultaneously with the intensification of the rods. Since, as previously mentioned, a mild straining of the streamwise vorticity is observed prior to the roll-up of the spanwise vorticity, and since the translative instability is a linear instability mechanism, the importance of such an interaction should be downplayed.

The formation of the streamwise vortex rods leaves its mark on the flow in the form of scalar mushroom structures. The translative instability, on the other hand, is manifested by an asymmetric spanwise vorticity distribution within the core, which resembles that predicted by the growth of unstable eigenfunctions of the Widnall instability of vortex rings (Widnall & Tsai, 1977). The alternating preferential entrainment patterns which result from the amplification of the instability mode compound the difficulty in experimentally visualizing the scalar structures mentioned by Corcos & Lin (1984), since uniform-density spatially-developing shear layers entrain more fluid from the faster stream (Dimotakis, 1986). Despite these difficulties, a deformation consistent with the development of the translative instability was inferred by Jimenez (1983) and by Bernal & Roshko (1986) based on spanwise correlations of velocity fluctuations.



The analysis of the evolving vorticity structures using numerical simulation makes a valuable contribution since direct and detailed measurements of the vorticity field are usually not possible or extremely cumbersome. Such difficulties are primarily encountered in experimental studies in which velocity correlations (Browand & Troutt, 1980; Jimenez, 1983; Wygnansky et al., 1979), passive scalar or dye techniques (Bernal & Roshko, 1986; Jimenez et al., 1985), or low heat release chemical reactions (Breidenthal 1981; Lasheras et al., 1986; Lasheras & Choi, 1988) have been used as substitute tools for deducing the topology of the vorticity field. Our results suggest that such efforts should be conducted with great care, because a large number of mechanisms contributes to their formation. The computed results reveal some of the difficulties arising from the lack of an accurate knowledge of the vorticity field. In particular, it is shown that the deformation of material surfaces, visualized for instance by injecting marker particles in one of the fluid streams, may not be sufficient to fully determine the corresponding vortical structures, especially if one cannot a priori locate a given material surface with respect to the layer of highest spanwise vorticity. The rapid variation of the strain field around the latter causes substantially different deformations of adjacent layers, thus preventing immediate correlations with the underlying vortical structures. On the other hand, the visualization of vorticity structures by means of the products of a unity-stoichiometry, low-heat-release chemical reaction may remove some of these difficulties, since, as observed by Knio and Ghoniem (1992), the products of reaction are always entrained into zones of high vorticity.

### 3.2 VARIABLE-DENSITY SHEAR LAYER

Density variation, characterized by a density ratio of the free streams, plays an important role in the evolution of heterogeneous shear layers created by the merging two streams of unequal density and velocity. It has been observed that a non-unity density ratio alters the spatial growth of the layer and influences the entrainment induced by the vortical structures embedded therein, even when gravity effects are weak (Brown & Roshko, 1974; Ho & Huerre, 1984; Dimotakis, 1989). In chemically-reacting flows, density variation is generated by heat release which leads to the generation of zones of high temperature and low density. Here too, the presence of two or more zones of different density is found to affect the stability and development of the flow. This effect depends on both the details of the density and vorticity distributions, as it may constitute a stabilizing or a destabilizing mechanism (Riley & McMurtry, 1989; McMurtry et al. [47]; Ghoniem & Krishnan, 1988).

In this section, the effect of weak density variation on 3D instability is investigated by computing the onset of 3D motion in an incompressible, variable-density shear layer. While this study is ultimately motivated by the desire to predict high-heat-release reactions in vortical flows, the simplified model allows us to focus on the dynamic effects of baroclinic vorticity. In a 3D flow, this stepwise approach is important because of the presence of a vorticity stretching term. One case with small density ratio,  $\rho_{max}/\rho_{min} = 2$ , is considered. To avoid a re-initialization of the scalar (density) gradient field, we use the same discrete scalar gradient values of the previous case but set  $\rho_{av} = 1.5$ . Therefore, in the high-density top free stream,  $\rho_{max} = 2$ , and in the low-density bottom free stream,  $\rho_{min} = 1$ . The same initial perturbation used in the previous case is applied, and the computations are performed to observe the growth of both the 2D and 3D instabilities.

The linear theory of variable-density shear layers (Ghoniem & Krishnan, 1989; Krishnan, 1989) shows that the wavelength of the most amplified mode of the 2D instability depends weakly on, and the growth rate are almost independent of the density ratio, while its phase velocity is strongly varied strongly with the density ratio. Unlike the uniform-density case, the most amplified mode in the variable-density layer evolves as a traveling wave moving in the direction of the high-density stream with phase speed increasing with the density ratio. This effect has been used to explain the difference in growth rates in variable-density, spatially-evolving layers (Dimotakis, 1989, 1986; Brown & Roshko, 1974, Ghoniem & Krishnan 1989). For the density and vorticity profiles used in the simulation, and a density ratio of 2, the linear stability theory predicts a phase speed  $c = 0.17$ . We note that the stability analysis performed by Ghoniem & Krishnan (1989) differs slightly from the earlier investigation of Maslowe & Kelly (1971), who showed that, in the limit of vanishing Richardson number, density stratification tends to stabilize a temporal shear layer. The differing conclusions are due to the assumed density profiles. The analysis of Maslowe and Kelly, which was primarily concerned with atmospheric and oceanic

flows, assumed an exponentially-varying density distribution. This distribution is contrasted with the error-function profile which is more representative of high-speed shear flows, where small Richardson numbers are more frequently encountered.

The effect of the density variation on the linear stability of 3D perturbations is not known at present. 3D instability of variable-density shear layers is not a simple extension of that of the uniform-density case since one must deal with the added difficulty of formulating a steady initial condition of the stability problem. In the uniform-density case, Stuart vortices were used to approximate the flow of the rolled layer (Pierrehumbert & Widnall, 1982). The existence of similar solutions in the variable density case is complicated by the convective motion of the vortices due to the baroclinic generation of vorticity, as observed in 2D simulations (Ghoniem & Krishnan, 1989). As a result, and because we have approached the study of 3D temporal layers with the intention of investigating deviations from the 2D case, we were content with keeping the same spanwise periodicity length used in the uniform-density case. This prompted us to select a small value of the density ratio, so that comparisons with the preceding results are justified.

### 3.2.1. DEFORMATION OF MATERIAL SURFACES

Figure 13 shows the evolution of a material surface initially lying in the planes  $z = 0$ . At early stages, the motion of the middle layer bears strong resemblance to its counterpart in the uniform-density case (figure 2). This similarity is expected, and in agreement with the results of the linear stability theory which predicts almost identical growth rates of the 2D perturbation. The first manifestation of the convective motion of the instability wave is observed once the roll-up of the layer is completed and a well-defined eddy core is formed ( $t > 8$ ). During this period, the 3D perturbation is amplified causing the core to deform in the way similar to that predicted by the translative instability of uniform-density cores. However, the (deformed) axis of the core no longer coincides with the streamwise mid-section of the domain, but shifts in the positive streamwise  $x$ - direction, i.e. in the direction of the high-density top stream. The braids suffer a deformation whose shape is of the same type observed in the uniform-density case.

The total surface area of the material surfaces and the number of transport elements, shown in Table 2, exhibit the same trends described in the uniform-density case. However, the motions of surfaces lying on the top and bottom sides of the middle layer are no longer similar because of the asymmetry of the flowfield. Prior to the maturation of the 3D instability,  $t < 12.0$ , the material surfaces lying on the low-density side are deformed at higher rate than those located in the heavier fluid side of the layer. At later stages, this trend is reversed. This asymmetric straining of the surfaces is related to the asymmetry of the spanwise vortices whose rotation resembles the eccentric spinning of egg-shaped cores.

While the uneven deformation of the braids is readily verified at later stages, the asymmetric stretching of streamwise vorticity affects the entrainment patterns in the neighborhood of the spanwise cores (Brown & Roshko, 1974; Dimotakis, 1986, 1989; Ghoniem & Krishnan, 1989). However, the motion of the Lagrangian mesh cannot be used to deduce this effect because the vorticity lines in a variable-density flow cannot be directly identified with material lines, and the deformation of material surfaces is not sufficient to completely determine the fate of the vorticity. In fact, detailed examination of the motion of the material surfaces only indicates that, in the braids, streamwise vorticity re-organizes into rods, leading to the formation of the mushroom structures that cover the eddy cores, and that the spanwise cores propagate in an asymmetric flowfield.

Table 2  
Normalized surface area,  $A$ , and number of elements,  $N$ , for the individual material layers.

	$t = 4.0$	$t = 8.0$	$t = 12.0$	$t = 16.0$
Material Layer: 1 Location: $z = -1.32$	$A = 1.03$ $N = 1.00$	$A = 1.12$ $N = 1.30$	$A = 1.70$ $N = 2.00$	$A = 3.47$ $N = 4.75$
Material Layer: 2 Location: $z = -0.66$	$A = 1.04$ $N = 1.00$	$A = 1.22$ $N = 1.40$	$A = 2.35$ $N = 2.84$	$A = 4.74$ $N = 7.75$
Material Layer: 3 Location: $z = 0.0$	$A = 1.04$ $N = 1.00$	$A = 1.43$ $N = 1.55$	$A = 2.71$ $N = 3.65$	$A = 5.48$ $N = 10.11$
Material Layer: 4 Location: $z = 0.66$	$A = 1.04$ $N = 1.00$	$A = 1.21$ $N = 1.41$	$A = 2.22$ $N = 2.93$	$A = 4.78$ $N = 8.63$
Material Layer: 5 Location: $z = 1.32$	$A = 1.03$ $N = 1.00$	$A = 1.12$ $N = 1.28$	$A = 1.57$ $N = 1.71$	$A = 3.11$ $N = 3.80$

Signs of the influence of the baroclinic vorticity and the associated asymmetry of the strain field on the evolution of the 3D perturbation appear in the cross-sections through the material surfaces. These sections, shown at  $t = 16.0$  in figure 14, are generated on a streamwise section translated in the direction of the heavy stream to  $x = 9.3$  in order account for the convective motion of the eddy. The mean streamwise location of the core is first estimated by translating the plane  $x_{1/2} = 6.6$  by  $ct$ ,  $c$  being the phase speed of the 2D Kelvin-Helmholtz wave obtained from the linear theory. This estimate is then refined by considering neighboring planes on both sides of the plane  $x = x_{1/2} + ct$ . It is found that the mean streamwise location of the eddy shifts from  $x = 6.6$  at  $t = 0$ , to  $x = 7.3, 8.0, 8.6$ , and  $9.3$  at  $t = 4.0, 8.0, 12.0$ , and  $16.0$  respectively. Thus, the convective speed of the eddy is closely approximated by  $c$  even in the non-linear stages (Ghoniem & Krishnan, 1989). For the remaining sections, we still use the planes  $y = 3.3$  and  $1.6$  to

visualize the variations along the span of the layer, and the plane  $x = 2.0$  to obtain a representative streamwise section of the braids.

The large-scale features of the instability in the variable-density flow can be approximated by those found in the previous case simply by accounting for the convective motion of the eddy. However, cross-sections through the core reveal that the mushrooms entrained on top and bottom of the core are not similar. The top mushroom, lying on the side of the high-density fluid, is larger, more rounded, and less developed than its counterpart on the bottom side of the eddy. The concentration of computational elements, visualized by darker areas on the plots, is higher in the lower mushroom especially near the axes of the streamwise vortex rods. Thus, streamwise vorticity is higher for the bottom vortex rods, leading us to expect higher rates of spinning around their axes, and a significant departure from the entrainment patterns observed in the previous case.

### 3.2.2 VORTICITY AND DENSITY FIELDS

The spanwise structure of the layer is shown in terms of the spanwise vorticity and density contours, plotted in figures 15 and 16 in the spanwise planes  $y = 3.3$  and  $5.0$ , respectively. The streamwise structure of the layer is examined by considering cross-sections through the core and the braid. The core cross-sections, figure 17, are generated in the  $y$ - $z$  planes coinciding with the mean streamwise location of the eddy. We use the fixed streamwise plane  $x = 2.0$  to cut through the braids, the results being shown in figure 18. Results are shown at  $t = 12.0$  and  $16.0$ , i.e. following the growth of the 3D modes.

A qualitative similarity between the uniform- and variable-density flow in terms of the types and shapes of vortical structures that are formed as a result of the evolution of the various instabilities is noticeable. The variable-density layer can be characterized by the same stages of evolution as the uniform-density layer: (i) an early growth of the Kelvin-Helmholtz instability during which the layer remains essentially 2D; (ii) a non-linear evolution accompanied by the formation of a spanwise core as a coherent eddy, the onset of the 3D undulation along its axis, and the generation of streamwise vorticity; and (iii) a maturation of the translative instability, the redistribution of the streamwise vorticity into vortex rods, and the formation of scalar mushroom structures. The differences between the two cases, which arise due to the baroclinic generation of vorticity, are summarized in the following:

- (1) The evolution of the Kelvin-Helmholtz mode is modified by a finite phase speed of the waves in the direction of the high-density stream. The motion of the waves is uniform in all spanwise stations, and persists into the non-linear stages.
- (2) The vorticity field loses its symmetry as a result of the vorticity generated by the baroclinic torque. The loss of symmetry is not restricted to any particular spanwise plane, and is not due

to the amplification of 3D modes as it is also observed in 2D simulations (Ghoniem & Krishnan, 1989).

- (3) The loss of symmetry affects the streamwise vorticity via its asymmetric strain field. For  $t < 12.0$ , the top layer of streamwise vortices, lying on the side of the high-density stream, is considerably weaker than its counterpart on the bottom side, while the trend is reversed at later stages. At  $t = 12.0$ ,  $\Gamma_{top}/\Gamma_{bot} = 0.536$ , and increases to  $\Gamma_{top}/\Gamma_{bot} = 1.12$  at  $t = 16.0$ . Thus, the strength of the streamwise vortices changes on both sides of the eddy in accordance with the deformation of material surfaces. This implies that, for  $12.0 < t < 16.0$ , the asymmetric straining of streamwise vorticity leads to the establishment of spanwise entrainment patterns which are biased towards the high-density side. This bias is due to the difference in strength of the streamwise rods wrapped on opposite sides of the spanwise core, and opposes the effect of the streamwise (2D) entrainment currents which favor low-density fluid.
- (4) The loss of symmetry is accompanied by a net asymmetric entrainment of the low-density fluid. We distinguish between the preferential entrainment associated with the growth of 3D modes, and the entrainment asymmetry due to the baroclinic generation of vorticity. The asymmetric entrainment of the low-density fluid combines with the preferential entrainment of low-density fluid in  $0 < y < \lambda_y/2$ , produces an asymmetric distribution at the spanwise mid-section of the domain, and counteracts the effect of the 3D instabilities in  $\lambda_y/2 < y < \lambda_y$ . At  $t = 16.0$ , the entrainment ratios,  $(S_{3D})^-/(S_{3D})^+ = 2.541$ , and  $(S'_{3D})^-/(S'_{3D})^+ = 4.458$  in the area  $0 < y < \lambda_y/2$ , while the net entrainment ratios,  $(S_{3D})^-/(S_{3D})^+ = 1.245$ , and  $(S'_{3D})^-/(S'_{3D})^+ = 1.140$ . Thus, the spanwise entrainment patterns induced by the streamwise vortex rods lead to a reduction of the asymmetry in the entrainment ratio.

### 3.2.3 BAROCLINIC VORTICITY

In order to isolate the effects of the density variation from those associated with vortex stretching, the distribution of the baroclinic torque is used. Figure 19 shows the spanwise component of the baroclinic torque,  $\tau_y$ , in the planes  $y = 3.3$  and  $5.0$ , while the streamwise component  $\tau_x$ , is shown in figure 20 for the core and braid sections. At early stages,  $t < 8.0$ , the spanwise component of the baroclinic torque is concentrated in two zones of opposite signs. The initial vorticity of the layer is depleted in the left-hand side of the domain and enhanced in the remaining part. Thus, baroclinic vorticity imparts an asymmetry on the vorticity distribution such that the part of the layer displaced towards the high-density fluid is weakened, while that pushed in the direction of the low-density stream is intensified. As suggested in Ghoniem & Krishnan (1989), this asymmetry may be used to explain the origin of the motion of the Kelvin-Helmholtz mode.

Reduction of spanwise vorticity on the high-density side of the layer, and its enhancement on the low-density side is responsible for the observed difference in the strength of the streamwise vortices between the top and bottom rows of the core. As shown in figure 20, the streamwise component of the baroclinic term is extremely weak during the linear stages of the primary instability. Therefore, the asymmetry in the streamwise vorticity distribution must be due to the uneven tilting and stretching of layers of varying strengths so that density variation effects are primarily felt through changes in the spanwise vorticity.

At later stages, however, baroclinic torques becomes strong enough to directly affect the evolution of the streamwise vorticity. Density variation does not lead to a net intensification or weakening of the streamwise vortices in the braids since the baroclinic term changes sign within each streamwise eddy. Nevertheless, the baroclinic term is distributed in such a way as to weaken the top parts of the streamwise eddies and to strengthen their bottom parts, leading to a downward drift of the vortex rods. On the other hand, in the core, baroclinic torques contribute to the asymmetry between the top and bottom rows of streamwise vortices. While the middle row of vortices is affected in a similar way as that observed in the braids, figure 20 indicates that baroclinic torques tend to strengthen the vorticity of the bottom row at the expense of the top row.

Thus, density variation plays two different roles in the development of 3D form of the layer. At the early stages, it generates an asymmetric strain field by imparting a convective motion on the core. At the later stages, it redistributes the vorticity within the core. The development of the instability modes in the variable-density shear layer highlights the importance of the asymmetry of the flow and strain fields. In the interpretation of the origin of the complicated structures associated with the 3D effects, the influence of strain and density gradient, which are respectively taken into account in the equation of motion through the vorticity stretching and baroclinic production terms, may be hard to distinguish in the results. To facilitate this task, we consider the case of a uniform-density shear layer with an asymmetric vorticity distribution at  $t = 0$ , and postpone further discussion until results of the latter case are analyzed.

### 3.3 UNIFORM-DENSITY, ASYMMETRIC SHEAR LAYER

Shear layers with asymmetric vorticity profiles are frequently encountered. Typically, these layers are formed following the merging, downstream of the splitter plates, of boundary layers of unequal thicknesses and opposite signs of vorticity. The velocity profile associated with the asymmetric vorticity distribution thus produced can be modeled as the superposition of a symmetric velocity profile induced by an idealized symmetric vorticity distribution, and a wake component biased towards the low-velocity stream. As shown by Koochesfahani & Frierer (1989), the wake component becomes important when the density of the slow stream is much larger than that of the fast stream. In such instances, linear stability analysis shows that the early development of the layer is dominated by the wake mode whose amplification rate is higher than that of the shear layer mode. In the remaining cases, the shear layer mode is dominant, and leads to the familiar roll-up of the Kelvin-Helmholtz waves.

While the wake component might be neglected in 2D models, results of Ashurst & Meiburg (1988) have shown that the detail of the vorticity distribution plays an important role in the development of 3D instability modes. Using two vorticity layers of opposite sign, they predicted an asymmetric spacing of the streamwise vortex rods similar to that experimentally observed (Lasheras & Choi, 1988). However, this approach is complicated by the difficulty in specifying the initial strength and separation of the vorticity layers. In fact, the initial separation of the individual vorticity layers is not uniquely determined in that model, and large separation distances may lead to the independent roll-up of each layer, a behavior that is not obtained in shear layers.

In our study, consideration of shear layers with asymmetric vorticity profiles is motivated by the results of the variable-density layer. In particular, the numerical experiment is designed to mimic the early effects of density variation which were shown to promote the spanwise vorticity of the low-density stream at the expense of that on the high-density side through asymmetric strain. This imitation is obtained by perturbing the second-order Gaussian vorticity profile to yield the asymmetric vorticity distribution shown by a broken line in figure 1. A single vorticity layer in which the velocity increases monotonically from one stream to the other is considered. The scalar is assumed passive, and its initial profile is the same as that used in Section 3.1. We keep the same dimensions and boundary conditions, and apply the same perturbation at the start of the computations. Since the deviation from the symmetric Gaussian profile is small, we expect similar growth characteristics of the 2D component of the perturbation, although its wavelength may not correspond to that of the most amplified Kelvin-Helmholtz mode.

#### 3.3.1 DEFORMATION OF MATERIAL SURFACES

Perspective views of the material surface initially lying in the plane  $z = 0$ , shown in figure 21, exhibit qualitative similarity to that of the first case and hence a detailed analysis of the



Lagrangian motion is omitted. Our discussion, will be restricted to the features by which the asymmetric layer may be identified. The deformation of the material layers is asymmetric with respect to the surface initially at  $z = 0$ , as indicated in Table 3. This development resembles that observed in the variable-density case where baroclinic vorticity generation produces a similar asymmetric strain field. Despite this similarity, the the two cases can be distinguished by the fact that, in the asymmetric uniform-density layer, the core does not exhibit any convective motion. The cross-sections of the material surfaces, plotted in figure 22, show that the asymmetry is primarily exhibited in the core where the top and bottom mushrooms are distinguishable. However, unlike the previous case, there is no indication that they have different strengths.

Table 3  
Normalized surface area,  $A$ , and number of elements,  $N$ , for the individual material layers.

	$t = 4.0$	$t = 8.0$	$t = 12.0$	$t = 16.0$
Material Layer: 1 Location: $z = -1.32$	$A = 1.03$ $N = 1.00$	$A = 1.14$ $N = 1.20$	$A = 1.72$ $N = 1.69$	$A = 3.54$ $N = 4.16$
Material Layer: 2 Location: $z = -0.66$	$A = 1.04$ $N = 1.00$	$A = 1.24$ $N = 1.33$	$A = 2.40$ $N = 2.54$	$A = 5.31$ $N = 8.55$
Material Layer: 3 Location: $z = 0.0$	$A = 1.04$ $N = 1.00$	$A = 1.44$ $N = 1.44$	$A = 2.78$ $N = 3.51$	$A = 5.87$ $N = 9.95$
Material Layer: 4 Location: $z = 0.66$	$A = 1.04$ $N = 1.00$	$A = 1.22$ $N = 1.31$	$A = 2.36$ $N = 2.48$	$A = 5.01$ $N = 7.35$
Material Layer: 5 Location: $z = 1.32$	$A = 1.03$ $N = 1.00$	$A = 1.11$ $N = 1.15$	$A = 1.56$ $N = 1.73$	$A = 3.38$ $N = 3.91$

### 3.3.2 VORTICITY AND SCALAR DISTRIBUTION

Figures 23-26 show scalar and vorticity contours plotted in the non-linear stages of evolution of the flow,  $t = 12.0$  and  $16.0$ . The spanwise sections show some but not all the effects associated with density variation exist in this case. While the convective motion could not be captured, the vorticity and scalar distributions exhibit weak asymmetry at all spanwise cuts, and the rotation of the core resembles the eccentric rotation of an oval-shaped body. Asymmetric entrainment patterns, whereby more fluid from the bottom stream reaches the core, are also established. At  $t = 16.0$ , the composition of the eddy slightly favors bottom layer fluid, as the net entrainment ratios admit small deviations from unity,  $(S_{3D})^-/(S_{3D})^+ = 1.026$ , and  $(S'_{3D})^-/(S'_{3D})^+ = 1.037$ . This corroborates our discussion of the motion of the material surfaces, whose deformation is found more severe in the bottom stream. On the other hand, the similarity between

the asymmetric and variable-density layers is restricted to the fact that these layers can be identified by larger spanwise vorticity values.

The spinning of the asymmetric spanwise eddy causes the generation of streamwise vortex rods of different strengths as they approach the core. Unlike the variable-density case, the vortex rods on the bottom side are intensified at a lower rate in the early stages,  $t < 12.0$ , and this effect is reversed at the later stages. At  $t = 12.0$ , the ratio of the circulation of the two streamwise vortices is  $\Gamma_{top}/\Gamma_{bot} = 1.313$ , and decreases to  $\Gamma_{top}/\Gamma_{bot} = 0.982$  at  $t = 16.0$ . This asymmetry occurs mainly as a result of the difference in shape and size of the streamwise rods as the maximum vorticity values in both remain close. A simplified model clarifying the origin of the difference in strengths between the streamwise rods can be constructed by noting that the stretching of the streamwise vorticity occurs along the streamwise boundaries of the domain where the braids are anchored and pulled towards the core of the eddy. In the braids, the strain is weakly dependent on the detail of the distribution within the core. In fact, the strain in the braids may be approximated by concentrating the spanwise vorticity of the core along its center. Thus, the asymmetry of the vorticity distribution of the spanwise core and of its induced flow and strain fields, are not expected to play a major role in the production of streamwise vorticity. The observed asymmetry becomes essentially a consequence of the eccentric spinning of the spanwise cores.

In the variable-density layer, the above description is modified by the baroclinic production of vorticity. The streamwise component of the baroclinic torque,  $\tau_x$ , is small in the braids, so that the production of streamwise vorticity there is dominated by strain and the contribution of the baroclinic torque to the strength of the streamwise vortices only appears as a modulation of the local vorticity values. On the other hand,  $\tau_x$  increases significantly as we approach the core. Focusing on the later stages of the flow, this observation is justified by realizing that fluid acceleration, which controls the production of baroclinic vorticity, becomes dominated by the convective acceleration. In turn, the convective acceleration must be larger in regions of higher curvature. Therefore, in the variable-density layer, as the streamwise vortices approach the core, their strengths is affected by the baroclinic source term which is shown to strengthen (weaken) the streamwise vorticity of the vortex rods lying on the low-density (high-density) side.

Our numerical results have shown that three mechanisms can lead to symmetry loss in 3D temporal shear layers. The first is associated with the growth of the translative instability which leads to a preferential entrainment pattern reversing itself every half spanwise wavelength of the instability. The second is caused by an initially asymmetric vorticity distribution which induces asymmetric entrainment currents favoring the free stream having higher spanwise vorticity values. Finally, baroclinic vorticity generation plays an important role in the formation of asymmetric structures by imparting a convective motion on the cores and redistributing the vorticity within the cores. These mechanisms should be distinguished from similar effects occurring in 2D and 3D

spatially-developing layers, in which individual mechanisms may be hard to isolate since asymmetric entrainment favoring the high-speed stream is observed before the transition to 3D motion, and the location of vortex amalgamation, which lead to the formation of composite structures of even higher complexity, is not easily predicted (Dimotakis, 1986).

The use of asymmetric vorticity distribution, with a strong negative component, has been suggested by Ashurst & Meiburg (1988) as a means of simulating the effect of the velocity ratio. Their computations were able to capture the asymmetric spacing of the streamwise vortices, observed experimentally by Lasheras & Choi (1988). This asymmetric spacing was not observed in our computations which did not include a negative initial vorticity component. Thus, we conclude that the presence of negative vorticity alone cannot be responsible for this effect and the asymmetric spacing of the streamwise vortices is not a property of the "primary" 3D structure. However, the development described by Ashurst & Meiburg (1988) could occur during the merging of the distorted spanwise eddies. In view of the results of Metcalfe et al. (1987), who showed that in the absence of pairing, both 2D and 3D instabilities tend to saturate, the suggestion that the asymmetric spacing is a product of a higher-order instability could be justified. This interpretation is consistent with the experimental findings of Bernal & Roshko (1986), and with the numerical simulations of Grinstein et al. (1989), who observed that an asymmetric reorganization of the streamwise vortices occurs after the merging of the distorted spanwise eddies.

## 5. CONCLUSIONS

The transport element method was applied to study the evolution of temporal, doubly-periodic, uniform- and variable-density shear layers. The numerical schemes are Lagrangian and adaptive. They are based on tracking the vorticity, scalar and scalar gradients, discretized using a finite number of computational elements. Three cases are considered: (i) a uniform-density vorticity layer with symmetric vorticity profile, (ii) a variable-density vorticity layer, and (iii) a uniform-density asymmetric layer. In the uniform-density case, we take advantage of Kelvin's circulation theorem in order to save computational effort, while the vorticity transport equation is used when the baroclinic source term is present. Thus, the vortex stretching is implicitly taken into account in the first case, while direct evaluation of the vorticity stretching and baroclinic source terms is performed in the second.

Starting from equal "small-amplitude" two- and three-dimensional perturbations, the evolution of the vorticity layer first exhibits a 2D regime which is characterized by the growth and roll-up of the Kelvin-Helmholtz mode. Following this stage, 3D perturbations are rapidly amplified. In all cases, and consistent with previous results, two types of 3D instability are observed: an instability in the braids which leads to the formation of streamwise vortex rods and scalar mushroom structures, and a core instability which causes an uneven deformation of the spanwise eddies. The instability in the braids is associated with the severe stretching of the vortex lines whose extension in the streamwise direction exceeds the separation distance between neighboring spanwise eddies. The streamwise vortex rods are continuously wrapped around the deformed spanwise cores leading to the intensification of the streamwise and spanwise components of vorticity and to the generation of complex vortex structures. While the amplitude of instability of the spanwise eddies does not reach such large values, it is still found to play an important role in the evolution of the flowfield.

A detailed visualization of the vorticity and scalar fields and of the motion of material surfaces was performed. The study focuses on the manifestation of 3D instabilities in vorticity layers. The 3D instability in a vorticity layer with initially symmetric vorticity and scalar profiles exhibits asymmetric vorticity and scalar distributions at different spanwise locations. These forms of asymmetry, which reverse themselves every one-half spanwise periodicity length, are linked to the development of the braids and translative instabilities. Similar entrainment currents are observed in a uniform-density asymmetric vorticity layer, where the asymmetry of the flowfield leads to a preferential entrainment of irrotational fluid from the stream initially having higher spanwise vorticity values. In this case, the effect of the asymmetric vorticity distribution combines with that of the 3D instability, whose development is not significantly altered from the previous case, resulting in a net departure from a unity entrainment ratio. The variable-density layer is

identified by a finite convective speed of the eddies in the direction of the high-density fluid stream and by an asymmetric entrainment pattern favoring the low-density stream. Baroclinic torques affect the development of the 3D modes via uneven intensification or weakening of the streamwise vorticity.

Special attention was paid to the evolution of the unstable modes, and on their roles in reorganizing the flowfield. We were thus content to observe unstable modes given by a single spanwise wavelength, which was chosen close to the most amplified mode of the linear stability theory. We leave to a subsequent study, the task of trying to determine the characteristics of the processes which lead to the wavelength selection of the 3D modes. Moreover, we have restricted our study to the formation and maturation of the primary 3D structures. We have thus omitted the pairing interactions between these structures and their role in the mixing transition and growth of the layer. These computations are currently considered.

## ACKNOWLEDGEMENT

This work is supported by the Air Force Office of Scientific Research Grant AFOSR 84-0356, the National Science Foundation Grant CBT-8709465, and the Department of Energy Grant DE-FG04-87AL44875. Computer support is provided by the John von Neumann National Supercomputer Center.

## REFERENCES

- Ashurst, W.T. & Meiburg, E. 1988. *J. Fluid Mech.* **189**, 87.
- Batchelor, G.K. 1967. *An Introduction to Fluid Dynamics*. Cambridge University Press.
- Beale, J.T. 1986. *Math. Comput.* **46**, 401.
- Beale, J.T. & Majda, A. 1982a. *Math. Comput.* **39**, 1.
- Beale, J.T. & Majda, A. 1982b. *Math. Comput.* **39**, 29.
- Beale, J.T. & Majda, A. 1985. *J. Comput. Phys.* **58**, 188.
- Bernal, L.P., *The coherent structure of turbulent mixing layers*, Ph.D. Thesis, California Institute of Technology, 1981.
- Bernal, L.P. & Roshko, A. 1986. *J. Fluid Mech.* **170**, 499.
- Breidenthal, R. 1980. *Phys. Fluids* **23**, 1929.
- Breidenthal, R. 1981. *J. Fluid Mech.* **109**, 1.
- Browand, F.K. & Troutt, T.R. 1980. *J. Fluid Mech.* **97**, 771.
- Brown, G.L. & Roshko, A. 1974. *J. Fluid Mech.* **64**, 775.
- Chorin, A.J. 1973. *J. Fluid Mech.* **57**, 785.
- Corcos, G.M. & Lin, S.J. 1984. *J. Fluid Mech.* **139**, 67.
- Crow, S.C. & Champagne, F.H. 1970. *J. Fluid Mech.* **48**, 547.
- Dimotakis, P.E. 1986. *AIAA J.* **24**, 1791.
- Dimotakis, P.E., 1989. "Turbulent free shear layer mixing," AIAA Paper 89-0262.
- Ghoniem, A.F., Heidarinejad, G. & Krishnan, A. 1988. *J. Comput. Phys.* **79**, 135.
- Ghoniem, A.F. & Krishnan, A. 1988. In *Twenty-Second Symposium (International) on Combustion*, The Combustion Institute, 665.
- Greengard, C. 1986. *Math. Comput.* **47**, 387.
- Grinstein, F.F., Hussain, F. & Oran, E.S. 1989. "A numerical study of mixing control in spatially evolving shear flows," AIAA Paper 89-0977.
- Ho, C.-H. & Huerre, P. 1984. *Ann. Rev. Fluid Mech.* **16**, 365.
- Hussain, A.K.M.F. 1986. "Coherent structures and turbulence," *J. Fluid Mech.* **173**, 303.
- Inoue, O. 1989. *AIAA J.* **27**, 1517.

- Jimenez, J. 1983. *J. Fluid Mech.* 132, 319.
- Jimenez, J., Cogollos, M. & Bernal, L.P. 1985. *J. Fluid Mech.* 152, 125.
- Koochesfahani, M.M. & Frierler, C.E. 1989. *AIAA J.* 27, 1735.
- Konrad, J.H., *An experimental investigation of mixing in two-dimensional turbulent shear flows with applications to diffusion-limited chemical reactions*, Ph.D. Thesis, California Institute of Technology, 1976.
- Koop, C.G. & Browand, F.K. 1979. *J. Fluid Mech.* 93, 135.
- Knio, O.M. & Ghoniem, A.F. 1988. "On the formation of streamwise vorticity in turbulent shear flows," AIAA Paper 88-0728.
- Knio, O.M. & Ghoniem, A.F. 1990. *J. Comput. Phys.* 86, 75.
- Knio, O.M. & Ghoniem, A.F. 1991. *J. Comput. Phys.* 97, 172.
- Knio, O.M. & Ghoniem, A.F. 1992. *AIAA J.* 30, 105.
- Krishnan, A. 1989. *Numerical study of vorticity-combustion interactions in shear flow*, Ph.D. Thesis, M.I.T.
- Lasheras, J.C., Cho, J.S. & Maxworthy, T. 1986. *J. Fluid Mech.* 172, 231.
- Lasheras, J.C. & Choi, H. 1988. *J. Fluid Mech.* 189, 53.
- Leonard, A. 1985. *Ann. Rev. Fluid Mech.* 17, 525.
- Lin, S.J. & Corcos, G.M. 1984. *J. Fluid Mech.* 141, 139.
- Lowery, P.S., Reynolds, W.C. & Mansour, N.N. 1987. AIAA Paper 87-0132.
- Majda, A. & Sethian, J.A. 1987. *Comb. Sci. Tech.* 42, 185.
- Maslowe, S.A. & Kelly, R.E. 1971. *J. Fluid Mech.* 48, 405.
- McMurtry, P.A., Riley, J.J. & Metcalfe, R.W. 1989. *J. Fluid Mech.* 199, 297.
- Metcalfe, R.W., Orszag, S.A., Brachet, M.E., Menon, S. & Riley, J.J. 1987. *J. Fluid Mech.* 184, 207.
- Neu, J.C. 1984. *J. Fluid Mech.* 143, 253.
- Pierrehumbert, R.T. & Widnall, S.E. 1982. *J. Fluid Mech.* 114, 59.
- Rehm, R.G. & Baum, H.R. 1978. *J. Res. N.B.S.* 83, 297.
- Riley, J.J. & McMurtry, P.A. 1989. In *Turbulent Reactive Flows*, R. Borghi & S.N.B. Murthy, eds., Springer-Verlag, 486.
- Widnall, S.E. & Tsai, C.-Y. 1977. *Proc. Roy. Soc. London A* 287, 273.



Winant, C.D. & Browand, F.K. 1974. *J. Fluid Mech.* **41**, 327.

Wynanski, I., Oster, D., Fiedler, H. & Dziomba, B. 1979. *J. Fluid Mech.* **93**, 325.

## FIGURE CAPTIONS

Figure 1. (a) Schematic representation of the shear layer, the coordinate axes, and the initial vorticity and scalar distributions, showing the shape of the perturbation, and the initial location of the vortex tubes. (b) Vorticity and velocity profiles for the symmetric and asymmetric layers discussed in Sections 3.1 and 3.3 respectively.

Figure 2. Three-dimensional perspective view of the  $s = 0$ , initially lying in the plane  $z = 0$ . The plots were generated from the point of view of an observer located at (48,24,48).  $x$ - is the streamwise direction,  $y$ - the spanwise direction, and  $z$ - is the cross-stream direction.

Figure 3. Three-dimensional perspective view of the iso-scalar surface (a) initially lying in the plane  $z = -1.32$ , (b) embedded in the middle layer and coinciding with the axis of the spanwise core, and (c) embedded in the middle layer and located within the braids. The plots are generated as in Figure 1.

Figure 4. Intersection of the Lagrangian mesh at  $t = 18.0$  with the planes (a)  $y = 3.3$ , (b)  $y = 1.6$ , (c)  $x = 6.6$ , and (d)  $x = 2.0$ . The intersection points are illustrated in terms of small circles whose radius is  $1/8$  of the core radius of the transport elements.

Figure 5. Schematic illustration of the evolution of the scalar distribution in the streamwise plane dividing the spanwise eddy core.

Figure 6. (a) Contours of constant spanwise vorticity,  $\omega_y$ , and (b) iso-scalar contours plotted in the plane  $y = 3.3$ .

Figure 7. (a) Contours of constant spanwise vorticity,  $\omega_y$ , and (b) iso-scalar contours plotted in the  $x$ - $z$  plane  $y = 5.0$ .

Figure 8. (a) Contours of constant streamwise vorticity,  $\omega_x$ , and (b) iso-scalar contours plotted in the plane  $x = 6.6$ .

Figure 9. (a) Contours of constant streamwise vorticity,  $\omega_x$ , and (b) iso-scalar contours plotted in the plane  $x = 2.0$ .

Figure 10. Evolution of the total streamwise vorticity,  $\int |\omega_x| dA$ , computed in the streamwise plane located at  $x = 6.6$ .

Figure 11. Schematic illustration of the eddy.

Figure 12. Evolution of the eddy size in two dimensions,  $S_{2D}$  (v), and in three dimensions,  $S_{3D}$  (^), and  $S'_{3D}$  (\*).

Figure 13. Three-dimensional perspective view of the surface  $\rho' = 0$ , initially lying in the plane  $z = 0$  for the case of a variable-density shear layer. The plots were generated from the point of view of an observer located at (48,24,48).

Figure 14. Intersection of the Lagrangian mesh at  $t = 16.0$  with the planes (a)  $y = 3.3$ , (b)  $y = 1.6$ , (c)  $x = 9.3$ , and (d)  $x = 2.0$ .

Figure 15. Contours of spanwise vorticity,  $\omega_y$ , (left) and density (right) plotted in the plane  $y = 3.3$ .

Figure 16. Contours of spanwise vorticity,  $\omega_y$ , (left) and density (right) plotted in the plane  $y = 5.0$ .

Figure 17. Contours of streamwise vorticity,  $\omega_x$ , (left) and density (right) plotted at  $t = 12.0$ , and  $16.0$ , in the planes  $x = 8.6$ , and  $x = 9.3$  respectively.

Figure 18. Contours of streamwise vorticity,  $\omega_x$ , (left) and density (right) plotted in the plane  $x = 2.0$ .

Figure 19. Contours of the spanwise component of the baroclinic torque,  $\tau_y$ , plotted in the plane (a)  $y = 3.3$  and (b)  $y = 5.0$ .

Figure 20. Contours of the streamwise component of the baroclinic torque,  $\tau_x$ , plotted at  $t = 8.0$  and  $16.0$ , in  $y$ - $z$  planes given by (a)  $x = 8.0$  and  $9.3$ ; and (b)  $x = 2.0$ .

Figure 21. Three-dimensional perspective view of the surface  $s = 0$ , initially lying in the plane  $z = 0$  for the shear layer with an initially asymmetric vorticity. The plots were generated from the point of view of an observer located at  $(48, 24, 48)$ .

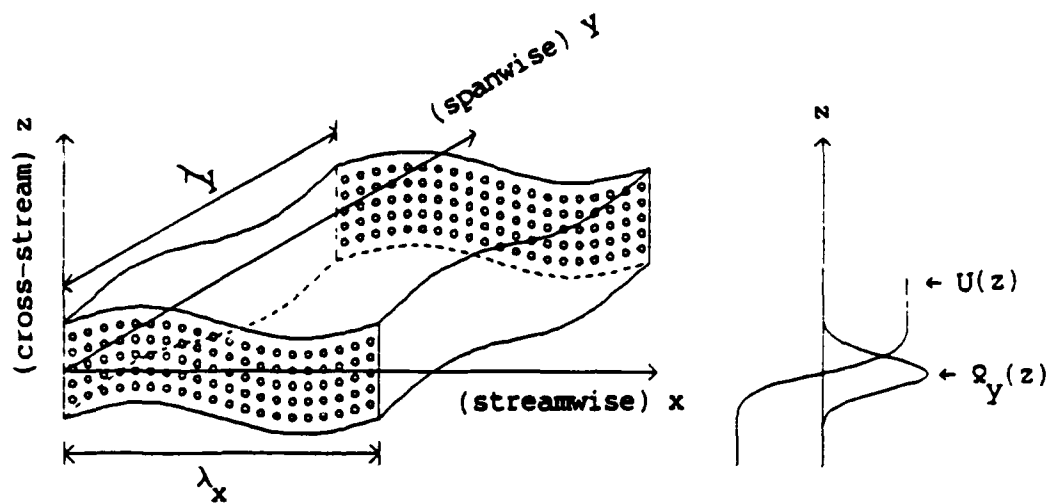
Figure 22. Intersection of the Lagrangian mesh at  $t = 16.0$  with the planes defined by (a)  $y = 3.3$ , (b)  $y = 1.6$ , (c)  $x = 6.6$ , and (d)  $x = 2.0$ .

Figure 23. Spanwise vorticity,  $\omega_y$ , (left) and scalar contours (right) plotted in the plane  $y = 3.3$ .

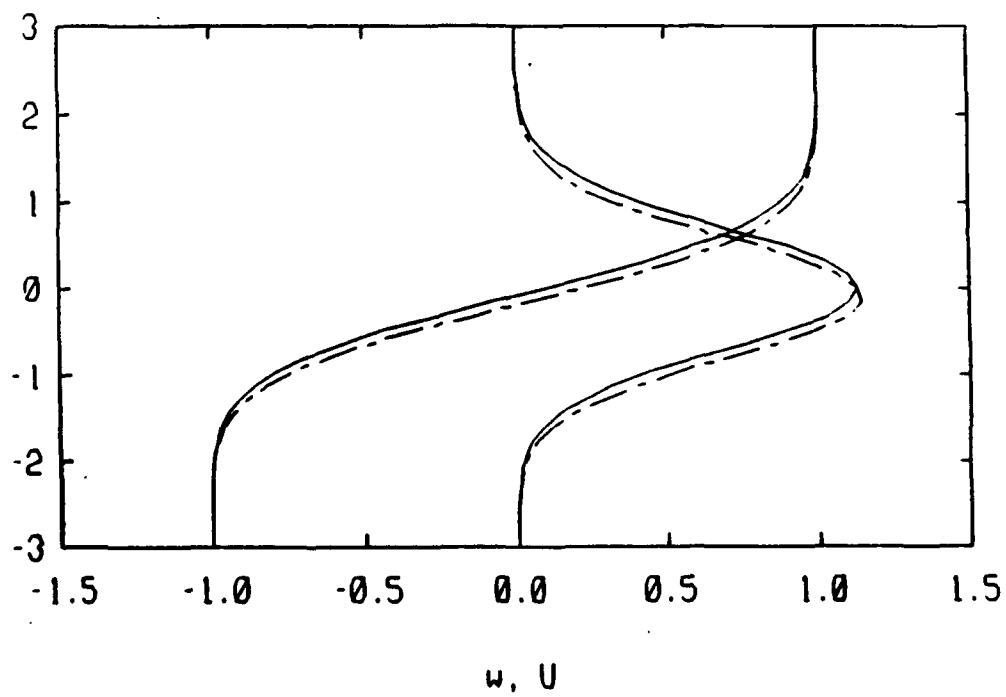
Figure 24. Spanwise vorticity,  $\omega_y$ , (left) and scalar contours (right) plotted in the plane  $y = 5.0$ .

Figure 25. Streamwise vorticity,  $\omega_x$ , (left) and scalar contours (right) plotted in the plane  $x = 6.6$ .

Figure 26. Streamwise vorticity,  $\omega_x$ , (left) and scalar contours (right) plotted in the plane  $x = 2.0$ .

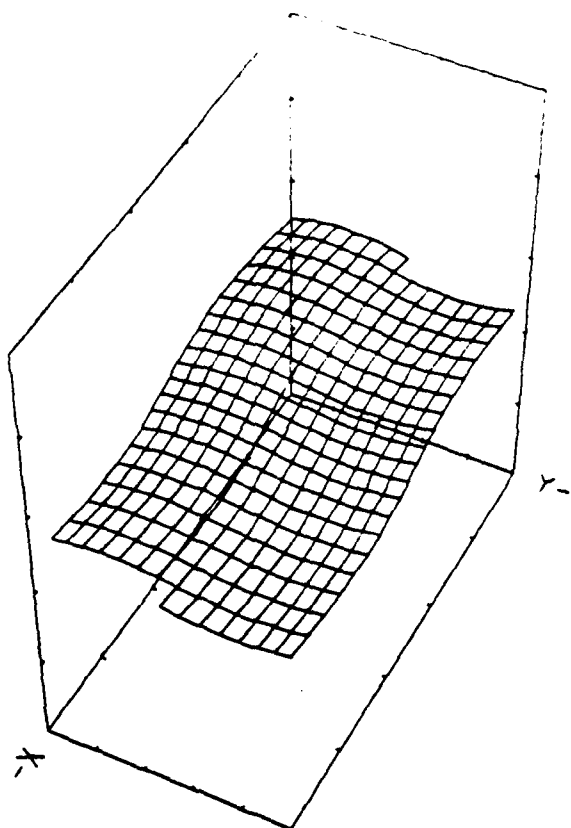


(a)

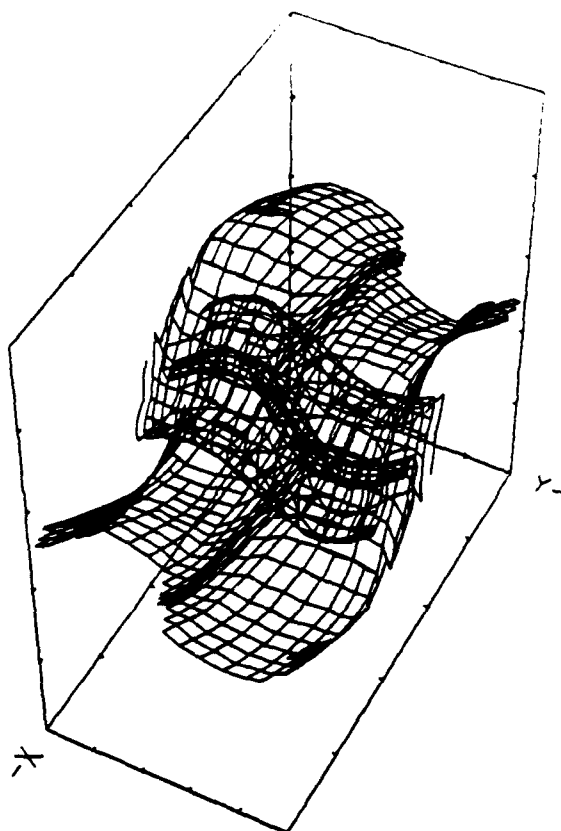


(b)

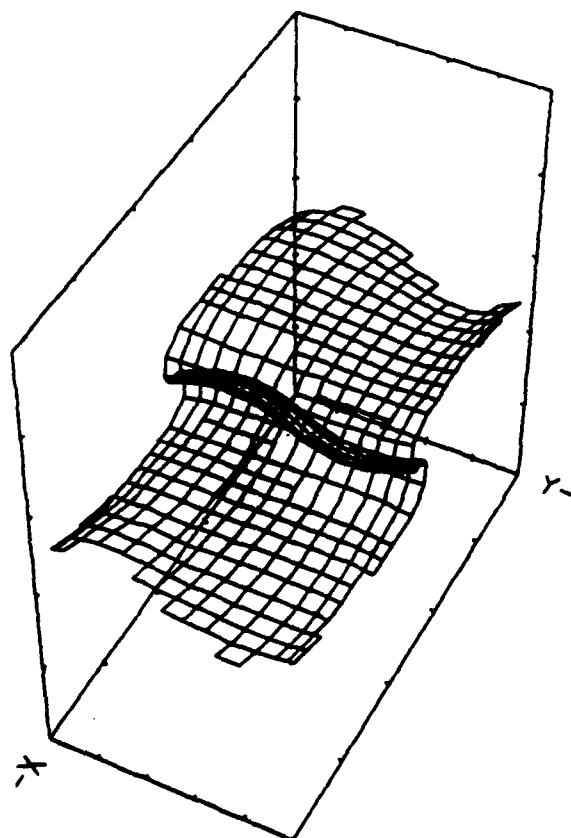
Figure 1



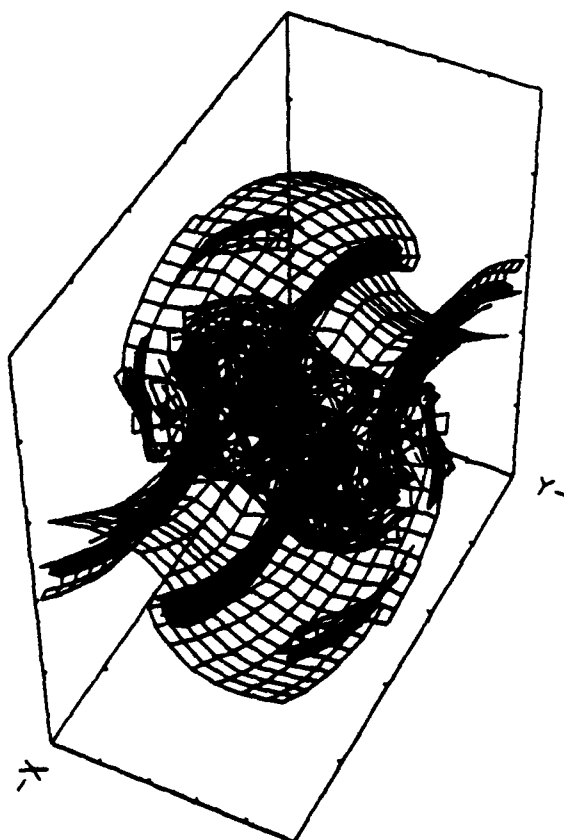
$t = 4.0$



$t = 12.0$

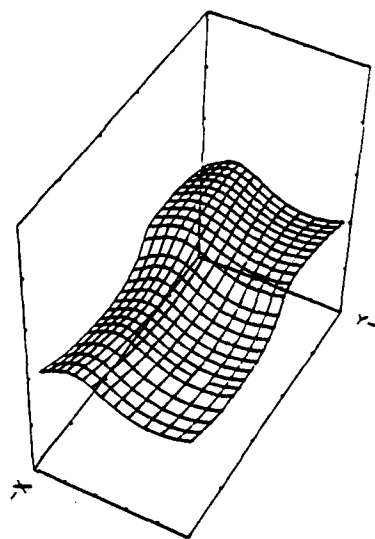


$t = 8.0$



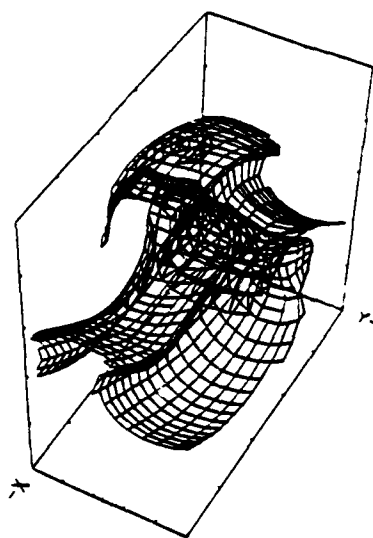
$t = 16.0$

Figure 2

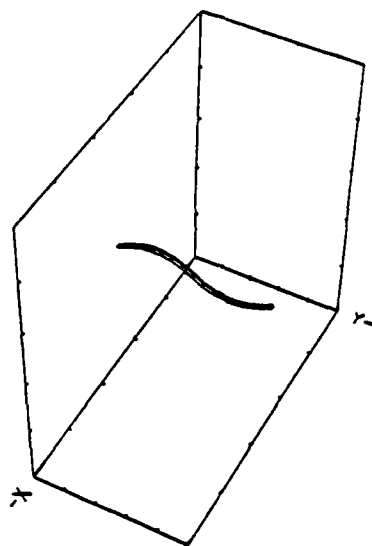


$t = 8.0$

(a)

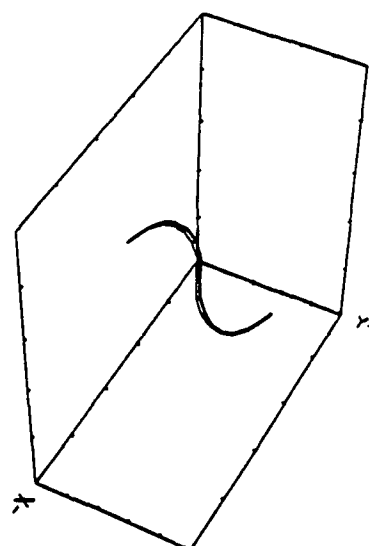


$t = 16.0$

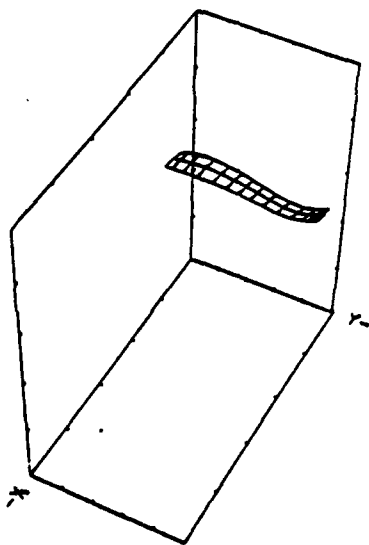


$t = 8.0$

(b)

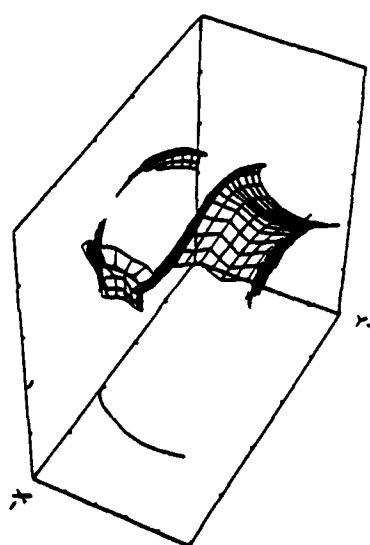


$t = 16.0$



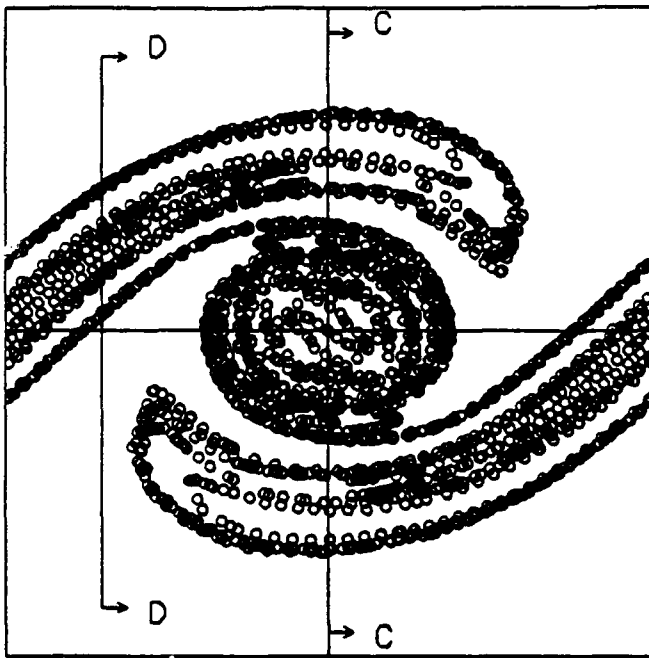
$t = 8.0$

(c)

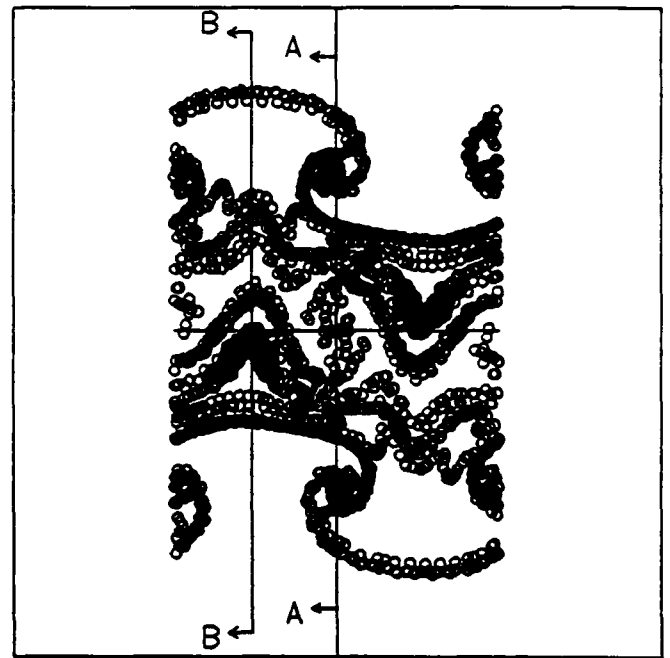


$t = 16.0$

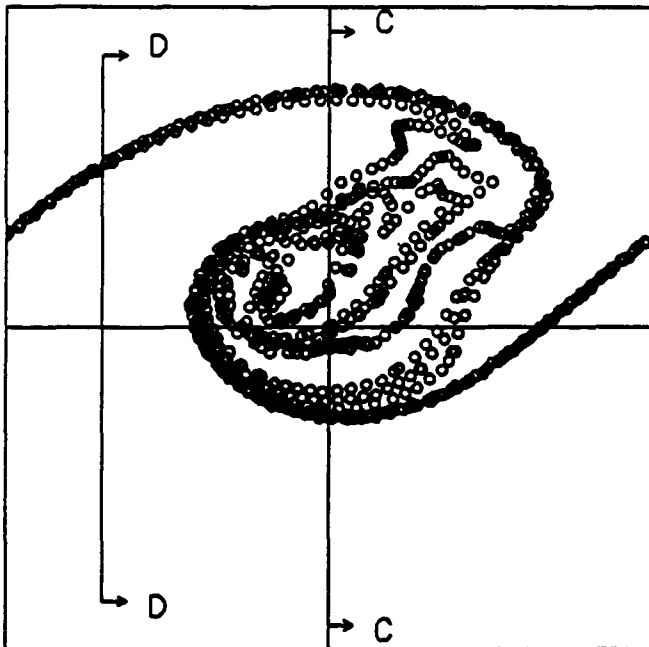
Figure 3



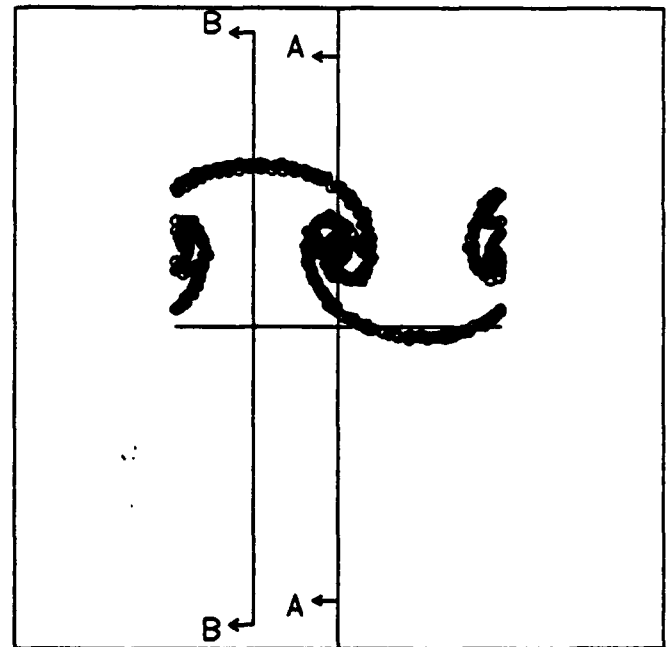
(a)  $y = 3.3$ , (AA).



(c)  $x = 6.6$ , (CC).

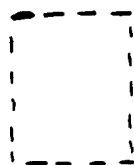
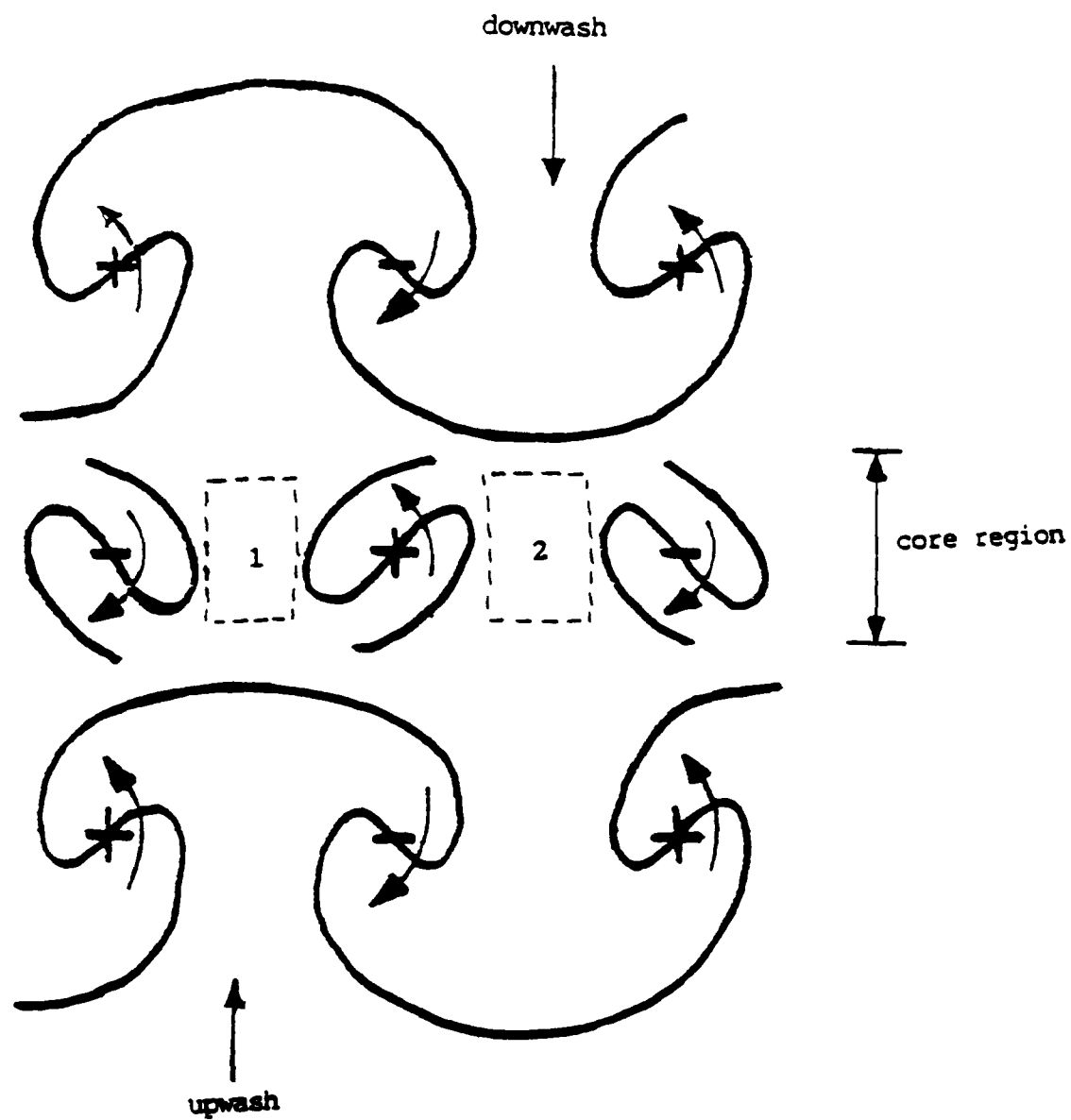


(b)  $y = 1.6$ , (BB).



(d)  $x = 2.0$ , (DD).

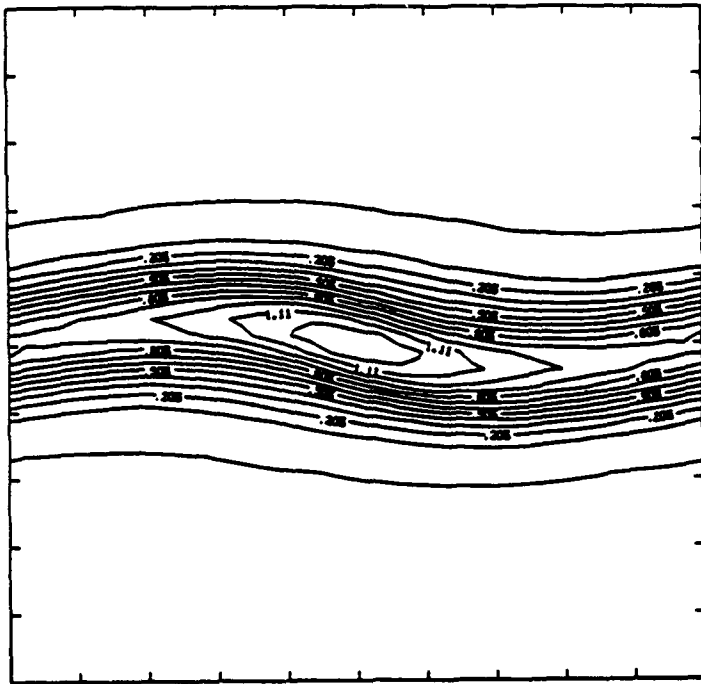
Figure 4



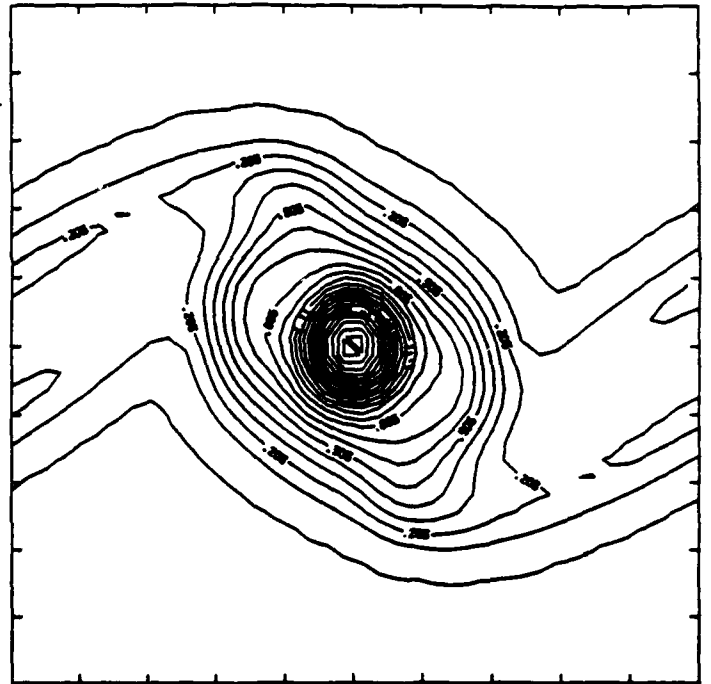
- core leaves the plane of the figure: 1 - outwards, 2 - inwards

Figure 5

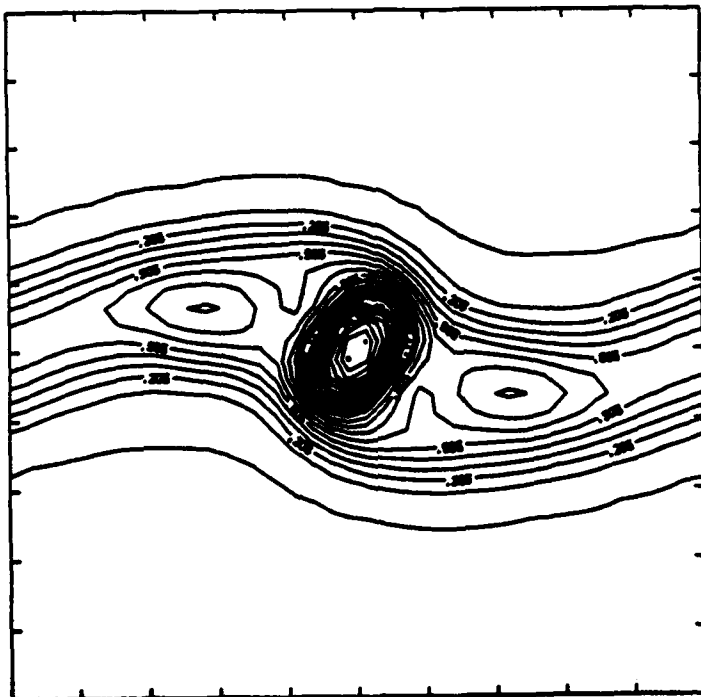




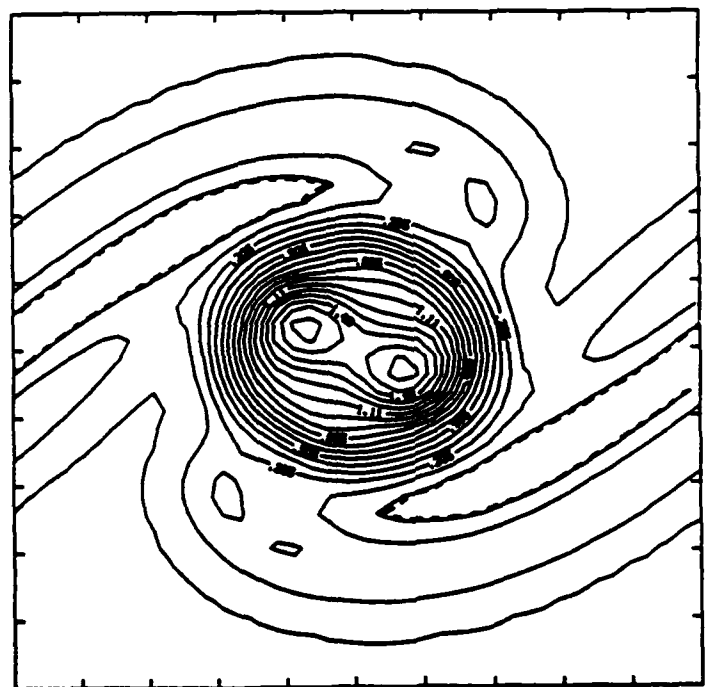
$t = 4.0$



$t = 12.0$

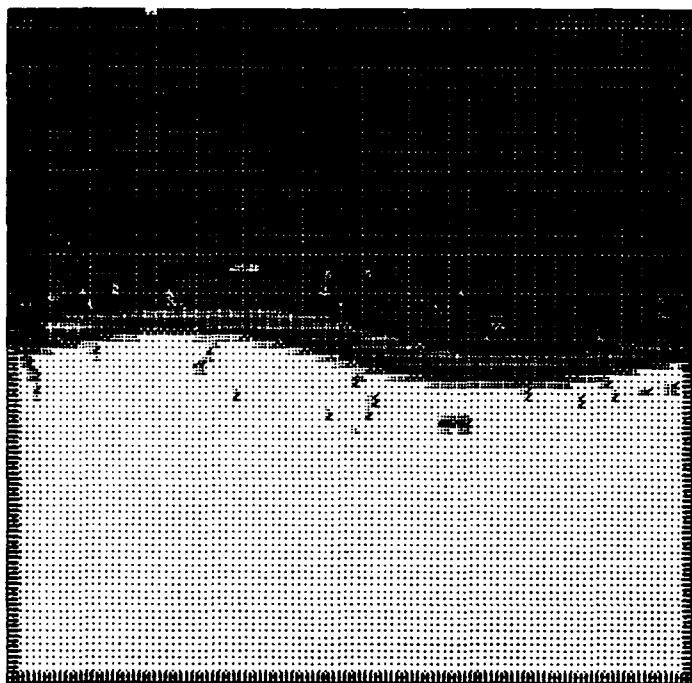


$t = 8.0$



$t = 16.0$

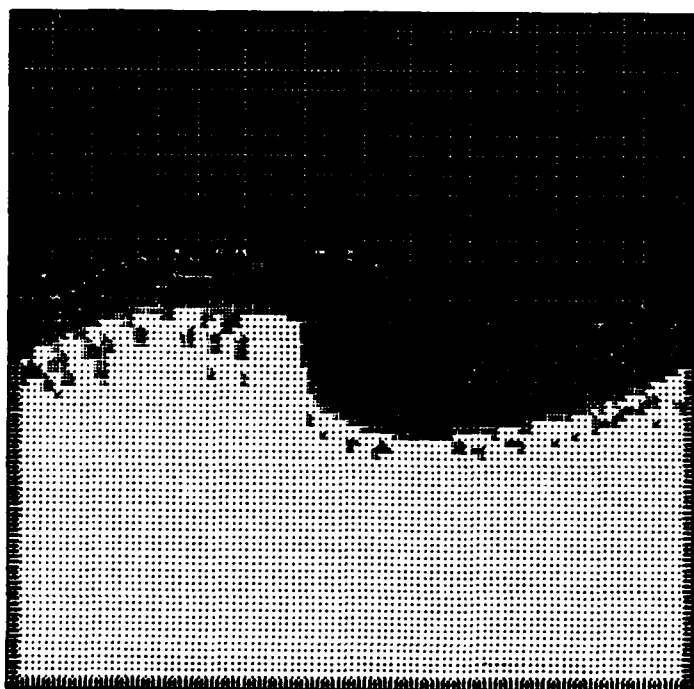
Figure 6 (a)



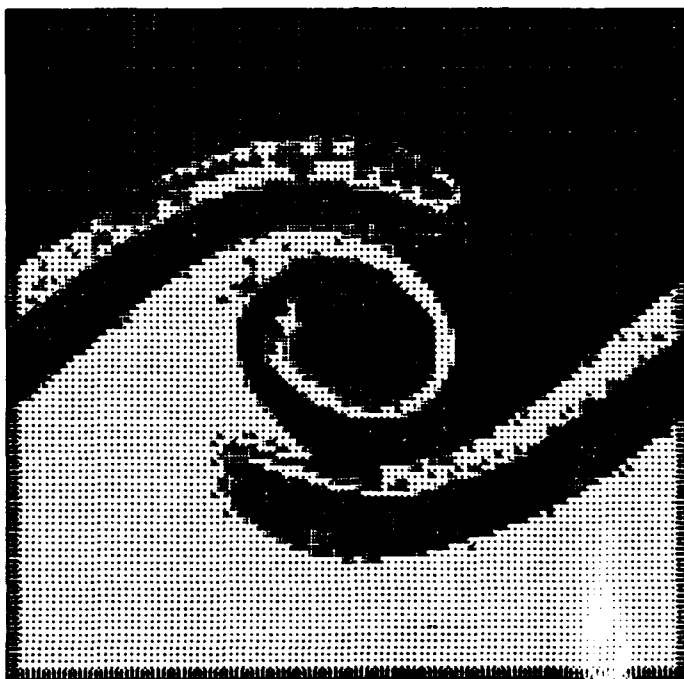
$t = 4.0$



$t = 12.0$

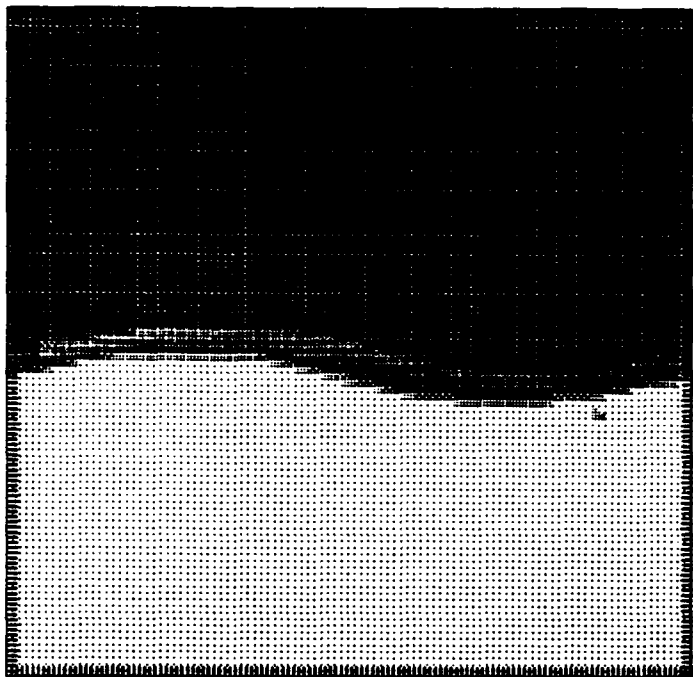


$t = 8.0$

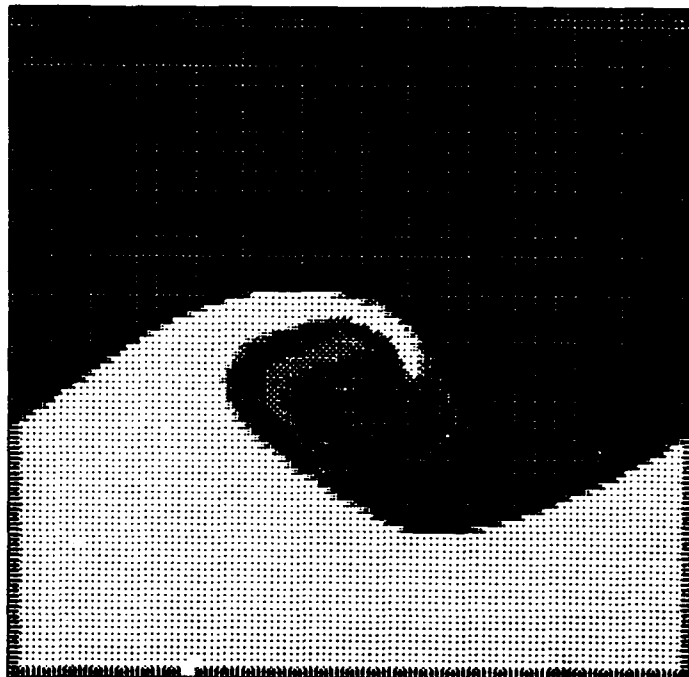


$t = 16.0$

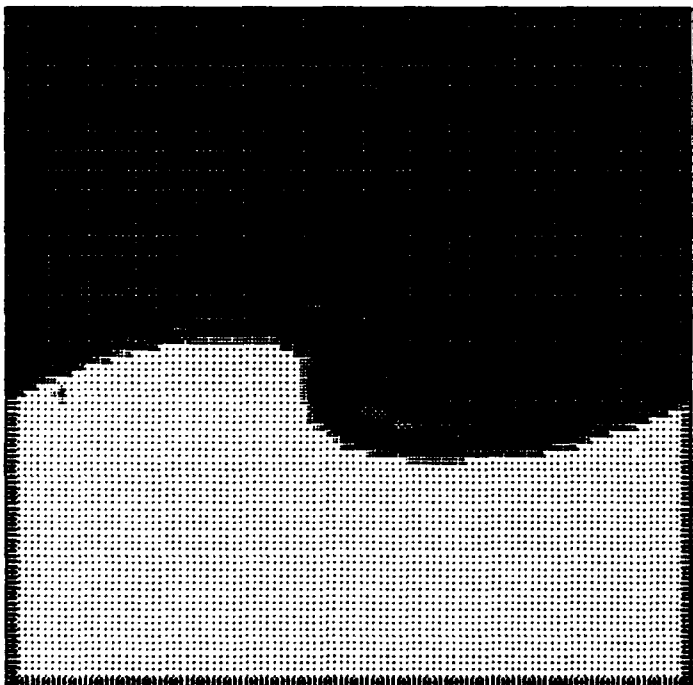
Figure 6 (b)



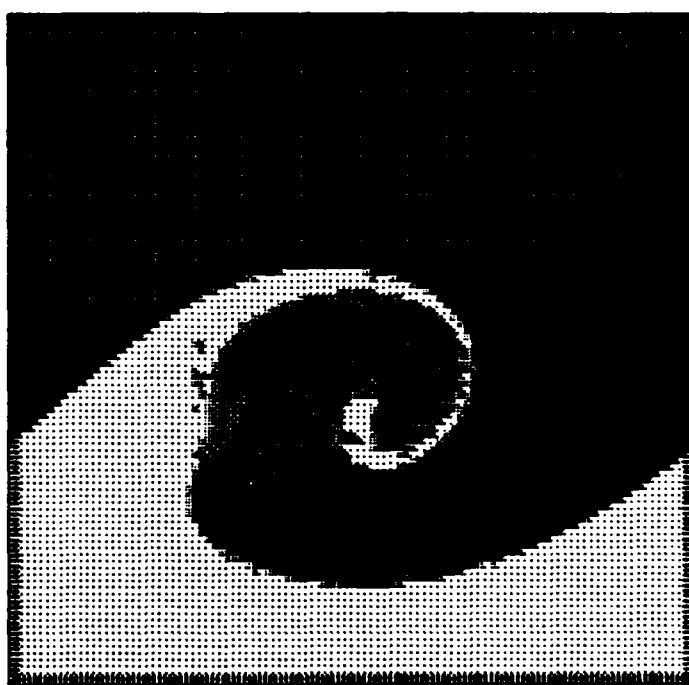
$t = 4.0$



$t = 12.0$

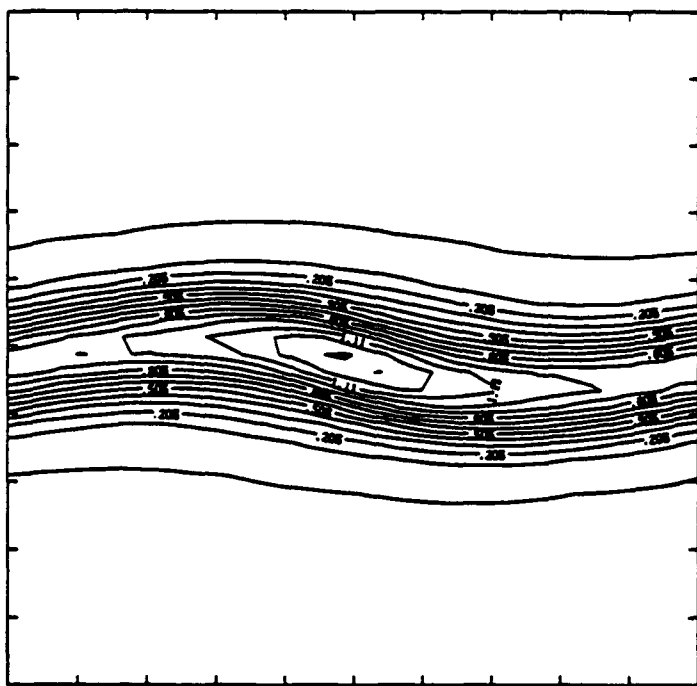


$t = 8.0$

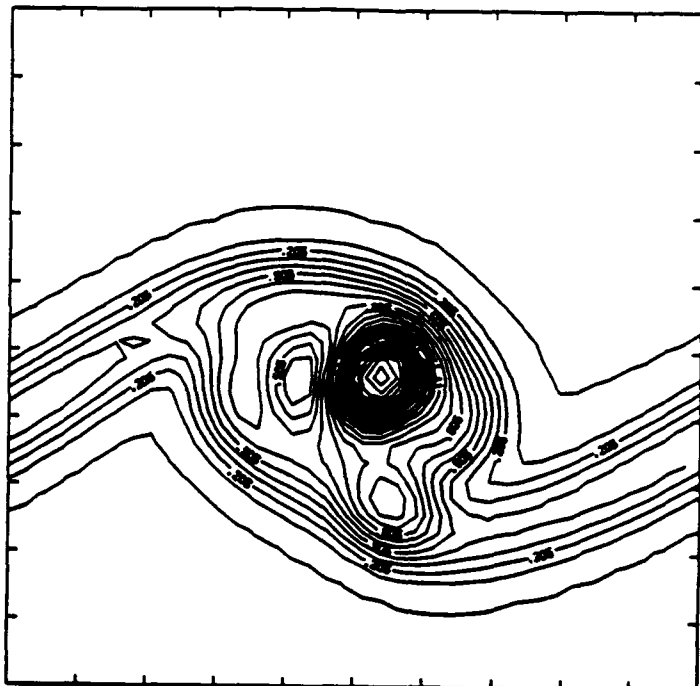


$t = 16.0$

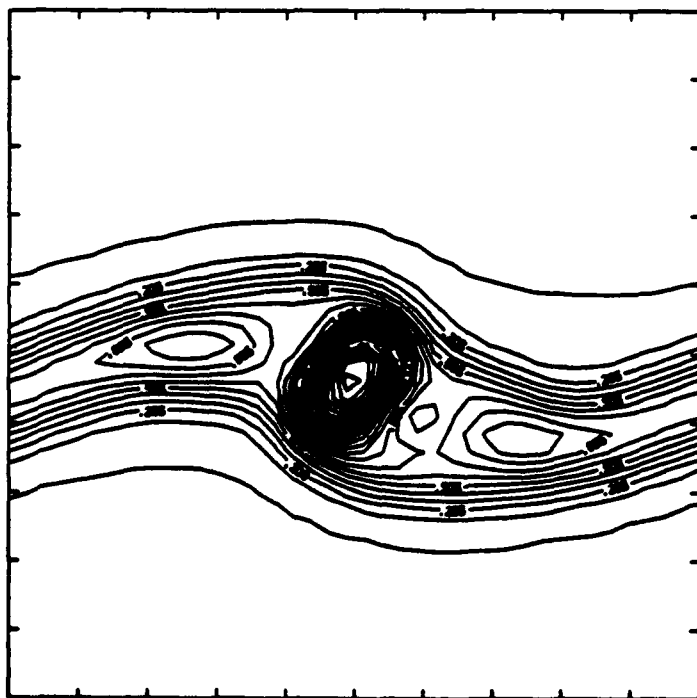
Figure 7 (b)



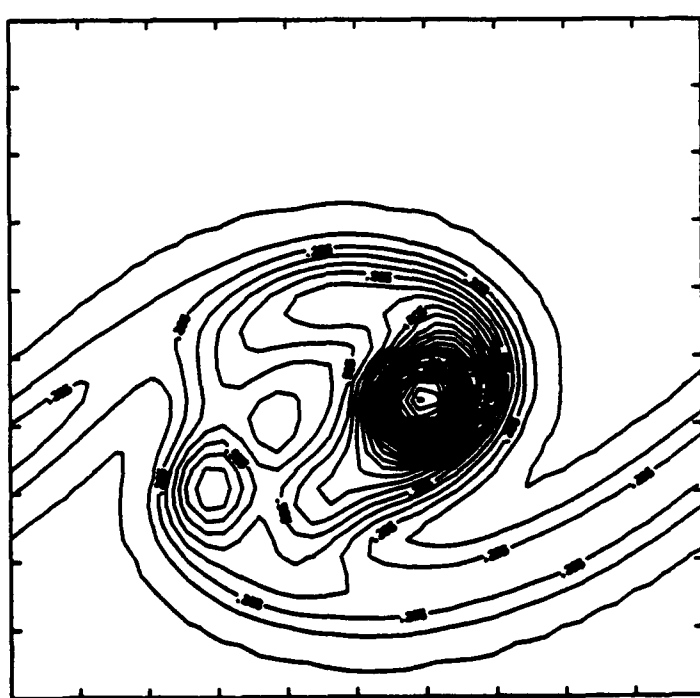
$t = 4.0$



$t = 12.0$

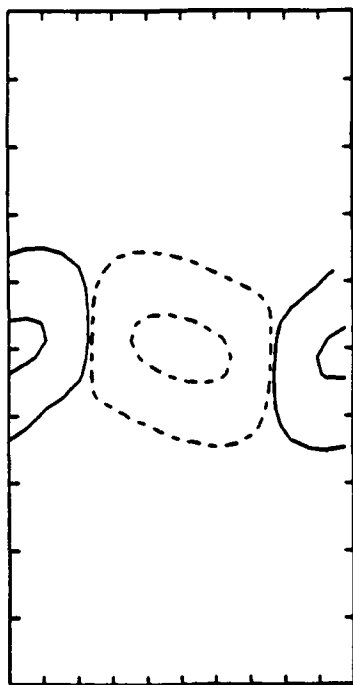


$t = 8.0$

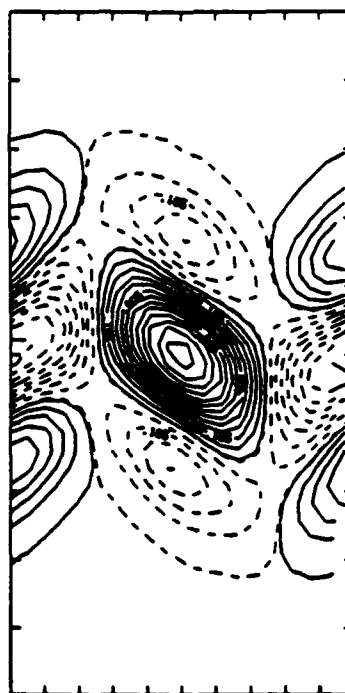


$t = 16.0$

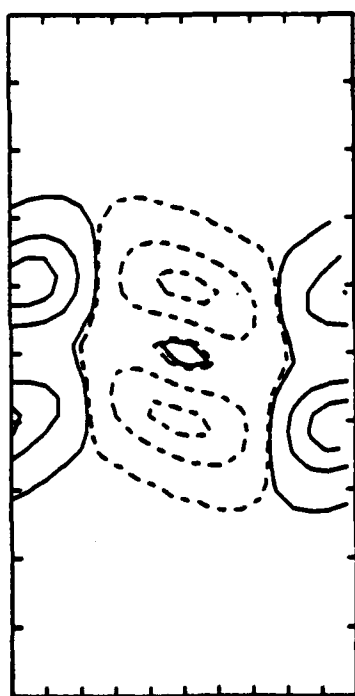
Figure 7 (a)



$t = 4.0$



$t = 12.0$

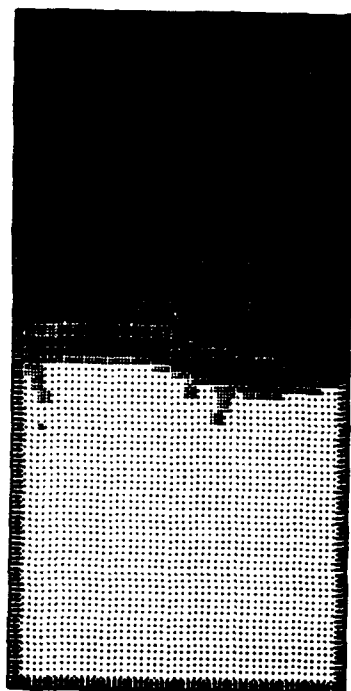


$t = 8.0$



$t = 16.0$

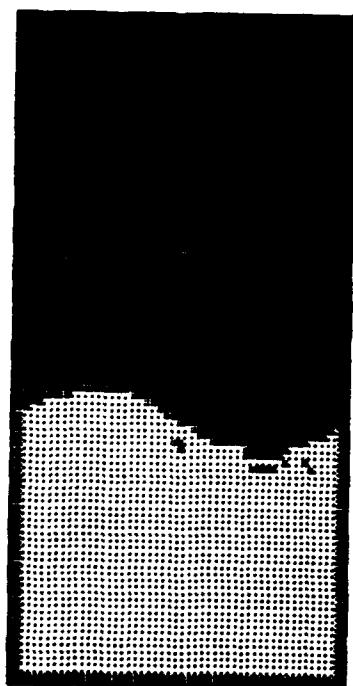
Figure 2 (a)



$t = 4.0$



$t = 12.0$

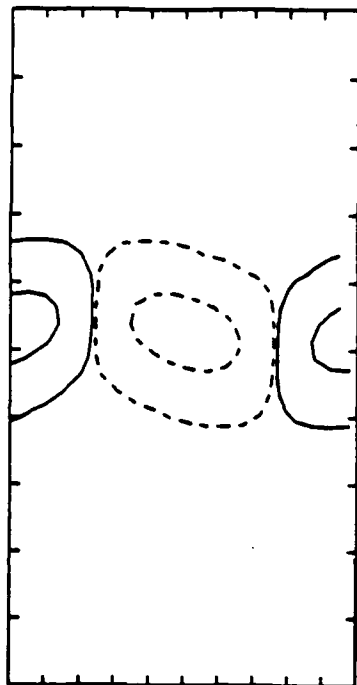


$t = 8.0$

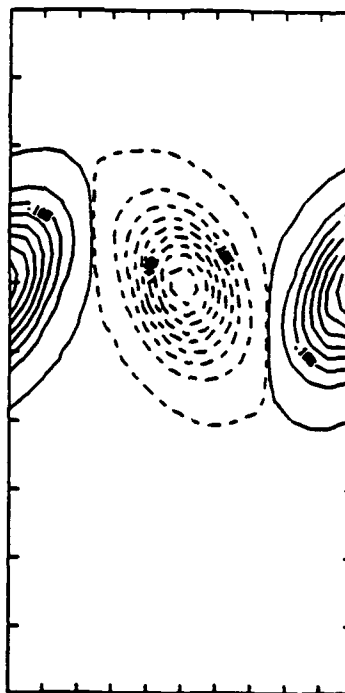


$t = 16.0$

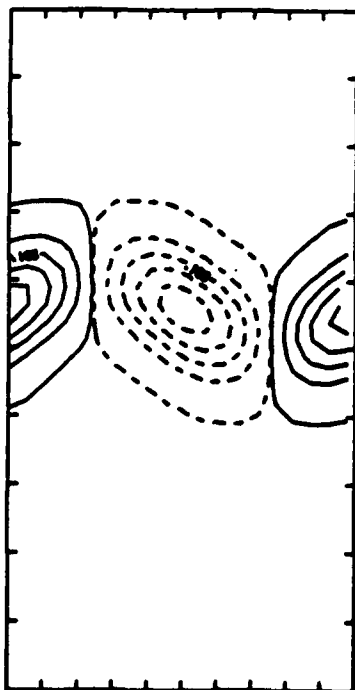
Figure 8. (b)



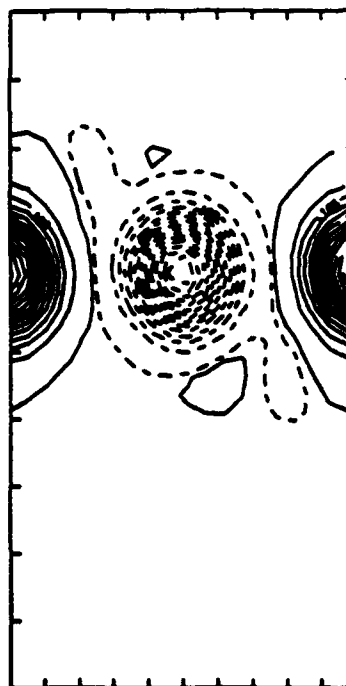
$t = 4.0$



$t = 12.0$

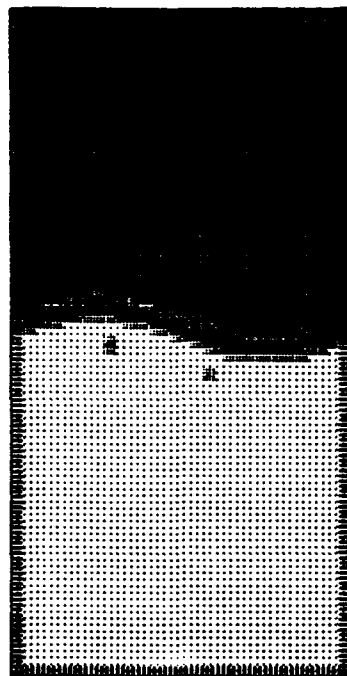


$t = 8.0$

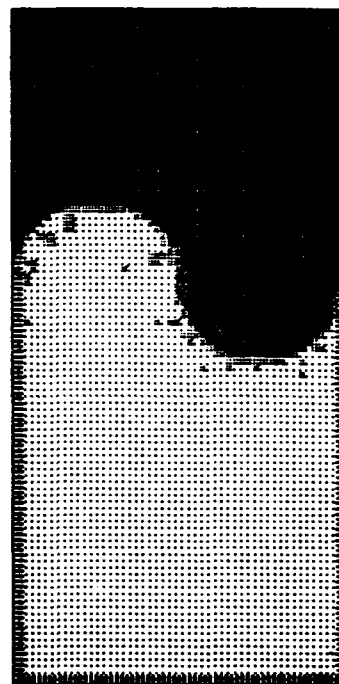


$t = 16.0$

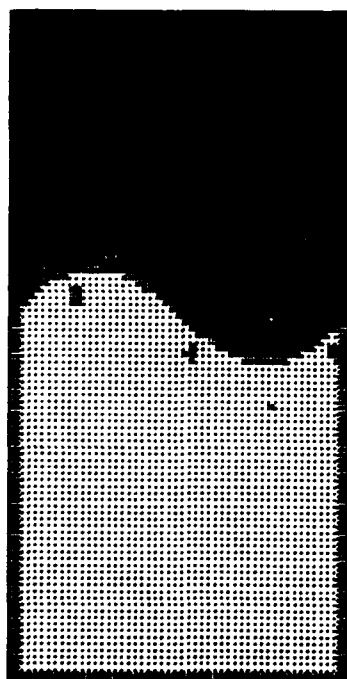
Figure 9 (a)



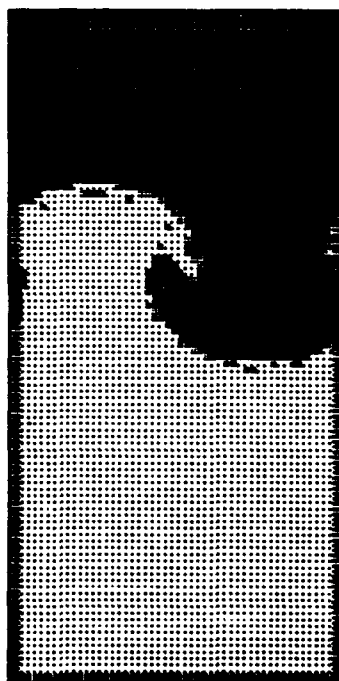
$t = 4.0$



$t = 12.0$



$t = 8.0$



$t = 16.0$

Figure 9 (b)



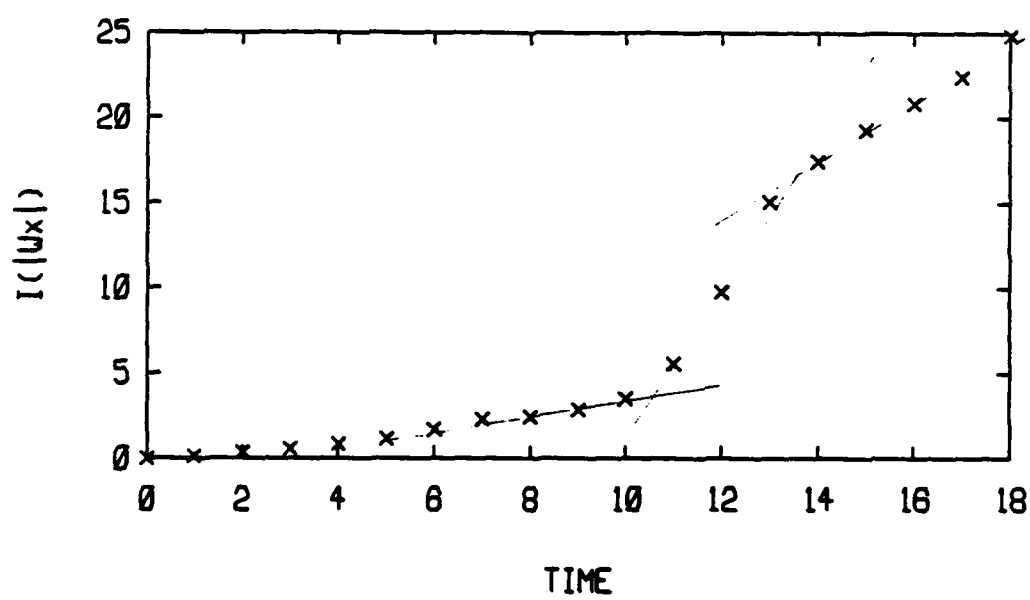


Figure 10

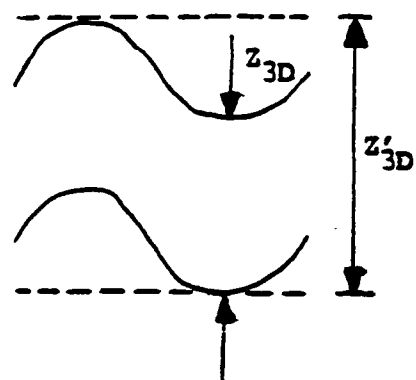
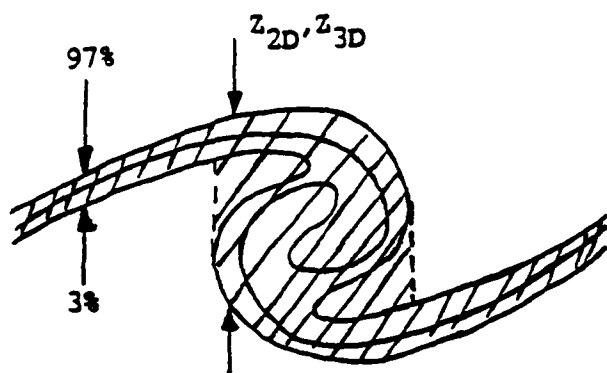


Figure 11

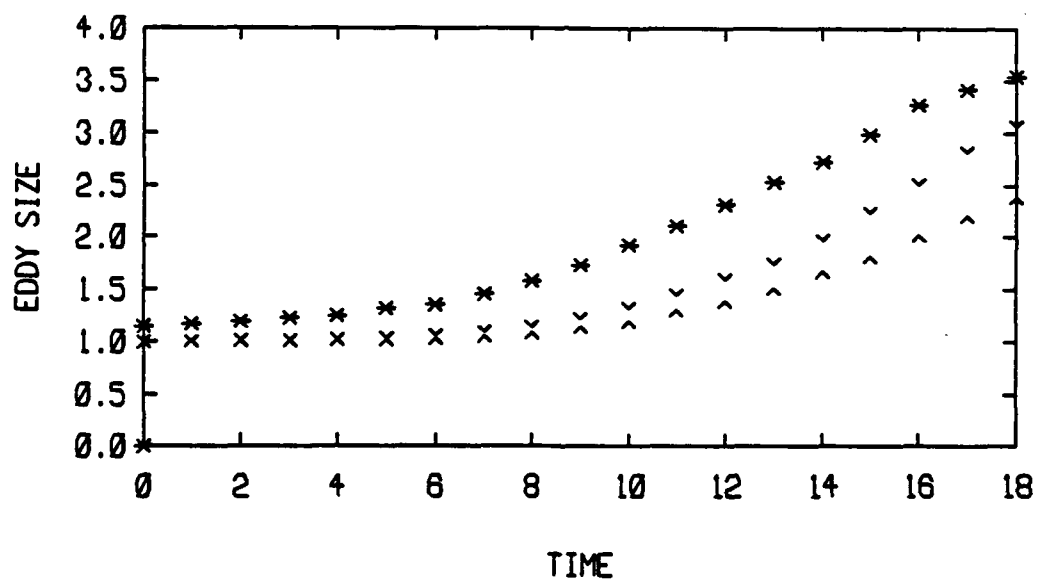
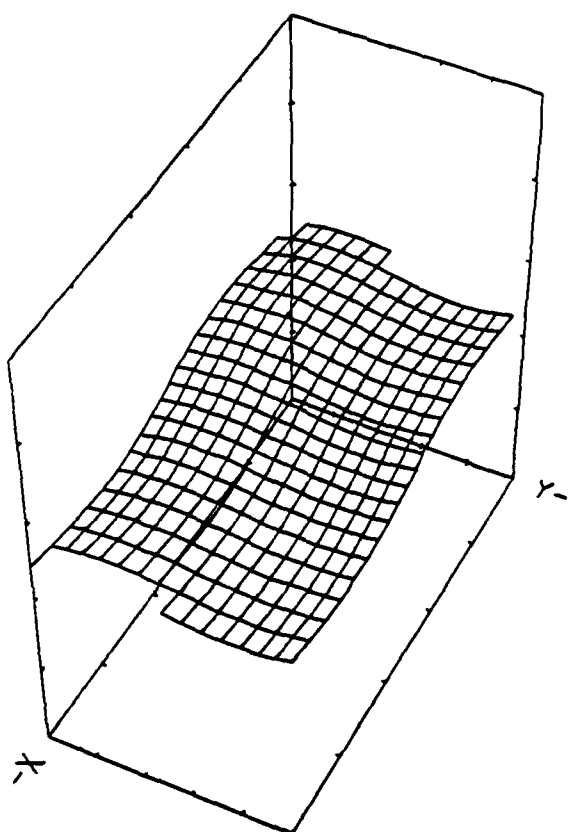
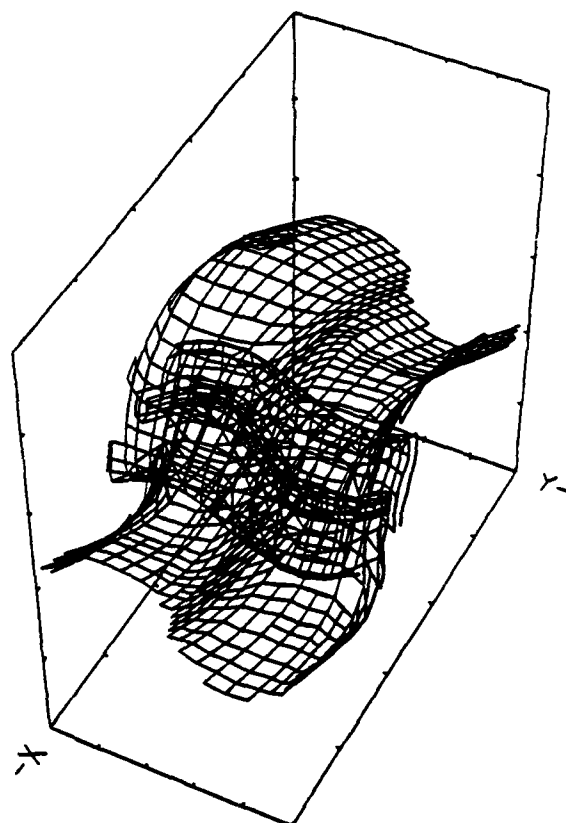


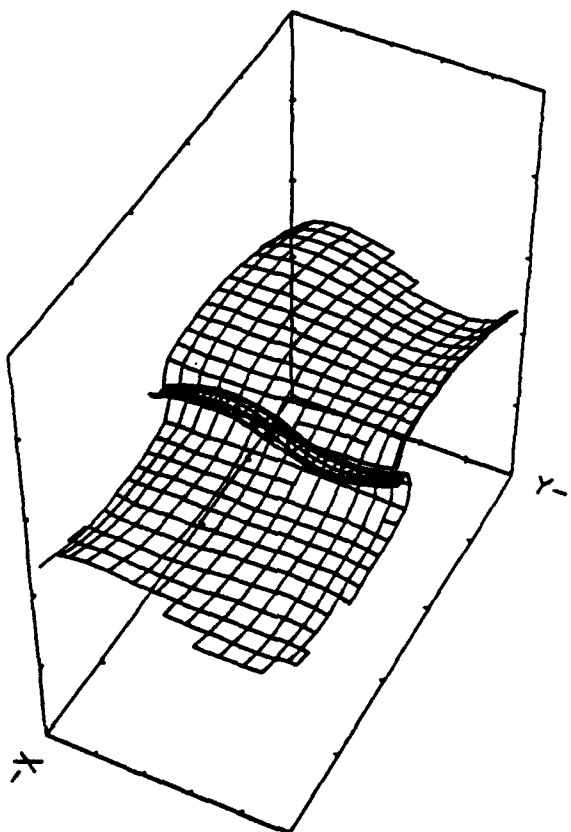
Figure 12



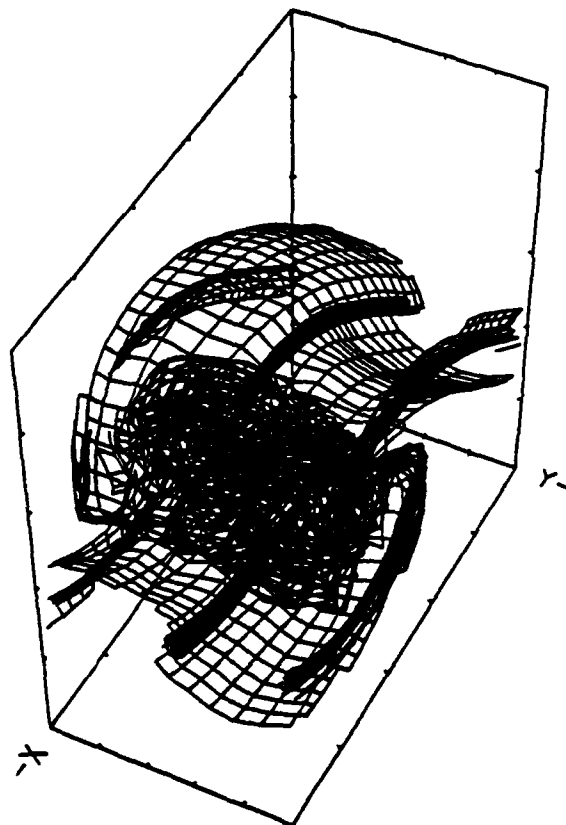
$t = 4.0$



$t = 12.0$

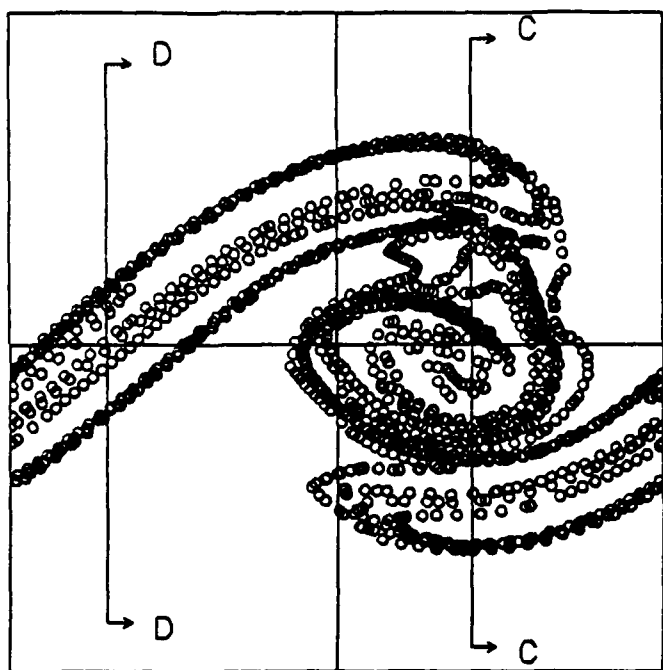


$t = 8.0$

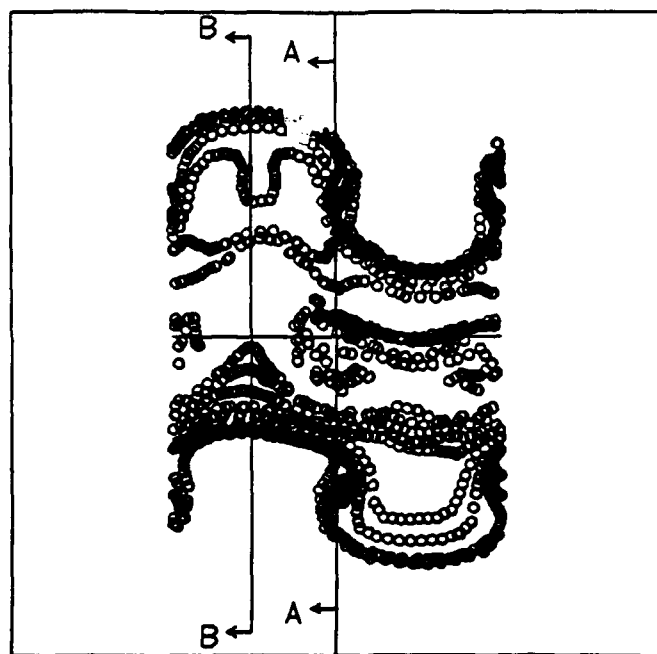


$t = 16.0$

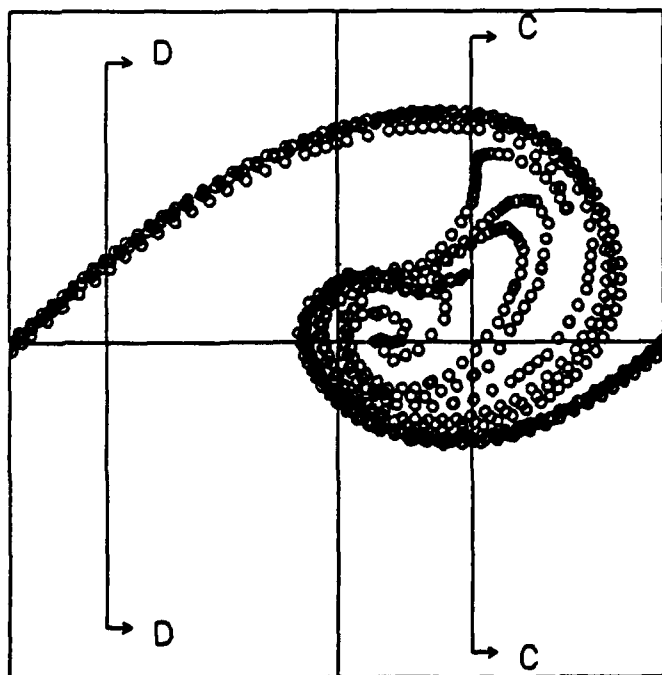
Figure 13



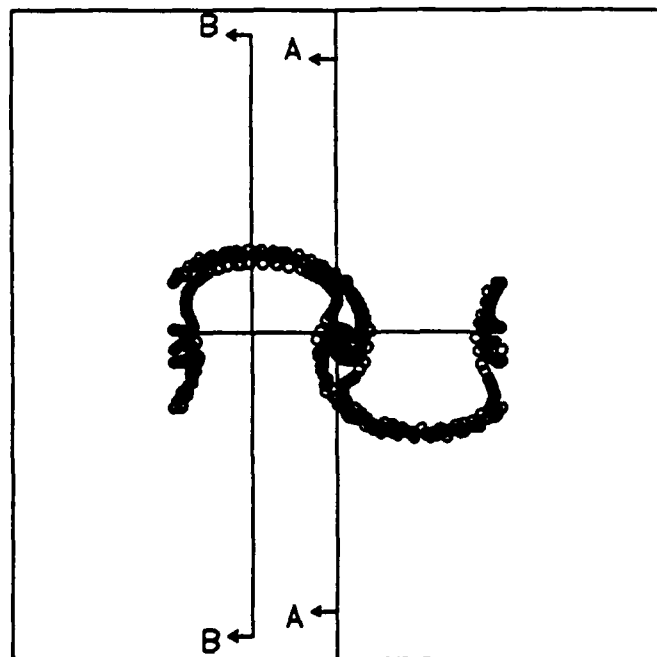
(a)  $y = 3.3$ , (AA).



(c)  $x = 9.3$ , (CC).

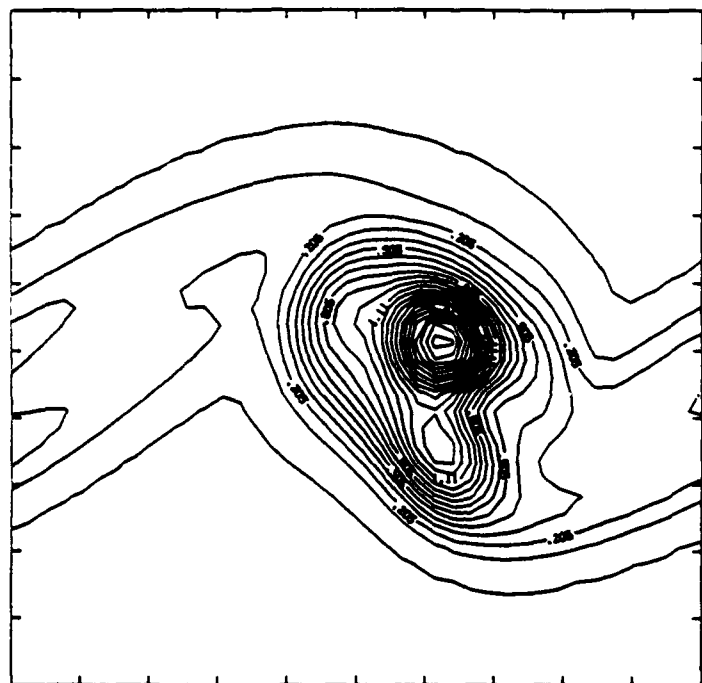


(b)  $y = 1.6$ , (BB).

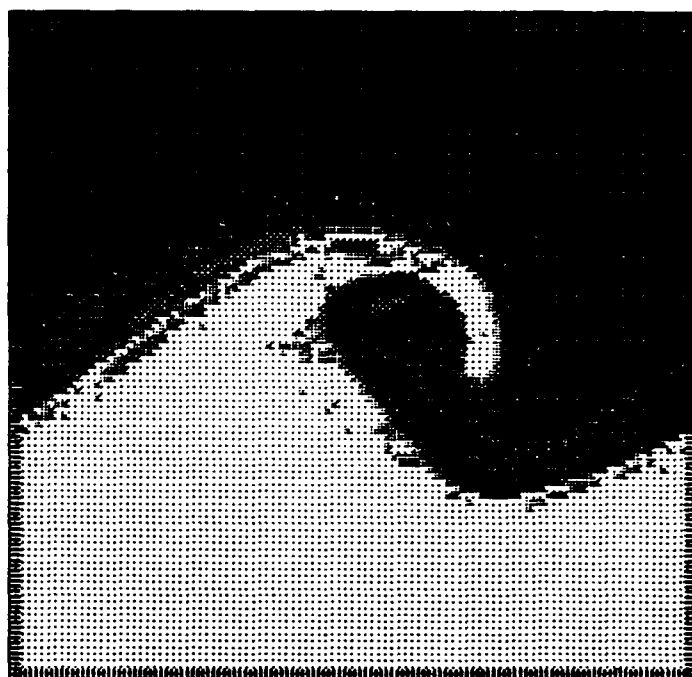


(d)  $x = 2.0$ , (DD).

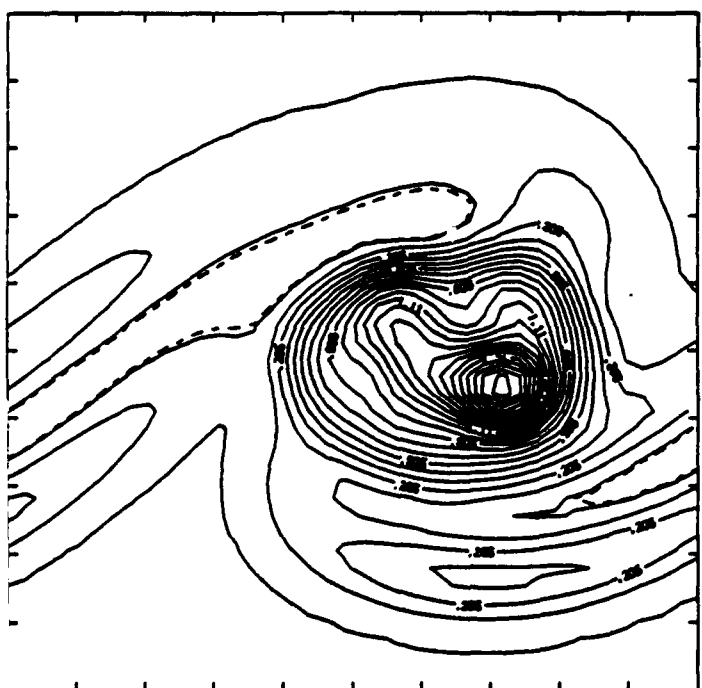
Figure 14



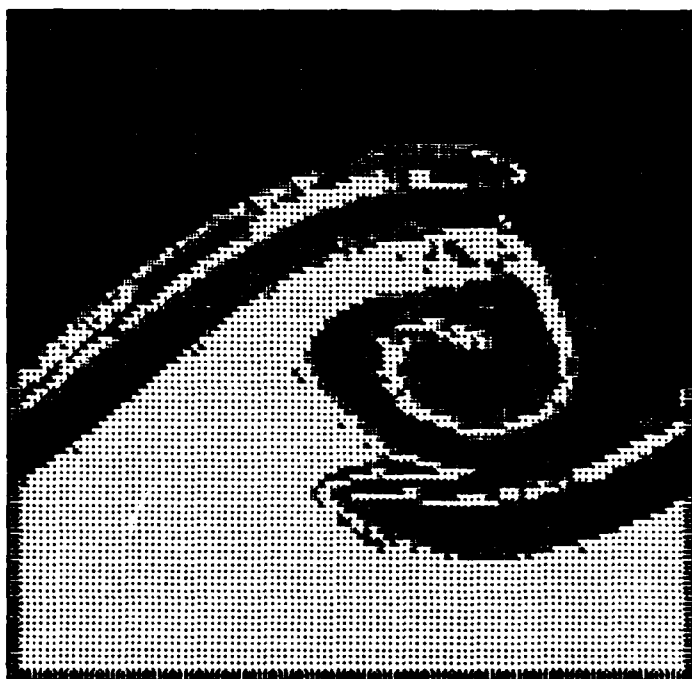
$t = 12.0$



$t = 12.0$

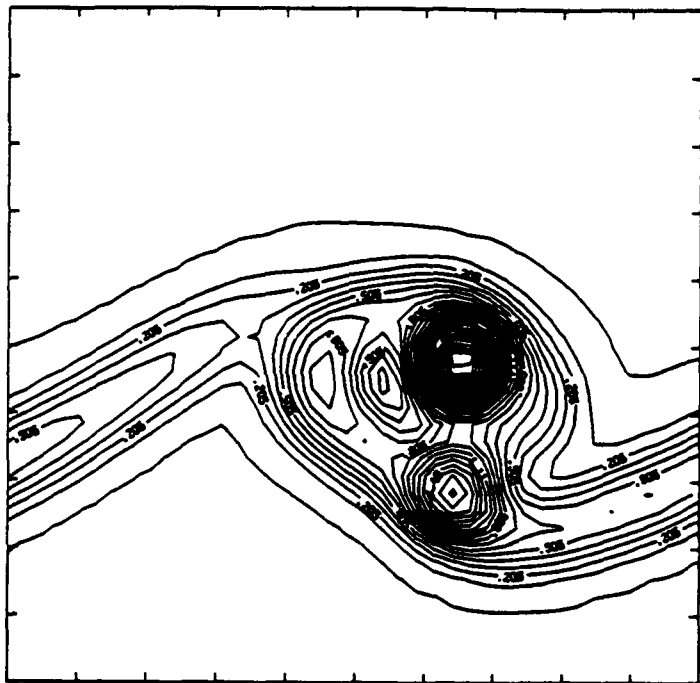


$t = 16.0$

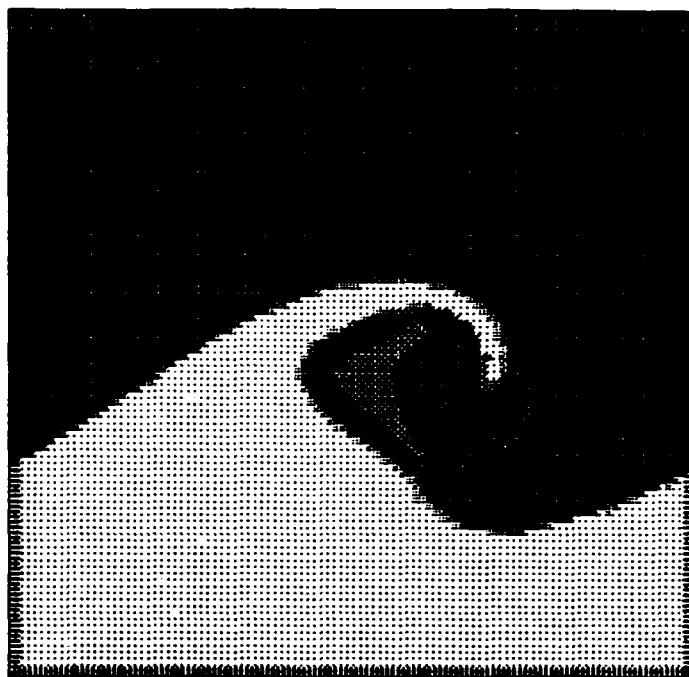


$t = 16.0$

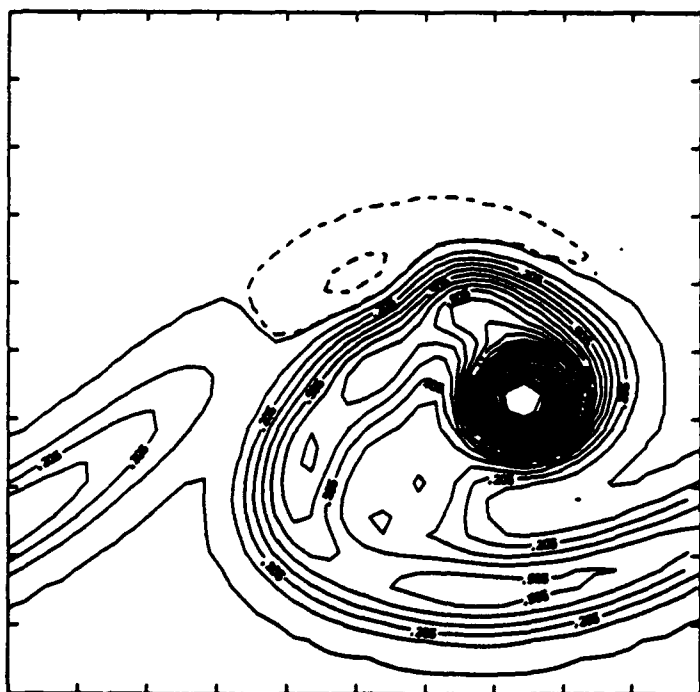
Figure 15



$t = 12.0$



$t = 12.0$

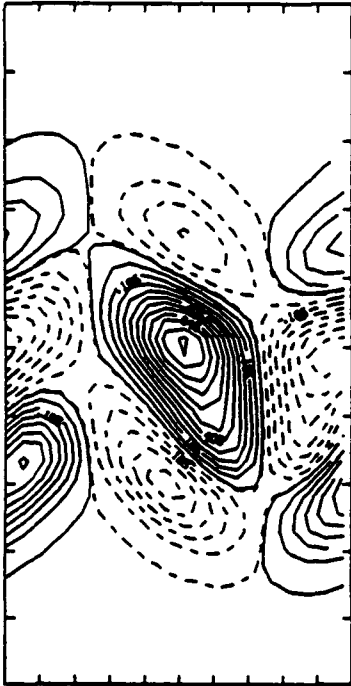


$t = 16.0$



$t = 16.0$

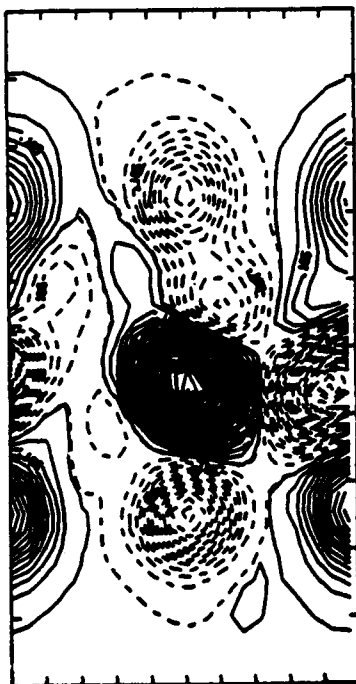
Figure 16



$t = 12.0$



$t = 12.0$



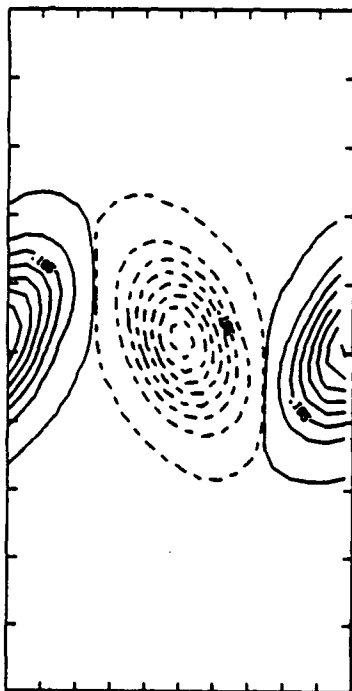
$t = 16.0$



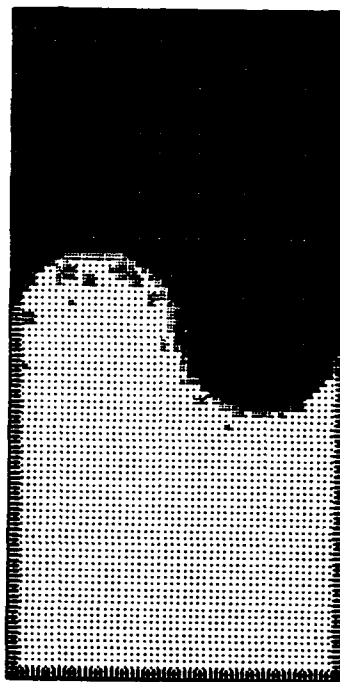
$t = 16.0$

Figure 17

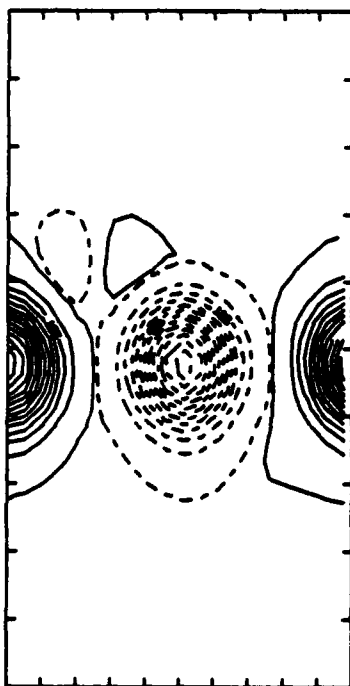




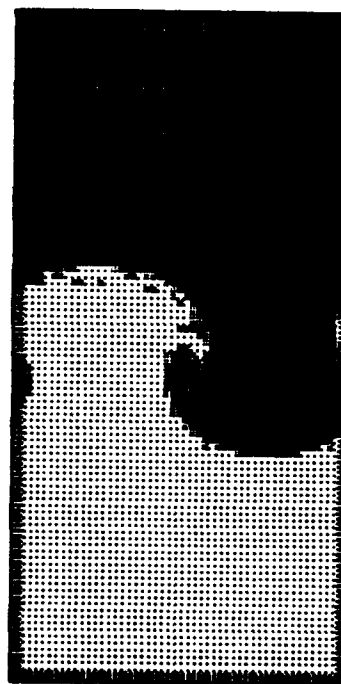
$t = 12.0$



$t = 12.0$

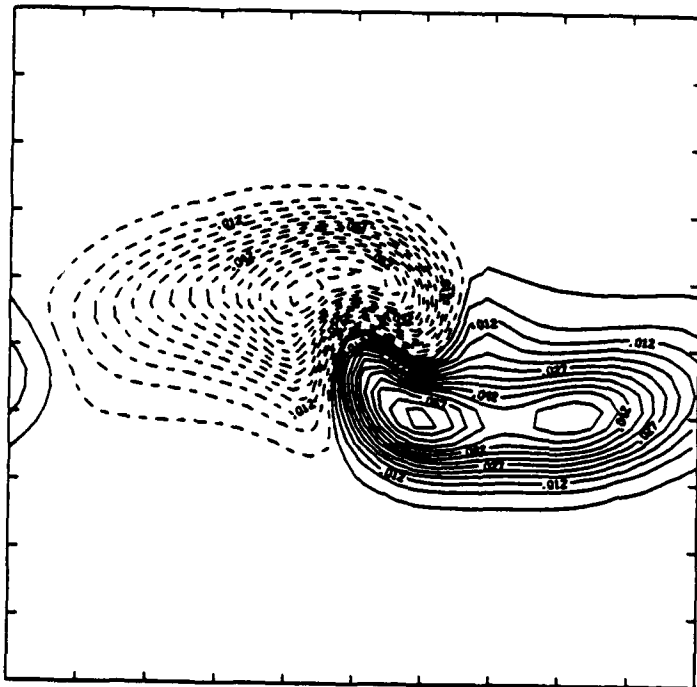


$t = 16.0$

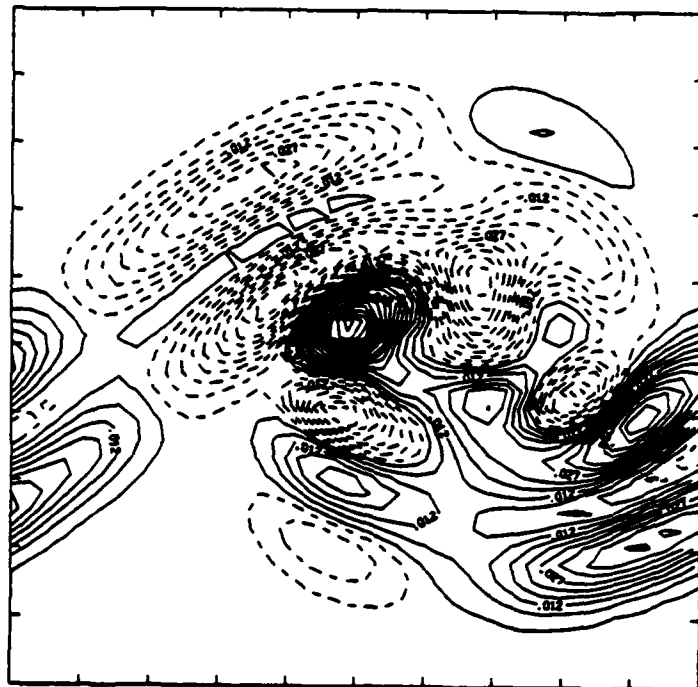


$t = 16.0$

Figure 18

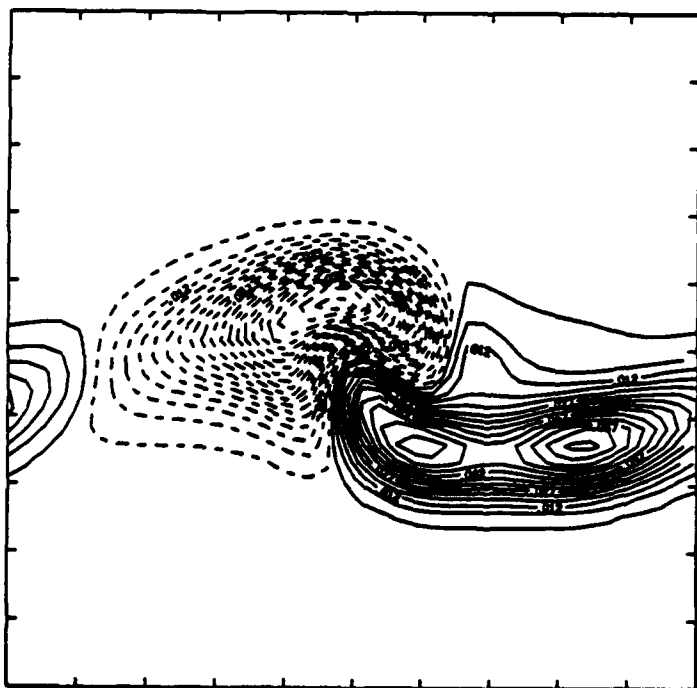


$t = 8.0$

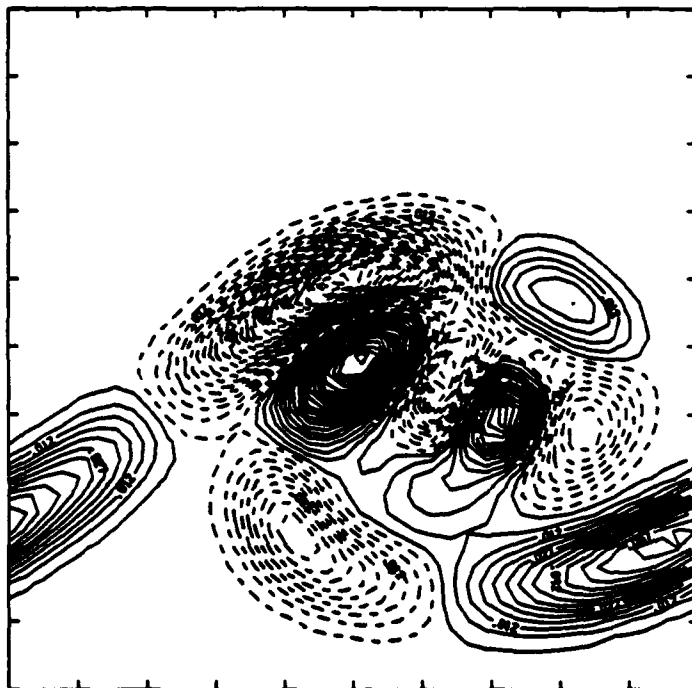


$t = 16.0$

(a)



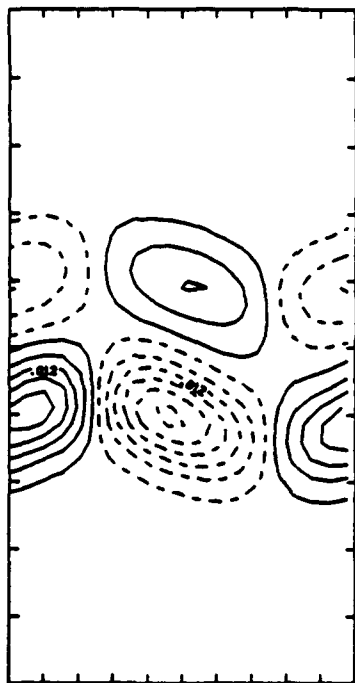
$t = 8.0$



$t = 16.0$

(b)

Figure 19

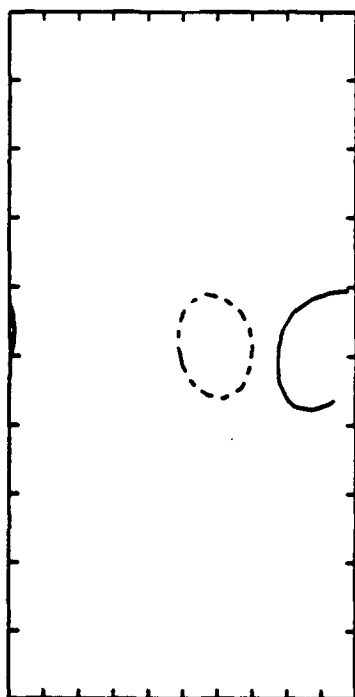


$t = 8.0$

(a)

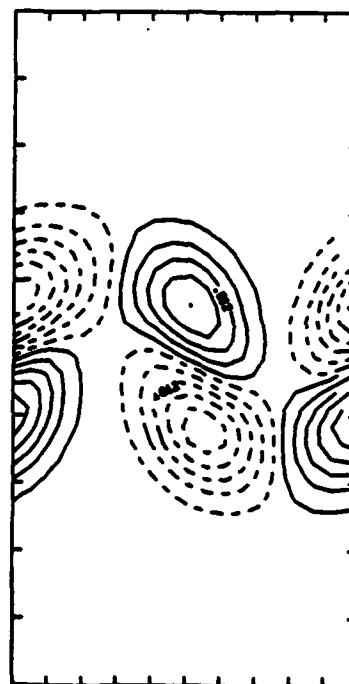


$t = 16.0$



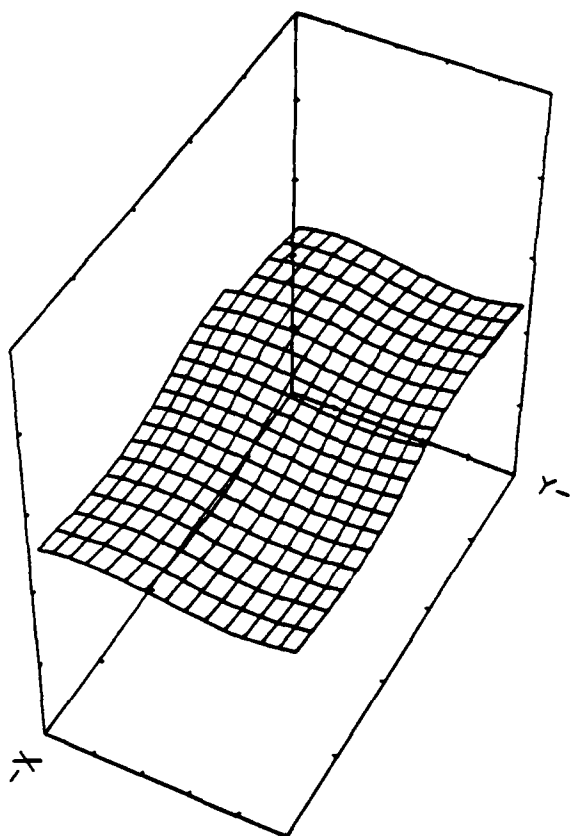
$t = 8.0$

(b)

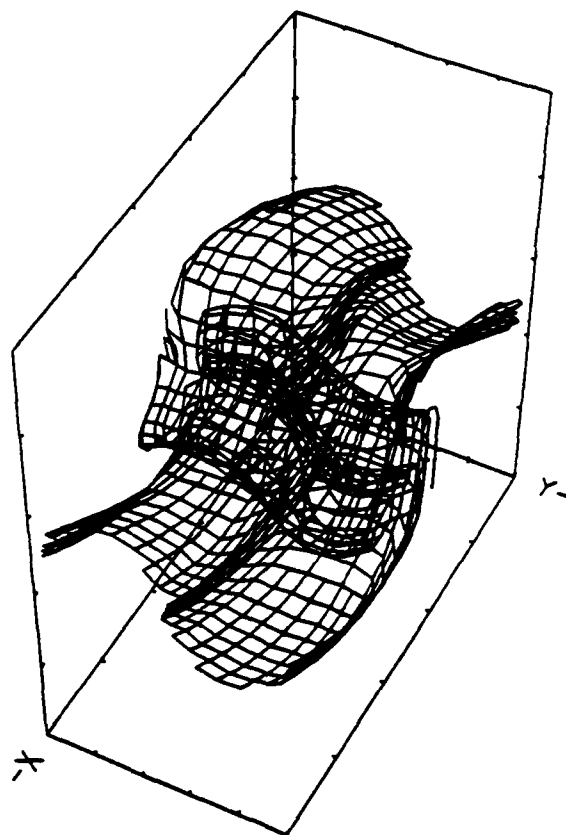


$t = 16.0$

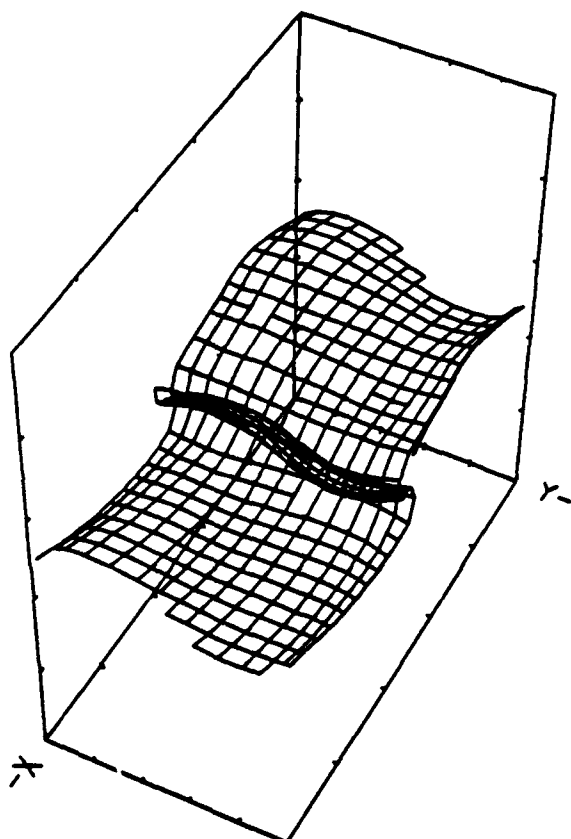
Figure 20



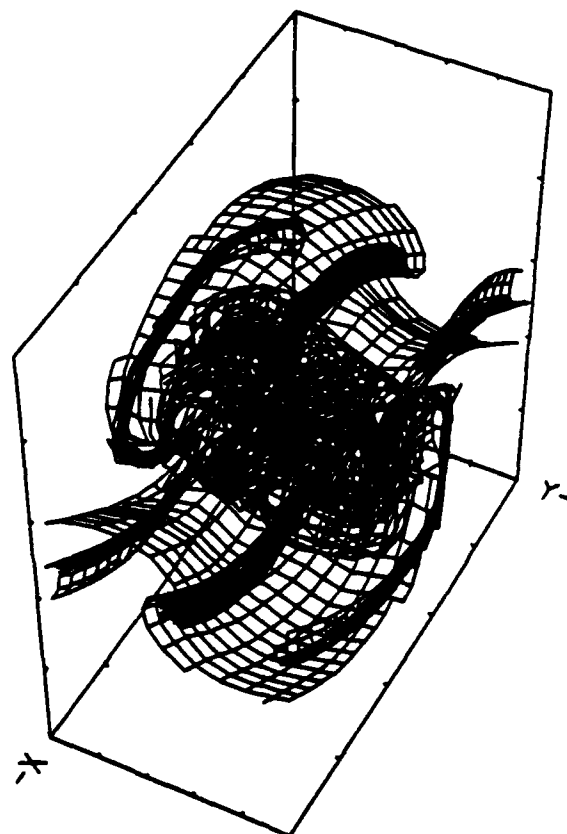
$t = 4.0$



$t = 12.0$

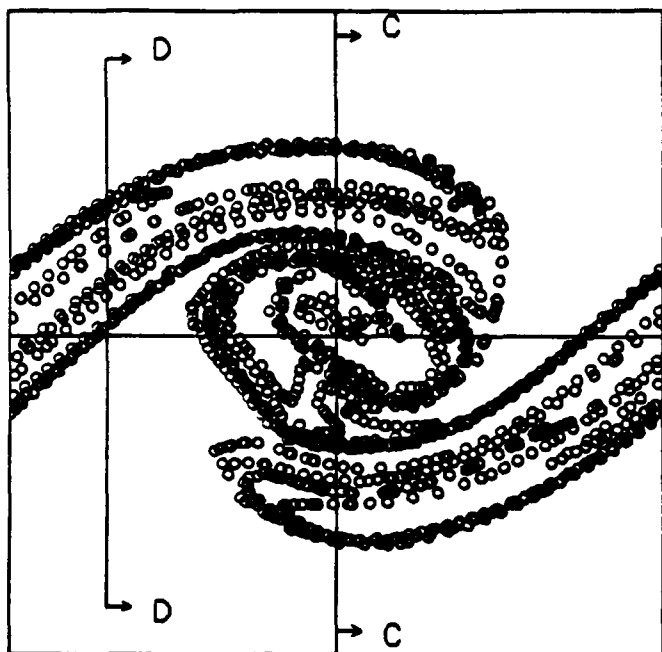


$t = 8.0$

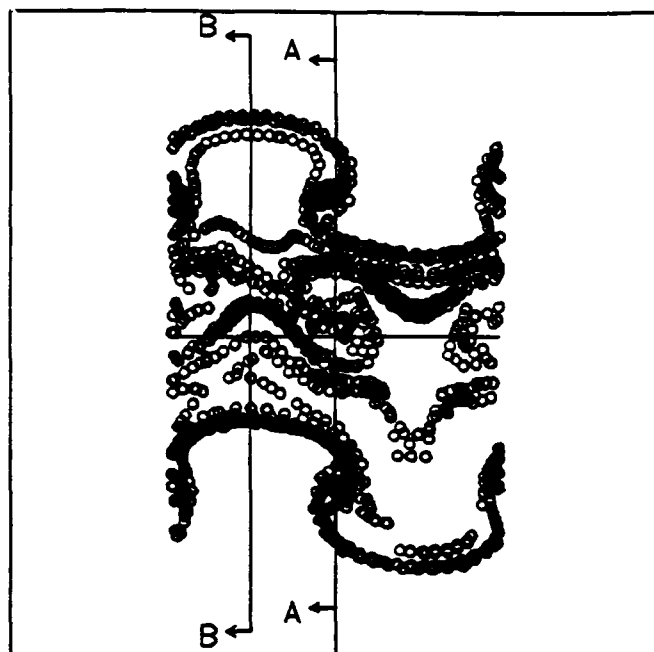


$t = 16.0$

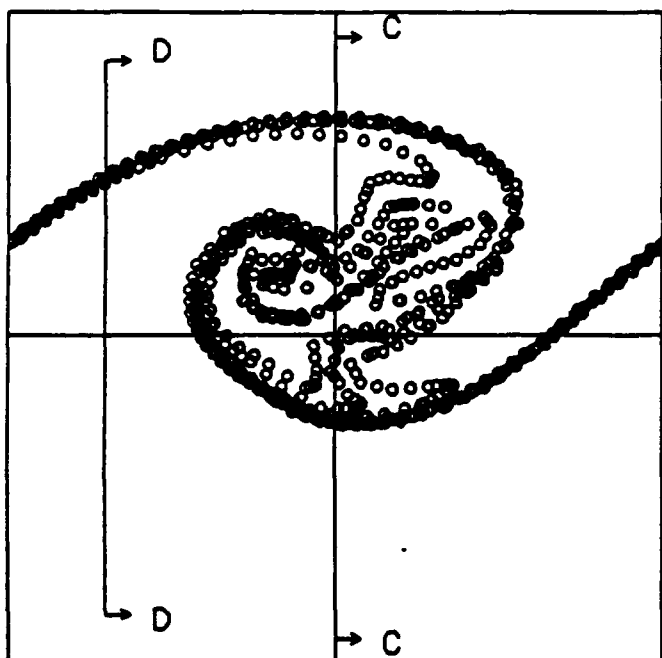
Figure 21



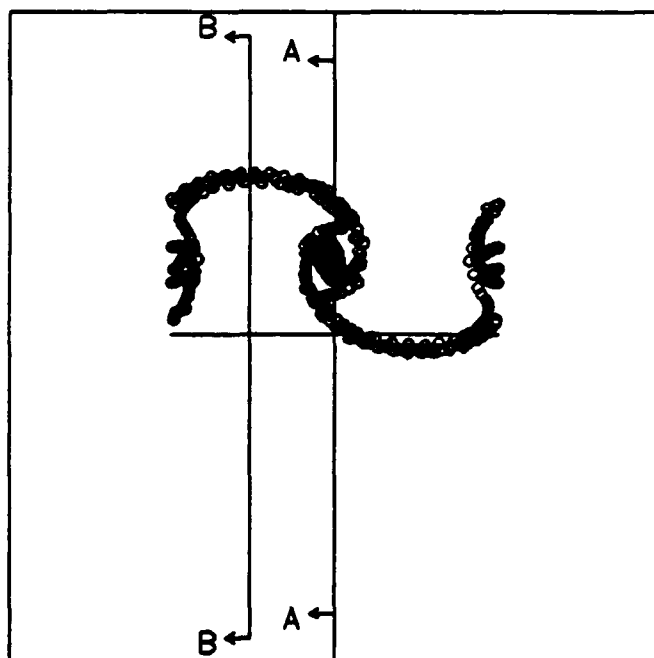
(a)  $y = 3.3$ , (AA).



(c)  $x = 6.6$ , (CC).

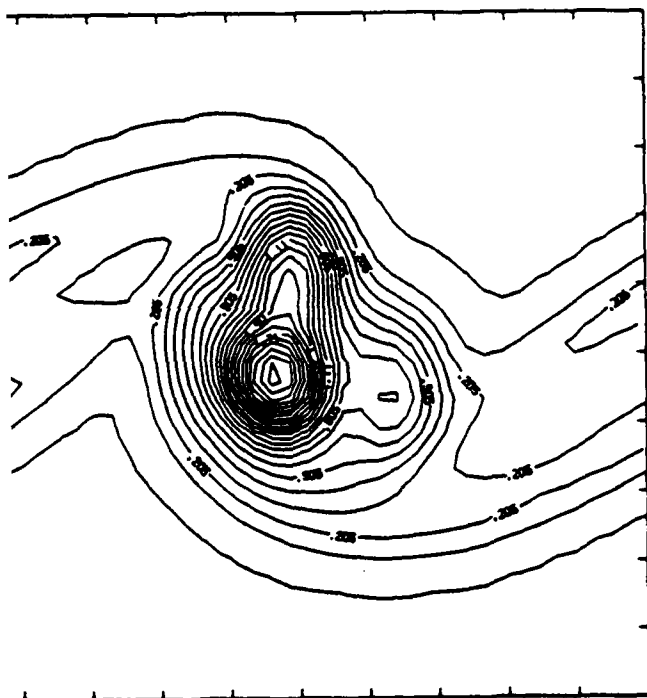


(b)  $y = 1.6$ , (BB).



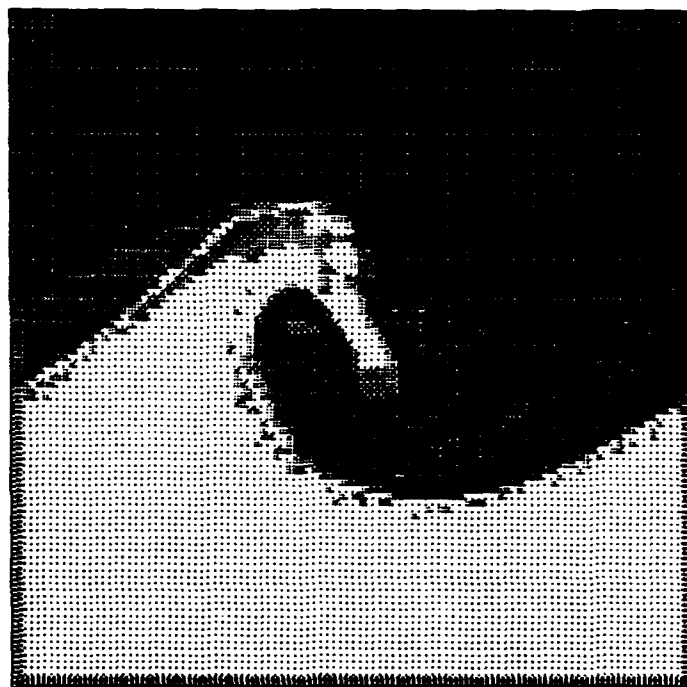
(d)  $x = 2.0$ , (DD).

Figure 22

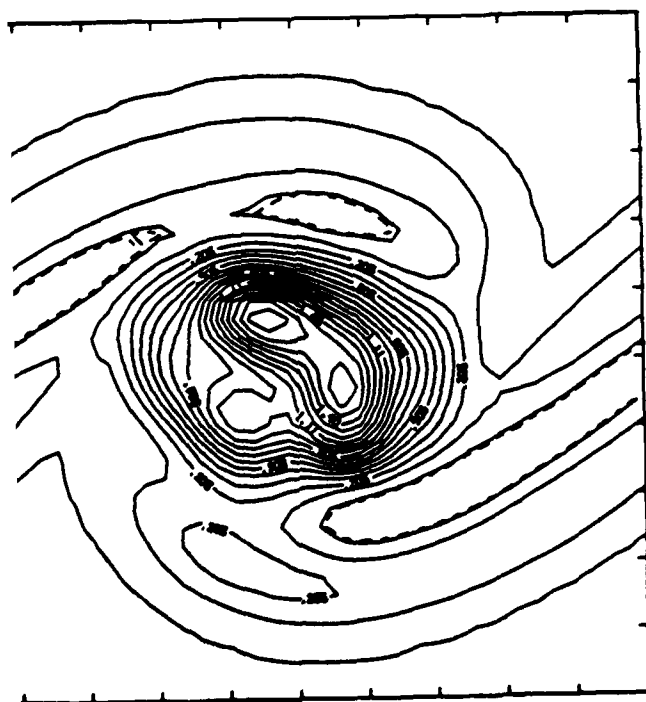


$t = 12.0$

(a)

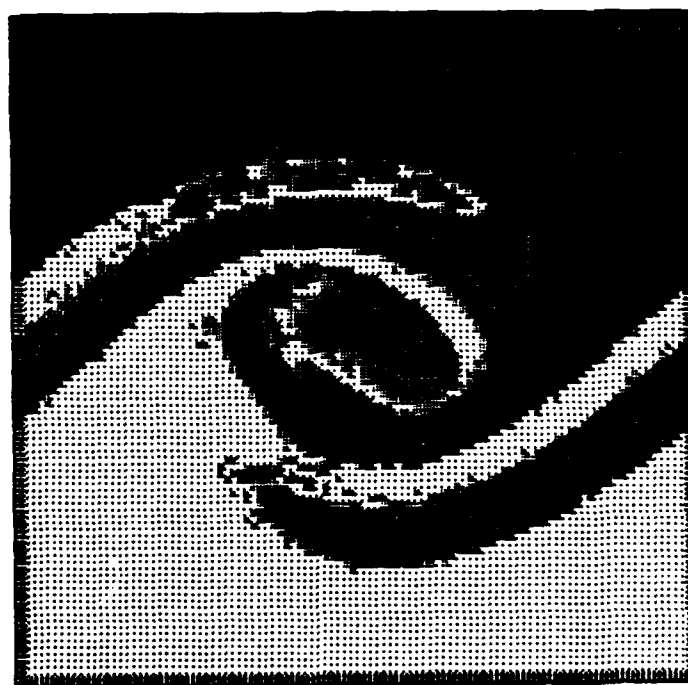


$t = 12.0$



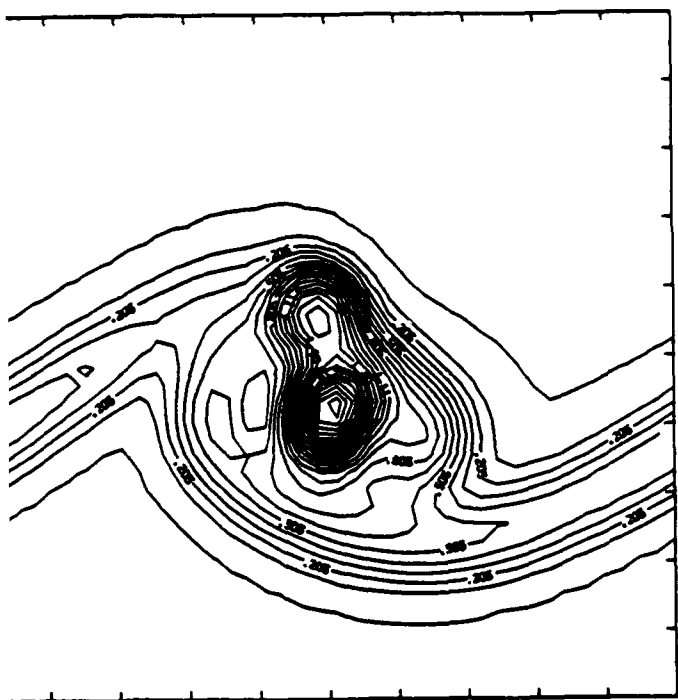
$t = 16.0$

(b)



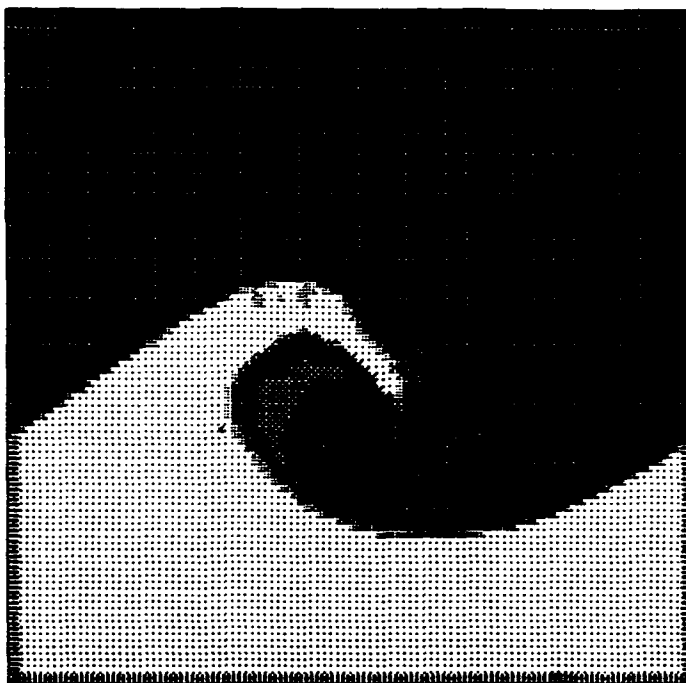
$t = 16.0$

Figure 23

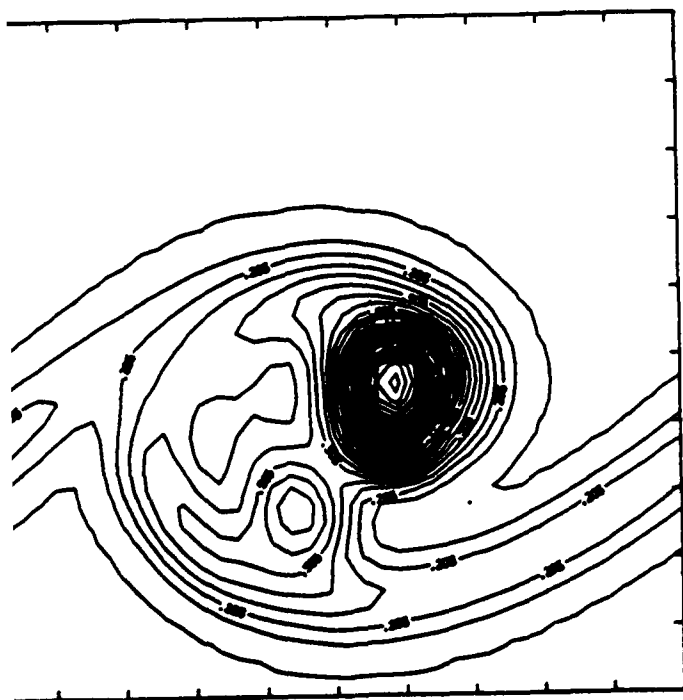


$t = 12.0$

(a)

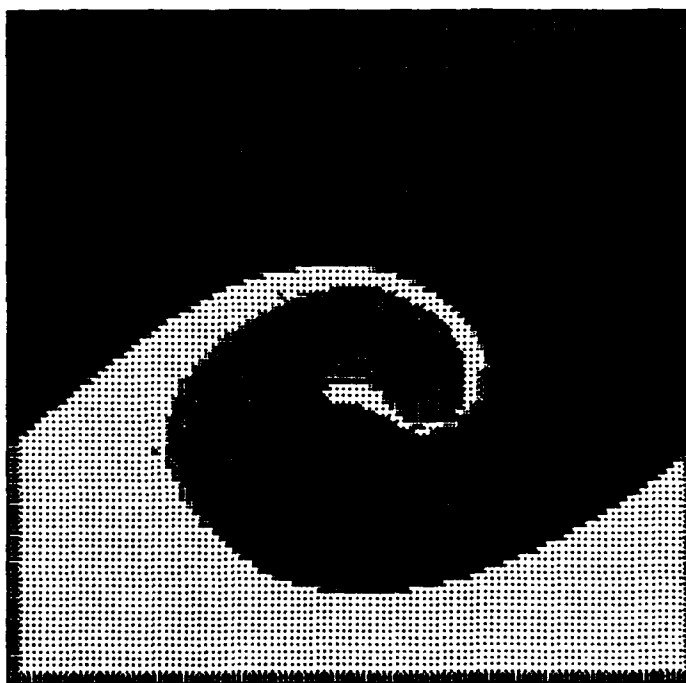


$t = 12.0$



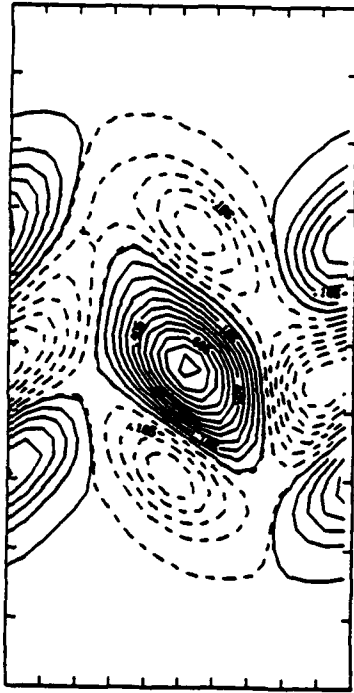
$t = 16.0$

(b)



$t = 16.0$

Figure 24



$t = 12.0$

(a)



$t = 12.0$



$t = 16.0$

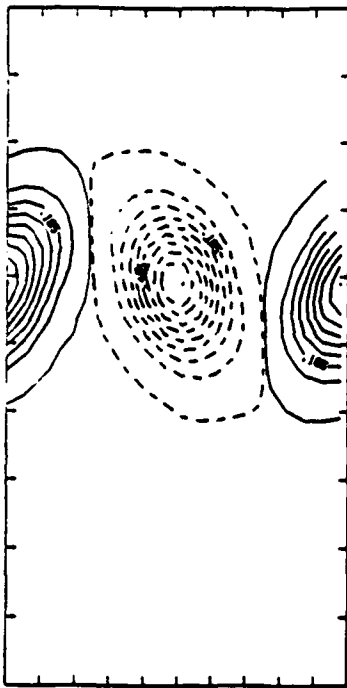
(b)



$t = 16.0$

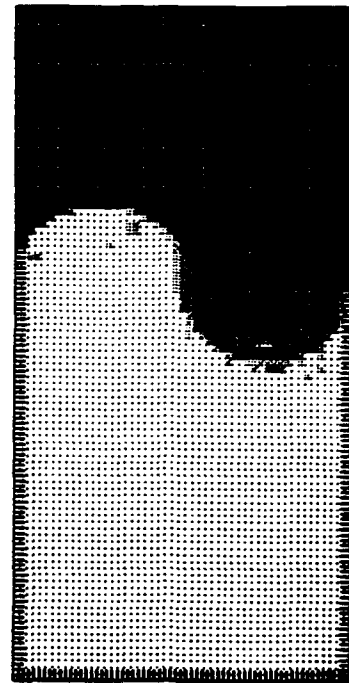
Figure 25



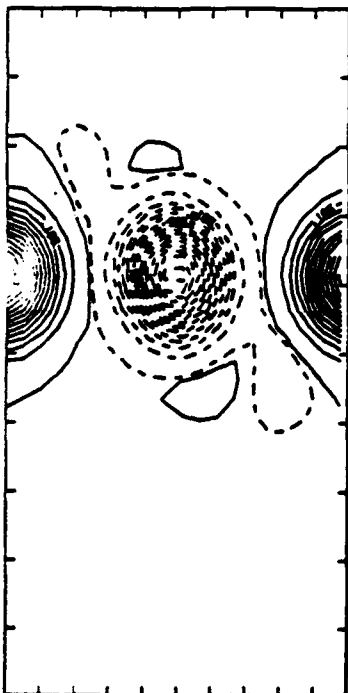


$t = 12.0$

(a)

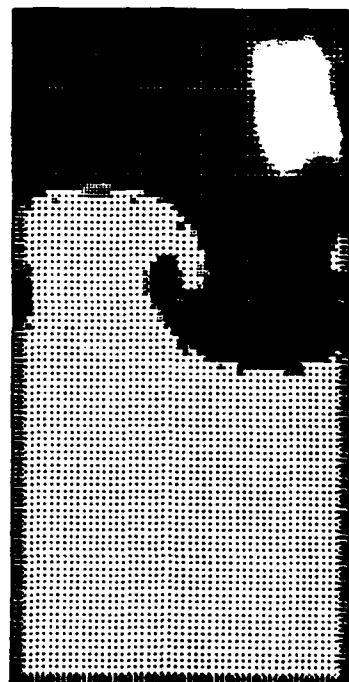


$t = 12.0$



$t = 16.0$

(b)



$t = 16.0$

Figure 26

## APPENDIX 11

Vortex Simulation of a Three-Dimensional Reacting  
Shear Layer With Infinite Rate Kinetics

Omar M. Knio<sup>\*</sup> and Ahmed F. Ghoniem<sup>¶</sup>

Department of Mechanical Engineering  
Massachusetts Institute of Technology

Cambridge, MA 02139

<sup>\*</sup> Post-Doctoral Associate, Member AIAA.

<sup>¶</sup> Associate Professor, Associate Fellow AIAA.

## ABSTRACT

The three-dimensional transport element method is extended to solve the conservation equations for reacting flow. The numerical scheme belongs to an adaptive, Lagrangian class of field methods in which computational effort is concentrated in zones of finite vorticity and chemical reaction. The method is based on accurate discretization of vorticity and species concentrations among a number of spherically-symmetric transport elements, and the advection of these elements along particle trajectories. We use the low Mach number approximation of combustion in open domains, and restrict our attention to the case of diffusion flames with no heat release. A single-step, second-order, infinite-rate kinetics chemical reaction model is employed.

The scheme is applied to study the effect of flow-induced instabilities on the reaction zone and product distribution in a temporal shear layer. Results are obtained in the high Peclet number regime for a wide range of Damkohler numbers. Changes in the reaction field are related to either the entrainment or the strain field associated with the saturation of the instabilities. With increasing Damkohler number, the structure of the reaction region changes from a distributed zone embedded within spanwise and streamwise vortices, to a thin sheet surrounding their cores. However, the product concentration always exhibits strong similarity to the vorticity distribution, realizing its highest values in zones of high vorticity and falling rapidly in regions where the vorticity magnitude is small. Variation of the Peclet number yields minor changes in the product distribution and in the reaction zone structure, but strongly affects product formation rates.

## I INTRODUCTION

The subject of this work is the construction of Lagrangian field methods for the numerical simulation of three-dimensional, high Reynolds number, reacting shear flow. In this fluid flow regime, vorticity is confined to a small well-defined fraction of the flow field making vortex methods, in which computational elements are used to cover the support of vorticity, a natural candidate for the solution of the momentum equation. In previous effort,<sup>1-3</sup> a modified vortex element scheme was constructed, and applied to study the motion of unconfined, inviscid vortex rings. The study revealed the need for (1) a careful representation of the vorticity field at the initial state, and (2) an accurate implementation of numerical schemes as time evolves. These requirements are especially critical in three-dimensional flows where several forms of rapidly-growing instabilities of complex shapes are present. To satisfy these requirements, and to accommodate the solution of scalar conservation equations, an adaptive class of Lagrangian field methods, called transport element methods, was constructed. Numerical study of several forms of these methods, which focused on the solution of the inviscid scalar transport equation, was successfully conducted in Refs. 4,5.

While the ultimate goal of this work consists of the construction of numerical methods for the solution of the compressible, turbulent combustion equations, in this study, we limit our attention to the low Mach number, isothermal flow limit. In the presence of an exothermic reaction, analysis of burning rates is complicated by the expansion field and the baroclinic vorticity generation spawned by the heat release, and the burning rates exhibit higher sensitivity to the strain field. In a three-dimensional flow, these mechanisms are further compounded by vorticity stretching and individual effects become hard to isolate. By virtue of our simplifying assumptions,

4

computed results will allow us to focus on studying the deformation of the diffusion flame by a known flow field.

The numerical scheme is obtained by modifying the transport element method discussed in Ref. 5. It is based on the discretization of both vorticity and species concentrations into a number of transport elements of finite, spherically-symmetric overlapping cores. Transport elements are distributed over entire material surfaces whose motion is tracked in a Lagrangian frame of reference. Vorticity associated with the elements changes by stretching and tilting, while species concentrations are updated by numerically accounting for diffusion-reaction terms. The rotational velocity field is computed by a discrete, desingularized Biot-Savart convolution over the field of the elements. Boundary conditions are satisfied by adding the contribution of the appropriate image system of the transport elements.

The method is applied to study the evolution of chemically-reacting temporal shear layers. The flow field is selected because of (1) its practical importance in a large class of combustion problems, and (2) the existence of experimental<sup>6-10</sup> and analytical<sup>11-12</sup> results which focus on the three-dimensional behavior of the flow. However, numerical studies of scalar entrainment, mixing and chemical reaction in three-dimensional layers remain scarce.<sup>13-16</sup> Thus, the method is used to study the effect of vorticity-induced entrainment and strain on the evolution of diffusion flames. Computed results are obtained for a wide range of Damkohler numbers, in order to study its effect on the structure of the reaction zone and product distribution.

## II FORMULATION AND NUMERICAL SCHEME

### II.1 FORMULATION AND GOVERNING EQUATIONS

We consider a three-dimensional, chemically-reacting flow in the limits of infinite Reynolds number, vanishingly small Mach number and heat release. The reaction is described by a single-step, second-order, infinite-rate kinetics,  $F$  (fuel) +  $O$  (oxidizer)  $\rightarrow$   $P$  (products). The reactants and products are assumed to behave as perfect gases with equal molecular weights, equal and constant physical properties. Under these assumptions, the vorticity form of the momentum equation, the continuity, and species conservation equations, normalized with respect to the appropriate combination of velocity,  $U_0$ , length,  $L_0$ , and density,  $\rho_0$ , scales, reduce to:

$$\frac{D\omega}{Dt} = \omega \cdot \nabla u \quad (1)$$

$$\nabla \cdot u = 0 \quad (2)$$

$$\frac{Ds^i}{Dt} = \frac{1}{Pe \, Le} \nabla^2 s^i - W \quad (3)$$

In Eqs. (1)-(3),  $u = (u, v, w)$  denotes the velocity vector in a right-handed Cartesian system  $x = (x, y, z)$ ,  $\omega = \nabla \times u$  is vorticity,  $t$  is time,  $D/Dt = \partial/\partial t + u \cdot \nabla$  is the material derivative,  $\nabla = (\partial/\partial x, \partial/\partial y, \partial/\partial z)$  is the gradient operator,  $\nabla^2$  is the Laplace operator,  $Pe = U_0/(\alpha L_0)$  is the Peclet number,  $Le = \alpha/\beta$  is the Lewis number, while  $\alpha$  and  $\beta$  denote, respectively, the thermal and mass diffusivities. The model requires the transport of two scalars,  $s^i$   $i=1,2$ , where  $s^1 = c_O$  denotes the oxidizer concentration, while  $s^2 = c_F$  represents the fuel concentration. The product distribution is given by  $c_P = 1 - c_O - c_F$ , and chemical production term  $W = Da \, c_O \, c_F$  where  $Da$  is the Damkohler number. Equations (1)-(3) are obtained by simplifying the low Mach number equations for combustion for vanishingly small heat release. The assumption of no heat release implies that both temperature and density remain constant, so that both baroclinic vorticity generation and volumetric expansion effects cancel in the vorticity transport equation. The model ignores viscous effects, since

viscosity only affects the motion of the vorticity field well beyond the mixing transition, a mechanism which is not in the scope of the present computations. Mass diffusion effects are retained, because they govern the mixing and chemical reaction processes.<sup>17</sup>

## II.2 NUMERICAL SCHEME

The numerical scheme used in the solution of the governing equations is obtained by extension of the methods analyzed in previous work,<sup>5</sup> and hence is summarized in the following. Its construction starts with the discretization of the vorticity field,  $\omega(\mathbf{x})$ , on a three-dimensional mesh:

$$\omega(\mathbf{x}, 0) = \sum_{i=1}^N \omega_i(0) dV_i f_{\delta}(\mathbf{x} - \mathbf{X}_i) \quad (4)$$

where  $N$  is the total number of vortex elements,  $\mathbf{X}_i$ ,  $dV_i$ , and  $\omega_i$  denote the center, volume, and vorticity of element  $i$ , respectively. The vorticity associated with each element is smoothed in a small neighborhood of  $\mathbf{X}_i$  according to a spherical core function,  $f_{\delta}$ , with core radius,  $\delta$ , where  $f_{\delta}(r) = (1/\delta^3) f(r/\delta)$ . A third-order Gaussian core function,

$$f(r) = \frac{3}{4\pi} e^{-r^3} \quad (5)$$

is adopted.<sup>18-19</sup> Note that  $f$  decays rapidly for  $r > \delta$  so that  $\delta$  represents the radius of the sphere where vorticity is concentrated.

The vortex elements are initialized by employing entire material surfaces distributed within the support of vorticity. The surfaces are discretized into rectangular "transport" elements which generalize the notion of the vortex vector elements. In this representation, a transport element is specified by the vector  $(X_1^1, X_1^2, X_1^3, X_1^4)$ , where the Lagrangian coordinates  $X_1^1$ ,  $X_1^2$ ,  $X_1^3$  and  $X_1^4$  are used to define a "rectangular" area around its center. The transport elements are selected such that the sides of adjacent rectangles



coincide to form a mesh which continuously describes an entire material surface. This construction resembles, but differs from that proposed by Agishtein & Migdal who used triangular elements to describe a singular vortex sheet.<sup>20</sup>

Within each element, we use a finite element description of the surface using linear interpolation functions.<sup>21</sup> The motion of the centers of the elements,  $x_i$ , is approximated by:

$$x_i(t) = \frac{1}{4} (x_i^1(t) + x_i^2(t) + x_i^3(t) + x_i^4(t)) \quad (6)$$

where the  $x_i^j(t)$ ,  $j = 1, 2, 3, 4$ , denote the instantaneous coordinate of the material particles whose Lagrangian coordinates coincide with the vertices of the initial mesh. This representation accommodates the integration of the vorticity transport equation, which is necessary in general flow situations,<sup>5</sup> but retains the advantages of vortex element schemes which relate the evolution of the vorticity field to the deformation of vortex lines.<sup>22-26</sup> Under the assumptions made above, the latter approach is preferred, since it results in considerable computational savings as direct evaluation of the gradient of the flow map is avoided. This is done by associating with each element a circulation  $\Gamma_i$  and requiring that the pair of opposing sides of the rectangles,  $(x^3, x^1)$  and  $(x^4, x^2)$ , align with the local vorticity vector. The quantity  $\omega_i(t) dV_i$  is thus replaced by  $\Gamma_i \delta x_i(t)$ , where the evolution of the material length  $\delta x_i(t)$  is given by:

$$\delta x_i(t) = \frac{1}{2} (x_i^3(t) + x_i^4(t) - x_i^1(t) - x_i^2(t)) \quad (7)$$

According to Kelvin's theorem,  $\Gamma_i$  remains constant along a particle path, while Helmholtz' theorem is used to relate the evolution of  $\omega_i(t)$  to that of  $\delta x_i(t)$  as follows:

$$\omega_i(t) = \frac{|\omega_i(0)|}{|\delta x_i|} \delta x_i(t) \quad (8)$$

The velocity field, induced by the vorticity distribution in an infinite domain, is given by the discrete, desingularized Biot-Savart law:

$$u_{\omega} = -\frac{1}{4\pi} \sum_{i=1}^N \Gamma_i \frac{(\mathbf{x}-\mathbf{x}_i) \times \delta \mathbf{x}_i}{|\mathbf{x}-\mathbf{x}_i|^3} \kappa\left(\frac{r_i}{\delta}\right) \quad (9)$$

where  $\kappa(r) = 4\pi \int_0^r f(r') r'^2 dr' = 1 - \exp(-r^3)$ , and  $r_i = |\mathbf{x}-\mathbf{x}_i|$ . The velocity field thus obtained is used in conjunction with a second-order predictor-corrector scheme to update the particle positions  $\mathbf{x}_i^j(t)$ .

Analysis of particle methods,<sup>22-26</sup> and numerical evidence<sup>5</sup> indicate that severe deformation of the Lagrangian mesh under the action of the strain field causes a deterioration in the discretization accuracy. To overcome this difficulty, the remeshing algorithm suggested in Ref. 5 is utilized. It effectively amounts to the redistribution of the elements along a vortex tube and the splitting of the vortex tubes along material surfaces, whenever the length of the elements exceeds the core radius. This allows us to capture severe distortions of the flow without losing accuracy.

The numerical solution of Eq. (3) is performed in a similar way as that of the vorticity field. The concentration fields are discretized among the transport elements, which now carry, along with vorticity, discrete local values of  $s^1$  and  $s^2$ . We let:

$$s(\mathbf{x}, t) = \sum_{i=1}^N s_i(t) dV_i f_{\delta}(\mathbf{x}-\mathbf{x}_i(t)) \quad (10)$$

Next, we adopt the discrete approximation of the Laplacian operator:

$$\nabla^2 s_j - B(s_j) = \frac{2}{\delta^2} \sum_{k=1}^N (s_k - s_j) dV_k g_{\delta}(\mathbf{x}_k(t) - \mathbf{x}_j(t)) \quad (11)$$

where

$$g(r) = -\frac{1}{r} \frac{df}{dr}, \quad g_{\delta}(\mathbf{x}) = \frac{1}{\delta^3} g\left(\frac{|\mathbf{x}|}{\delta}\right) \quad (12),$$

and  $f$  is the core smoothing function previously defined.<sup>27-31</sup> This scheme is preferred over random walk methods,<sup>32</sup> whose implementation is cumbersome in conjunction with the transport of connected surfaces, and over core spreading techniques,<sup>33</sup> which no longer yield simple evolution equations for the core radii. The evolution of the scalar concentration fields is found by numerically integrating:

$$\frac{ds_j^i}{dt} = \frac{1}{Pe \ Le} B(s_j^i) + W \quad (13)$$

using the same method employed in tracking the particle positions.

### III FLOW GEOMETRY AND INITIAL CONDITIONS

We assume a vorticity layer of finite thickness, periodic in its streamwise  $x$ -direction and spanwise  $y$ -direction, and unconfined in the cross-stream  $z$ -direction. The thickness of the layer is expressed by  $2\sigma$  where  $\sigma$  is the standard deviation of the second-order Gaussian curve which describes the physical vorticity distribution within the layer at  $t = 0$ . Letting  $\Omega(x)$  denote this initial condition, we have:  $\Omega_y(x) = 2/(\sigma \sqrt{\pi}) \exp(-z^2/\sigma^2)$ ,  $\Omega_x(x) = \Omega_z(x) = 0$ . The corresponding velocity distribution  $U(x)$  at  $t = 0$  is given by:  $V(x) = W(x) = 0$ , and  $U(x) = \text{erf}(z/\sigma)$ ,  $\text{erf}$  being the error function. The vorticity layer thus admits a streamwise velocity difference  $\Delta U = 2$ . The periodicity length in the  $x$ -direction,  $\lambda_x = 13.2 \sigma$ , corresponds to the wavelength of the two-dimensional most unstable mode,<sup>11</sup> while  $\lambda_y = \lambda_x/2$  is selected close to the wavelength of the most amplified three-dimensional mode.<sup>12</sup> The initial fuel and oxidizer concentrations follow error-function type profiles,  $c_o(t=0) = \text{erf}(z/\sigma)$ ,  $c_f(t=0) = 1 - \text{erf}(z/\sigma)$ , so that  $c_p(t=0) = 0$ . Thus, the top stream and bottom streams consist respectively of oxidizer and fuel, and the initial

thickness of the vorticity layer matches the "mixed" zone, or the zone of finite chemical activity.

The layer is initially discretized among elements distributed on a grid of  $20 \times 14 \times 5$  points along the  $x$ -,  $y$ -, and  $z$ -directions respectively. Furthermore,  $\sigma$  is chosen as a reference length scale so that  $\Delta x = \Delta z = 0.66$ , and  $\Delta y = 0.471$ . The top stream velocity,  $U(z \rightarrow \infty)$ , is selected as a reference velocity scale, the time step  $\Delta t = 0.1$ , and  $\delta = 0.89$ . The circulations of the elements are found by matching discretized and assumed vorticity values at the centers of the elements, while the concentration fields,  $s_i^1$  and  $s_i^2$ , are initialized by associating with the transport elements, the values realized by the corresponding "physical" distribution at their centers. Normal, periodic boundary conditions are satisfied by adding the contribution of the image system of the transport elements, using the procedure detailed in Ref. 5.

The layer is perturbed at  $t = 0$  using two sinewaves of the same amplitude in the streamwise and spanwise directions, as expressed by the transformation  $z_i \rightarrow z_i + \epsilon \sin(2\pi x_i / \lambda_x) + \epsilon \sin(2\pi y_i / \lambda_y)$ ,  $\epsilon = 0.02 \lambda$ . Computations of the non-reacting flow field are carried until  $t = 18.0$  to observe the growth of two and three-dimensional instabilities, while those of the reacting flow field are stopped at  $t = 16.0$ , i.e. when mature vortical structures are formed. Results are obtained for a total of 21 cases, assuming infinite Reynolds number, unit Lewis number and varying the Damkohler and Peclet numbers. We consider seven values of the Damkohler number,  $Da = 0.1, 0.2, 0.4, 1., 2.5, 5.0$ , and  $10.0$ , and three values of the Peclet number,  $Pe = 250, 500$ , and  $1000$ . In the following, we start with a summary of the evolution of the flow and vorticity fields, and then discuss the influence of the vortical structures on the shape of the reaction zone and the product concentration distribution.

#### IV FLOW FIELD EVOLUTION

The development of the shear layer, as represented by the evolution of the material surfaces where the vorticity is non-zero (the flow is inviscid), and the vorticity field on different spanwise and streamwise locations are examined. Similar flow configurations were analyzed by the present authors in Ref. 5, studied by Ashurst and Meiburg who focused on the dynamics of vortex filaments in both symmetric and asymmetric layers,<sup>34</sup> and by Metcalfe et al. who used a spectral scheme to examine the evolution of individual instability modes.<sup>35</sup> Hence, the main features of the flow are briefly discussed in the following.

Figure 1 depicts three-dimensional perspective views of the material surface initially located at  $z = 0$ , at  $t = 12.0$  and  $16.0$ . This represents the middle surface within the shear layer where most of the vorticity is concentrated. The plots are generated from the point of view of an observer located at  $(48, 24, 48)$ .

At  $t = 12.0$ , the rollup of the vorticity layer produces a well-defined spanwise eddy core. The saturation of the instability is associated with the redistribution of the vorticity field and results in the creation of a core where most of the spanwise vorticity is concentrated, and braids which are constantly strained under the influence of the spanwise vortex cores. The amplitude of the spanwise perturbation is significantly amplified along the core, an indication of the evolution of the transverse instability.<sup>12</sup> This non-uniform axial displacement of the core is accompanied by an out-of phase deformation of the braids region under the influence of the generated streamwise vorticity.

At  $t = 16.0$ , the motion becomes highly three-dimensional as differences along various spanwise stations become important and depart from the shape of the imposed sinewave perturbation. The stretching of the braids, which are

"anchored" along the boundaries of the domain and pulled towards the core, leads to the generation and intensification of streamwise vorticity. This results in the saturation of the streamwise vorticity into vortex rods which extend throughout the braids and are wrapped around the spanwise core. The presence of streamwise vortex rods is inferred from the spinning of material surfaces about streamwise axes which are located at the spanwise mid-section and boundaries of the domain.

The Lagrangian description of the flow is completed by considering two-dimensional cross-sections of the computational surfaces. Figure 2 shows cross-sections through all the material surfaces at  $t = 18.0$ . We consider spanwise sections along two-dimensional planes specified by (a)  $y = 3.3$ ; and (b)  $y = 1.6$ , and streamwise sections through the core and braid regions, in the planes located at (c)  $x = 6.6$ ; and (d)  $x = 2.0$ . Circles are drawn to mark the intersection points with the transport elements. The radius of the circles is smaller than the core radii of the smoothing functions.

The spanwise cross-sections illustrate the effect of the translative instability which causes a non-uniform axial deformation of the spanwise vorticity core. The eddy core eddy is pushed upwards and in the direction of the top stream in the "left" half of the domain,  $0 < y < 3.3$ , while it suffers an antisymmetric deformation in the other half. The core region at most spanwise cross-sections loses its symmetry, as computational elements migrate in the direction opposite to that of the core translation. The intersection of material surfaces with the plane  $y = 3.3$ , shows that the braids thicken significantly at this spanwise location and that they entrain irrotational fluid from both free streams. This can be verified by simultaneously examining Fig. 2c which shows the wrapping of the mushrooms around the core of the eddy. The entrainment of mushrooms, which are generated in the braids, towards the core region leads to the formation of a double structure. Dark

areas which appear along the core region correspond to the intersection of the streamwise vortex rods with the plane of the figure.

Figures 3-6 show constant spanwise vorticity contours, plotted in two spanwise sections,  $y = 3.3$  and  $1.6$ , and streamwise vorticity contours in the streamwise sections  $x = 6.6$  and  $2.0$ , respectively. Contours are generated at times  $t = 12.0$  and  $16.0$ . At earlier times, the vorticity field exhibits small deviations from that obtained in a two-dimensional flow, and hence is not depicted. The growth of three-dimensional perturbations is suppressed during the initial stages of the Kelvin-Helmholtz instability and the spanwise vorticity remains essentially uniform across the layer.<sup>5,34,35</sup> Weak streamwise structures are generated by local tilting of the vortex lines into the streamwise direction, but do not significantly affect the evolution of the flow. This mechanism leads to the creation of zones of alternating streamwise vorticity whose locations and signs follow the shape of sinewave perturbation.

Following the rollup of the spanwise vorticity the flow field undergoes a rapid transition to three-dimensional motion. In the braids region, a violent increase in the amount of streamwise vorticity is observed. The streamwise structure almost doubles in strength in half the time span it took to generate it. This behavior is expected since the creation of the large spanwise eddy results in larger strain rates in the neighborhood of the stagnation "lines" which anchor the braids.

In the meantime, the streamwise vorticity distribution along the core becomes distinguished by the presence of a top and a bottom row of counter-rotating streamwise vortices. These rows are separated by a third, middle row, which is generated as a result of the growth of perturbations along the core itself by the mechanism of the translative instability, and is  $180^\circ$  out of phase with the other two.<sup>34</sup> The growth of perturbations along the core leads to a more dramatic increase of the streamwise vorticity, as the middle

row of vortices becomes stronger than the top and bottom rows. The generation of strong streamwise structures in the core region is not associated with large amplitude deformation in the streamwise direction. This may be explained by noting that the rollup of the layer, which precedes the three-dimensional motion, forces the migration of the spanwise vorticity from the thinning braids into the core region. Also note that the intensification of the streamwise vortices, entrained from the braids into the cores (the top and bottom rows), lags that observed in the braids. Thus, streamwise vorticity associated with the vortex rods is generated in the braids and then strained towards the cores.

The transition to three-dimensional motion, in its initial stage, does not lead to significant qualitative modification of the structure of the layer as perceived in two-dimensional spanwise cuts. The spanwise vorticity distribution still bears a striking resemblance to that observed in a two-dimensional flow. However, we note two minor differences: (i) the vortex core, while essentially governed by the dynamics of the primary instability, suffers a reduction of its cross-section; and (ii) the vorticity distribution loses its symmetry in the plane located at  $y = 1.6$ , but remains symmetric at the spanwise midsection of the domain,  $y = 3.3$ . The first effect is a consequence of the growth of the three-dimensional perturbation on the spanwise core which necessitates a stretch component along its axis. The loss of symmetry, which becomes more obvious in the later stages of development of the three-dimensional instability, is discussed below.

The non-linear stages of evolution of the three-dimensional instability are examined first in the streamwise planes of the shear layer, Figs. 5 and 6. The stretching of the vorticity lines along the braids leads to the maturation of the elongated vortices into round concentrated cores.<sup>36-37</sup> The flow field induced by the vortex rods causes further deformation of the material surfaces



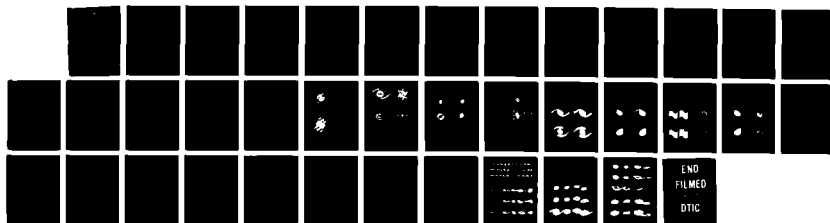
AD-A239 745

VORTEX SIMULATION OF TURBULENT COMBUSTION(U)  
MASSACHUSETTS INST OF TECH CAMBRIDGE A F GHONIM  
19 NOV 92 AFOSR-TR-92-1018 AFOSR-89-0491

2/2

UNCLASSIFIED

NL



resembles, but is different from, the two-dimensional pairing of vortices. This type of distribution should be contrasted with that obtained in unstable vortex rings which displays similar features at certain azimuthal cross-sections.<sup>2</sup>

## V REACTING SHEAR LAYER

We turn our attention to the study of diffusion flames in three-dimensional vorticity layers. Since heat release effects are neglected, temperature and density remain constant, and the reaction does not affect the flow field. Results are used to analyze the effect of vorticity-induced entrainment and strain on the reaction zone, product distribution, and burning rates. We start with a reacting layer at low Damkohler number and low diffusion,  $Da = 0.1$  and  $Pe = 1000$ , then at high Damkohler number and low diffusion,  $Da = 10$  and  $Pe = 1000$ .

Results are shown in terms of shaded contours of product concentration, and product formation rate,  $W$ . Product concentration is shown in terms of six different shades of gray, mapped to equal size intervals between 0 and 1. The product formation rates are first normalized by the maximum value achieved in the plane where the figure is generated, before the contours are drawn. In these plots, dark areas highlight the zone of highest chemical activity, and must not be used as indication of the actual formation rates.

### V.1 REACTING LAYER AT LOW DAMKOLER NUMBER

Figures 7-10 show product concentration and reaction rate contours in the planes  $y = 3.3$ ,  $y = 1.6$ ,  $x = 6.6$ , and  $x = 2.0$ , respectively, generated at  $t = 12.0$  and  $16.0$ . In each figure, product concentration and reaction rate contours are shown side-by-side. At earlier stages,  $t \leq 8.0$ , examination of

the reaction field (not shown here) exhibits small differences from those one obtains in a two-dimensional field.<sup>39-40</sup> The products of reaction and the zone of highest chemical activity surround the region of highest vorticity. Three-dimensional effects are weak in this stage, and can only be detected along the streamwise sections, which show very small spanwise undulations of the layer.

With the intensification of the streamwise vortices in the braids and the amplification of the translative instability in the cores, significant deviations from two-dimensional behavior are observed. At  $y = 3.3$ , the streamwise vortex rods which start to form at the boundaries of the domain enlarge the product concentration layer at this location. As shown in Fig. 7b, enlargement of the layer is a consequence of burning enhancement, associated with the rollup of the surfaces around the streamwise vortices. This is contrary to the result of two-dimensional simulations in which the strain field of the spanwise vortex cores leads to continuous thinning of the product layer embedded within (or surrounding) the braids.<sup>40</sup>

However, the thinning of the braids and the entrainment of products towards the spanwise vortex core are still observed in the spanwise section  $y = 1.6$ , which does not intersect any streamwise vortex rod. Meanwhile, the products of reaction undergo a displacement similar to that of the vorticity core (Fig. 8a). The translation of the core towards the top stream and the migration of its geometric center in the opposite direction destroy the symmetry of the product concentration. The asymmetric mixing patterns associated with this mechanism also affect the reaction rate distribution (Fig. 8b), since the reaction rate, which depends strongly on the composition of the reacting mixture, drops rapidly if either oxidizer or fuel become deficient. This description persists survives the restructuring of the vorticity core by the maturation of three-dimensional instabilities, so that

the reaction rate and product concentration distributions at this section are in qualitative agreement with the results of two-dimensional simulations.<sup>40</sup>

The difference between the two sections is directly related to the streamwise vorticity. The presence of streamwise vortex rods leads to mixing and combustion enhancement, a mechanism which resists the "negative" effects of the underlying two-dimensional strain field. Not only do the streamwise vortex rods lead to mixing enhancement via entrainment, but also maintain high product concentration near their axes (Fig. 7a).

In the streamwise sections, the product concentration changes from a wavy layer across the span, into a highly concentrated distribution embedded within the cores of the streamwise vortices. The streamwise vortex rods generate mushroom structures in the braids. With the intensification of the streamwise vorticity in concentrated cores, At late stages,  $t = 16.0$ , the field of the vortices causes severe thinning of the "braids" joining neighboring rods which almost become devoid of products. These transverse entrainment currents are best appreciated by simultaneously examining Figs. 10a and 10b, which indicate that the depletion of products occurs despite high reaction rates in regions separating the streamwise eddies. Thus, the strain and entrainment fields tend to reshape the structure of the product concentration such that high product concentration coincides with high concentration of vorticity, and falls rapidly as one moves into zones of small vorticity.

The effect of the translation of the spanwise core on the product and reaction rate distributions is inspected in Fig. 9. At early stages,  $t \leq 8.0$ , combustion occurs in an almost uniform layer across the span. Initial growth of the transverse instability causes a wavy deformation of the reaction zone and of the region of high product concentration. The distribution of the latter is complicated by the entrainment of the braids, which trap layers of unburnt fluid on the top and bottom sides of the deformed core. At later

stages, the maturation of the three-dimensional instabilities yields distributions of even higher complexity.

The entrainment of mushroom structures formed in the braids towards the cores remains easy to detect. Within these structures, zones of high product coincide with the axes of the corresponding vortex rods, while, as expected, reaction rates remain high across the span. The deformation associated with the maturation of the translative instability is harder to analyze, as the core of vorticity to cross the plane of the figure. The streamwise vortices induce a spinning motion which enhances the chemical reaction (Fig. 9b) so that their axes become zones of high product concentration. The motion induced by these vortices, visualized by the redistribution of the reaction zone, resembles the deformation which accompanies the formation of the vortex rods and can be predicted by the streamwise vorticity distribution shown in Fig. 5. Interpretation of the product and reaction distributions shown in Fig. 9 requires examination of several sections simultaneously. Such an exercise might be conducted by comparing the distributions of Figs. 9 and 8, with the motion of material particles shown in Figs. 2c and 2b. The comparison yields a clear illustration of the motion of the core of vorticity, and of the transverse diffusion fluxes associated with the growth of three-dimensional instabilities.

## V.2 REACTING LAYER AT HIGH DAMKOHLEK NUMBER

We now consider the evolution of the reaction field for a three-dimensional layer at high Damkohler and Peclet numbers,  $Da = 10$ , and  $Pe = 1000$ . As in the previous section, the analysis is conducted by plotting the product concentration and normalized reaction rate contours in the spanwise sections  $y = 3.3$  and  $1.6$  and the streamwise sections  $x = 6.6$  and  $x = 2.0$ , in

Figs. 11-14 respectively. In each figure, snapshots of the corresponding variables are shown at  $t = 12.0$  and  $16.0$ .

Comparison of Figs 11a, 12a, 13a and 14a, with their respective counterparts, Figs. 7a, 8a, 9a, and 10a, reveals that the increase in the Damkohler number does not change the structure of the product distribution. Despite high reaction rates, products are reorganized by the flow in such a way as to force a correspondence between zones of high vorticity and high product concentration. This similarity is in agreement with results of two-dimensional computations.<sup>39-40</sup>

At low Damkohler number, a small reaction rate confines the reaction zone to the initial well-mixed region. At high Damkohler number, the reaction zone undergoes a change as the flow evolves, from a region inside the large cores/rods to a thin zone around their outer boundaries. This is expected since fast reaction rates lead to "complete" combustion in well-mixed zones and therefore to the migration of the reaction zone to reactants-rich regions.

As shown in Fig. 11b, the product concentration reaches values close to one inside the core of the spanwise eddy. Similarly, the section located at  $y = 1.6$ , shown in Fig. 12b, indicates that the reaction rate drops first at the center of the eddy. At late stages, the reaction zone migrates towards the outer edges of the eddy core. Burning takes place in thin regions located around the outer edges of the core of vorticity, while little or no reaction occurs within the core. A similar redistribution of the reaction zone is observed in the spanwise plane  $y = 3.3$ . However, this effect is less pronounced near the spanwise core, while the braids continue to support the chemical reaction. The difference between the two sections is related to the presence of streamwise vortices whose stirring action results in enhanced transverse diffusion fluxes.

The mechanisms by which the streamwise vortices enhance the rate of burning differ between the core and braid regions. Within the core, streamwise vortices, generated by the deformation of the core itself, cause a spinning motion that is weakly affected by the underlying two-dimensional flow. This results in a limited enhancement in burning rates within a large, product-dominated zone. On the other hand, despite the presence of streamwise vortex rods within the braids, the strain field associated with the underlying two-dimensional flow prevents the formation of a thick product region. Hence, high product concentrations and high reaction rates coexist in this region.

The streamwise sections of Figs. 13b and 14b provide another view of the evolution of the reaction zone in the spanwise direction. At  $t = 12.0$ , the deformation of the product interfaces is dictated by the growth of three-dimensional instabilities. Combustion occurs in two thin layers enclosing the spanwise vorticity core, and in the braids which start to roll under the action of the streamwise vortex rods. At later stages, the reaction becomes confined to the core of the vortex rods and a thin layer trapped between the braids and the core region. The region of lowest reaction rate, located within the spanwise core, corresponds to a zone of small streamwise vorticity separating neighboring vortices. On the other hand, cross-sections of the braids shown in Fig. 14b confirm our earlier claim regarding the competing influence of the streamwise vortex rods and of the two-dimensional strain field. Despite the extreme thinning of the braids by the strain field of the spanwise core, and the continuous entrainment of the products of reaction, the braids support high reaction rates and high product concentration near the axes of the vortex rods.

### V.3 TOTAL MASS OF PRODUCTS

The evolution of the total mass of products formed,  $M(t) = \int \rho c_p dx = \sum \rho c_{p,i} dV_i$ , is shown in Fig. 15 for all 21 cases considered. Figure 15 contains three plots, corresponding to (a)  $Pe = 1000$ , (b)  $Pe = 500$ , and (c)  $Pe = 250$ , each showing changes in  $M(t)$  for seven values of the Damkohler number,  $Da = 0.1, 0.2, 0.4, 1.0, 2.5, 5.0$ , and  $10$ . Variations in the Peclet number are found to induce minor changes in the product and reaction zone structures. Thus, at high Peclet numbers, the latter are mainly governed by the convective flow field. However, the reaction rates are strongly dependent on the amount of mixing, and hence on the coefficients of mass diffusion.

At high values of the Damkohler number, the chemical reaction leads to an almost immediate and complete burning of the initial mixed region. Curves corresponding to  $Da \geq 2.5$  are characterized by a short and sharp initial growth period, which does not depend on the Peclet number. This is expected since, for fast chemistry, regions of mixed reactants burn immediately. An abrupt transition to a controlled growth regime follows, indicating that a diffusion-limited reaction is reached.<sup>41</sup> The burning rates in this regime increase with decreasing Peclet numbers, as indicated by the slopes of the corresponding  $M(t)$  curves at later stages between Figs 15a, 15b and 15c.

At low values of the Damkohler number,  $Da \leq 0.4$ , the chemical reaction is too slow for such a transition to occur. The evolution of  $M(t)$  exhibits a monotonic increase throughout the duration of the computations. As previously mentioned, the reaction remains confined to the initial mixed region. This observation is supported by noting that the mass of products formed at the end of the computations at low Damkohler number is less than that reached at the time of the transition to diffusion-limited regime in the high Damkohler number computations. This explains the fact that, at late stages, the burning rates at low Damkohler number are higher than those at high Damkohler number,



and that gains in the amount of products formed achieved by decreasing the Peclet number are smaller when the Damkohler number is small.

## VI CONCLUSIONS

In this work, the evolution of reacting shear layers are numerically determined in the high Peclet number regime, for a wide range of Damkohler numbers. Computed results show that the product distribution is shaped by the convective field induced by spanwise and streamwise vortex structures which form due to the growth of essential instability of the flow. The rollup of spanwise vorticity leads to the creation of concentrated vortex cores, and braids which join neighboring cores. Entrainment currents associated with these structures force the migration of products from the braids towards the cores, while their induced strain field causes a severe thinning of the braids and of the reaction zone supported therein. However, streamwise vortices, which are generated as a result of growth of three-dimensional instability and are intensified by stretch, significantly affect the flow at later stages, resulting in substantial deviation from the two-dimensional situation.

The maturation of the streamwise vortices into strong streamwise rods, and the amplification of the translative instability are accompanied by spanwise variations in the reacting field and the formation of mushroom structures. Mixing and burning enhancement is achieved through the transverse entrainment fluxes. The entrainment fluxes cause a reorganization of the product distribution such that zones of high product concentration always correspond to zones of high magnitude of vorticity. Thus, products tend to migrate towards the core of the spanwise vortices and towards the axes of the streamwise vortex rods.

While the product distribution is dictated by the flow, and is insensitive to variation of the Damkohler number, the structure of the reaction zone depends strongly on the latter. At low Damkohler number, combustion occurs in distributed zones located within the cores of the vortices, and is confined to the initial, well-mixed region. As the Damkohler number increases, complete combustion is achieved within the cores of the vortices, thus causing a migration of the reaction zone towards their outer edges. The motion of the reaction zone towards regions of higher strain rates result in a substantial change in its structure, as considerable thinning of the latter is observed. Extension of the computations to study pairing among several eddies and to accommodate high heat release, compressible flow models with complex chemical reactions, is currently contemplated.

#### ACKNOWLEDGEMENT

This work is supported by the Air Force Office of Scientific Research Grant AFOSR 84-0356, the National Science Foundation Grant CBT-8709465 and the Department of Energy Grant DE-FG04-87AL44875. Computer support is provided by the John von Neumann National Supercomputer Center.

..

## REFERENCES

- <sup>1</sup>Ghoniem, A.F., Aly, H., and Knio, O.M., "Three-dimensional Vortex Simulation with Application to Axisymmetric Shear Layer," AIAA Paper 87-0379, Jan. 1987.
- <sup>2</sup>Knio, O.M., and Ghoniem, A.F., "On the Formation of Streamwise Vorticity in Turbulent Shear Flows," AIAA Paper 88-0728, Jan. 1988.
- <sup>3</sup>Knio, O.M., and Ghoniem, A.F., "Numerical Study of a Three-Dimensional Vortex Method," Journal of Computational Physics, Vol. 86, January 1990, pp. 75-106.
- <sup>4</sup>Knio, O.M., and Ghoniem, A.F., "Three-Dimensional Vortex Simulation of Entrainment Augmentation Due to Streamwise Vortex Structures," AIAA Paper 89-0574, Jan. 1989.
- <sup>5</sup>Knio, O.M., and Ghoniem, A.F., "Three-Dimensional Vortex Simulation of Rollup and Entrainment in a Shear Layer," Journal of Computational Physics, in press, 1990.
- <sup>6</sup>Bernal, L.P., and Roshko, A., "Streamwise Vortex Structure in Plane Mixing Layers," Journal of Fluid Mechanics, Vol. 170, September 1986, pp. 499-525.
- <sup>7</sup>Breidenthal, R.E., "A Chemically-Reacting, Turbulent Shear Layer," Ph.D. Thesis, California Institute of Technology, 1978.
- <sup>8</sup>Jimenez, J., "A Spanwise Structure in the Plane Shear Layer," Journal of Fluid Mechanics, Vol. 132, July 1983, pp. 319-336.
- <sup>9</sup>Jimenez, J., Cogollos, M., and Bernal, L.P., "A Perspective View of the Plane Mixing Layer," Journal of Fluid Mechanics, Vol. 152, March 1985, pp. 125-143.
- <sup>10</sup>Lasheras, J.C., and Choi, H., "Three-Dimensional Instability of a Plane Free Shear Layer: An Experimental Study of the Formation and Evolution of Streamwise Vortices," Journal of Fluid Mechanics, Vol. 189, April 1988, pp. 53-86.
- <sup>11</sup>Michalke, A., "On Spatially Growing Disturbances in an Inviscid Shear Layer," Journal of Fluid Mechanics, Vol. 23, November 1965, pp. 521-544.

- <sup>12</sup>Pierrehumbert, R.T., and Widnall, S.E., "The Two- and Three-Dimensional Instabilities of a Spatially Periodic Shear Layer," Journal of Fluid Mechanics, Vol. 114, January 1982, pp. 59-82.
- <sup>13</sup>Riley, J.J., Metcalfe, R.W., and Orszag, S.A., "Direct Numerical Simulation of Chemically-Reacting Turbulent Mixing Layers," Physics of Fluids, Vol. 29, February 1986, pp. 406-422.
- <sup>14</sup>Riley, J.J., and McMurtry, P.A., "The Use of Direct Numerical Simulation in the Study of Turbulent, Chemically-Reacting Flows," in Turbulent Reactive Flows, R. Borghi and S.N.B Murthy, eds., Springer-Verlag, New York, 1989, pp. 486-514.
- <sup>15</sup>Lowery, P.S., Reynolds, W.C., and Mansour, N.N., "Passive Scalar Entrainment and Mixing in a Forced Spatially Developing Mixing Layer," AIAA Paper 87-0132, Jan. 1987.
- <sup>16</sup>McMurtry, P.A., Riley, J.J., and Metcalfe, R.W., "Effects of Heat Release on the Large-Scale Structure in Turbulent Mixing Layers," Journal of Fluid Mechanics, Vol. 199, February 1989, pp. 297-332.
- <sup>17</sup>Heidarinejad, G., and Ghoniem, A.F., "Vortex Simulation of the Reacting Shear Layer; Effects of Reynolds and Damkohler Number," AIAA Paper 89-0573, Jan. 1989.
- <sup>18</sup>Leonard, A., "Computing Three-Dimensional Incompressible Flows With Vortex Elements," Annual Review of Fluid Mechanics, Vol. 17, 1985, pp. 523-559.
- <sup>19</sup>Beale, J.T., and Majda, A., "High Order Accurate Vortex Methods with Explicit Velocity Kernels," Journal of Computational Physics, Vol. 58, April 1985, pp. 188-208.
- <sup>20</sup>Agishtein, M.E., and Migdal, A.A., "Dynamics of Vortex Surface in Three Dimensions: Theory and Simulations," preprint, 1989.
- <sup>21</sup>Bathe, K.-J., Finite Element Procedures in Engineering Analysis, Prentice Hall, New Jersey, 1982.

- <sup>22</sup>Beale, J.T., and Majda, A., "Vortex Methods. I: Convergence in Three Dimensions," Mathematics of Computation, Vol. 39, July 1982, pp. 1-27.
- <sup>23</sup>Beale, J.T., and Majda, A., "Vortex Methods. II: Higher Order Accuracy in Two and Three Dimensions," Mathematics of Computation, Vol. 39, July 1982, pp. 29-52.
- <sup>24</sup>Beale, J.T., "A Convergent 3-D Vortex Method With Grid-Free Stretching," Mathematics of Computation, Vol. 46, April 1986, pp. 401-424.
- <sup>25</sup>Hald, O., "Convergence of Vortex Methods for Euler's Equations. II" SIAM Journal on Numerical Analysis, Vol. 16, October 1979, pp. 726-755.
- <sup>26</sup>Anderson, C., and Greengard, C., "On Vortex Methods," SIAM Journal on Numerical Analysis, Vol. 22, June 1985, pp. 413-440.
- <sup>27</sup>Raviart, P.A., "Particle Numerical Models in Fluid Dynamics," Numerical Methods For Fluid Dynamics II, K.W. Morton and M.J. Baines, eds., Clarendon Press, Oxford, 1986, pp. 231-253.
- <sup>28</sup>Mas-Gallic, S., "Methode Particulare Pour Une Equation de Convection-Diffusion," Comptes Rendus de L'Academie des Sciences. Serie I, Mathematique, Vol. 305, September 1987, pp. 431-434.
- <sup>29</sup>Winckelmans, G., and Leonard, A., "Improved Vortex Methods for Three-Dimensional Flows," Mathematical Aspect of Vortex Dynamics, R.E. Caflish, ed., SIAM, Philadelphia, 1989, pp. 25-35.
- <sup>30</sup>Degond, P., and Mas-Gallic, S., "The Weighted Particle Method for Convection-Diffusion Equations. Part 1: The Case of an Isotropic Viscosity," Mathematics of Computation, Vol. 53, October 1989, pp. 485-507.
- <sup>31</sup>Degond, P., and Mas-Gallic, S., "The Weighted Particle Method for Convection-Diffusion Equations. Part 2: The Anisotropic Case," Mathematics of Computation, Vol. 53, October 1989, pp. 509-525.

<sup>32</sup>Ghoniem, A.F., and Sherman, F.S., "Grid-Free Simulation of Diffusion Using Random Walk Methods," Journal of Computational Physics, Vol. 61, October 1985, pp. 1-37.

<sup>33</sup>Ghoniem, A.F., Heidarinejad, G., and Krishnan, A., "Numerical Simulation of a Thermally Stratified Shear Layer Using the Vortex Element Method," Journal of Computational Physics, Vol. 79, November 1988, pp. 135-166.

<sup>34</sup>Ashurst, W.T., and Meiburg, E., "Three-Dimensional Shear Layers Via Vortex Dynamics," Journal of Fluid Mechanics, Vol. 189, April 1988, pp. 87-116.

<sup>35</sup>Metcalf, R.W., Orszag, S.A., Brachet, M.E., Menon, S., and Riley, J.J., "Secondary Instability of a Temporally Growing Mixing Layer," Journal of Fluid Mechanics, Vol. 184, November 1987, pp. 207-243.

<sup>36</sup>Corcos, G.M., and Lin, S.J., "The Mixing Layer: Deterministic Models of a Turbulent Flow. Part 2. The Origin of the Three-Dimensional Motion," Journal of Fluid Mechanics, Vol. 139, February 1984, pp. 67-95.

<sup>37</sup>Lin, S.J., and Corcos, G.M., "The Mixing Layer: Deterministic Models of a Turbulent Flow. Part 3. The Effect of Plane Strain on the Dynamics of Streamwise Vortices," Journal of Fluid Mechanics, Vol. 141, April 1984, pp. 139-178.

<sup>38</sup>Widnall, S.E., and Tsai, C.-Y., "The Instability of the Thin Vortex Ring of Constant Vorticity," Proceedings of the Royal Society, Vol. 287 A1334, October 1977, pp. 273-305.

<sup>39</sup>Ghoniem, A.F., Knio, O.M., and Heidarinejad, G., "The Structure of the Reaction Zone in a Reacting Mixing Layer," Proceedings 12th International Colloquium on Dynamics of Explosions and Reactive Systems, A. Kuhl, ed., in press, 1989.

<sup>40</sup>Ghoniem, A.F., Knio, O.M., and Krishnan, A., "Lagrangian Simulation of the Initial Stages of a Reacting Jet", 23rd Symposium (International) on Combustion, in press, 1989.

<sup>41</sup>Mungal, M.G., and Frieler, C.E., "The Effects of Damkohler Number in a Turbulent Shear Layer," Combustion and Flame, Vol. 71, January 1988, pp. 23-34.

## FIGURE CAPTIONS

Figure 1. Three-dimensional perspective view of the material surface initially lying in the plane  $z = 0$ , and carrying the highest spanwise vorticity. The plots are generated at  $t = 12.0$  and  $16.0$  from the point of view of an observer located at  $(48, 24, 48)$ .  $x$ - denotes the streamwise direction,  $y$ - the spanwise direction, and  $z$ - is cross-stream direction. A constant- $y$  plane is called a spanwise section, while a constant- $x$  is called a streamwise section.

Figure 2. Intersection of the Lagrangian mesh at  $t = 18.0$  with the planes defined by (a)  $y = 3.3$ , (b)  $y = 1.6$ , (c)  $x = 6.6$  and (d)  $x = 2.0$ . Results are obtained using rectangular transport elements.

Figure 3. Contours of the spanwise vorticity,  $\omega_y$ , shown in the  $x$ - $z$  plane located at  $y = 3.3$ . The plots are generated at  $t = 12.0$  and  $16.0$ . Dashed lines are used to represent negative values.

Figure 4. Contours of the spanwise vorticity,  $\omega_y$ , shown in the  $x$ - $z$  plane located at  $y = 1.6$  at  $t = 12.0$  and  $16.0$ .

Figure 5. Contours of the streamwise vorticity,  $\omega_x$ , shown in the  $y$ - $z$  plane located at  $x = 6.6$  at  $t = 12.0$  and  $16.0$ .

Figure 6. Contours of the streamwise vorticity,  $\omega_x$ , shown in the  $y$ - $z$  plane located at  $x = 2.0$  at  $t = 12.0$  and  $16.0$ .

Figure 7. Contours of (a) product concentration and (b) reaction rate generated in the  $x$ - $z$  plane located at  $y = 3.3$ . The plots are generated at  $t = 12.0$  and  $16.0$  for a reacting layer with  $Da = 0.1$  and  $Pe = 1000$ .

Figure 8. Contours of (a) product concentration and (b) reaction rate generated in the  $x$ - $z$  plane located at  $y = 1.6$ . The plots are generated at  $t = 12.0$  and  $16.0$  for a reacting layer with  $Da = 0.1$  and  $Pe = 1000$ .



Figure 9. Contours of (a) product concentration and (b) reaction rate generated in the  $y$ - $z$  plane located at  $x = 6.6$ . The plots are generated at  $t = 12.0$  and  $16.0$  for a reacting layer with  $Da = 0.1$  and  $Pe = 1000$ .

Figure 10. Contours of (a) product concentration and (b) reaction rate generated in the  $y$ - $z$  plane located at  $x = 2.0$ . The plots are generated at  $t = 12.0$  and  $16.0$  for a reacting layer with  $Da = 0.1$  and  $Pe = 1000$ .

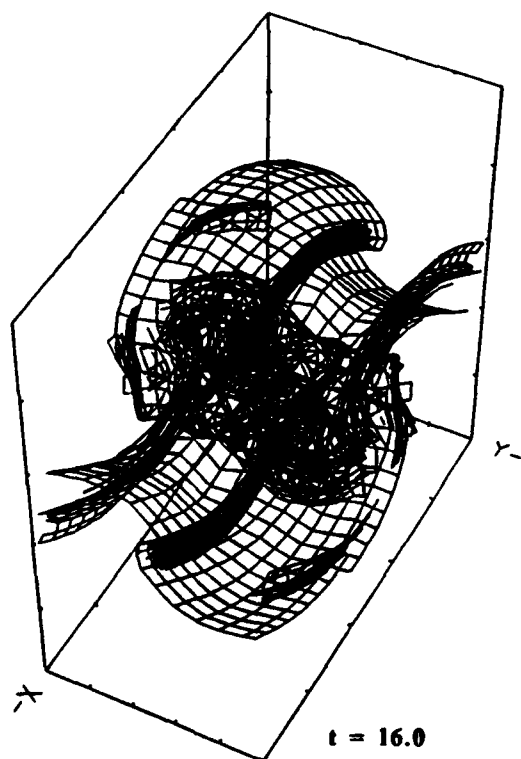
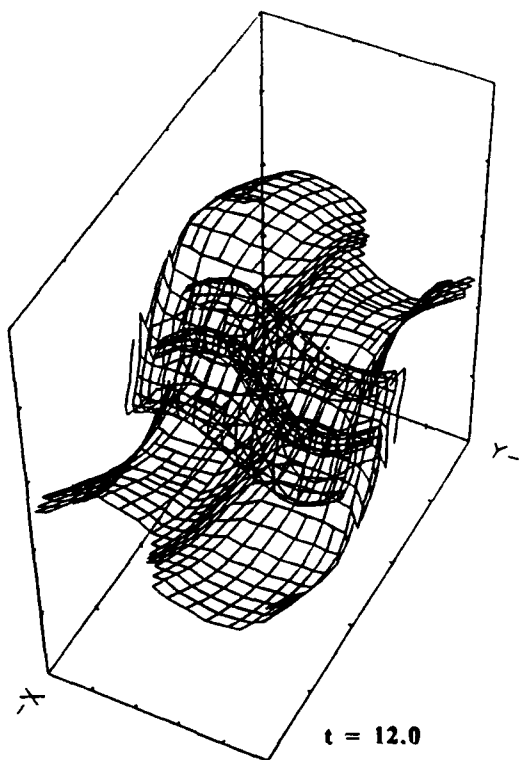
Figure 11. Contours of (a) product concentration and (b) reaction rate generated in the  $x$ - $z$  plane located at  $y = 3.3$ . The plots are generated at  $t = 12.0$  and  $16.0$  for a reacting layer with  $Da = 10$  and  $Pe = 1000$ .

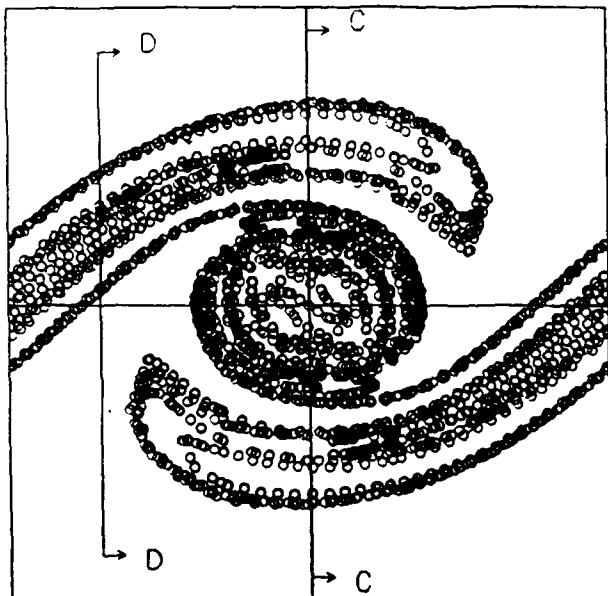
Figure 12. Contours of (a) product concentration and (b) reaction rate generated in the  $x$ - $z$  plane located at  $y = 1.6$ . The plots are generated at  $t = 12.0$  and  $16.0$  for a reacting layer with  $Da = 10$  and  $Pe = 1000$ .

Figure 13. Contours of (a) product concentration and (b) reaction rate generated in the  $y$ - $z$  plane located at  $x = 6.6$ . The plots are generated at  $t = 12.0$  and  $16.0$  for a reacting layer with  $Da = 10$  and  $Pe = 1000$ .

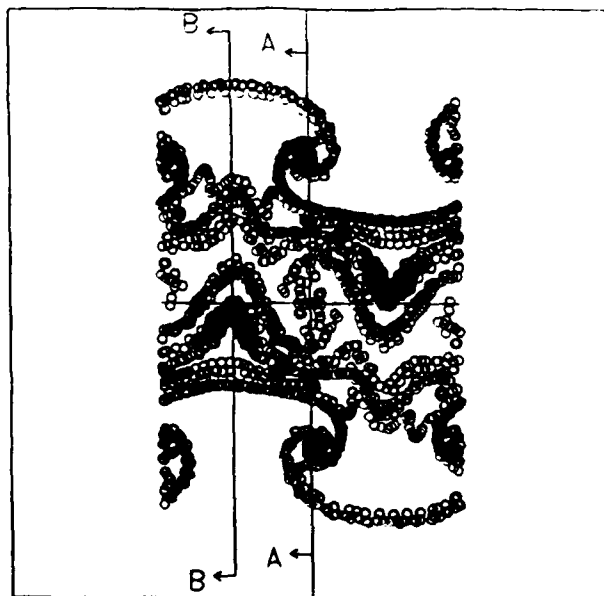
Figure 14. Contours of (a) product concentration and (b) reaction rate generated in the  $y$ - $z$  plane located at  $x = 2.0$ . The plots are generated at  $t = 12.0$  and  $16.0$  for a reacting layer with  $Da = 10$  and  $Pe = 1000$ .

Figure 15. Evolution of the total mass of products,  $M(t)$ , for reacting shear layers at (a)  $Pe = 1000$ , (b)  $Pe = 500$ , and (c)  $Pe = 250$ . In each plot,  $M(t)$  is generated for Damkohler numbers  $Da = 0.1, 0.2, 0.4, 1, 2.5, 5$ , and  $10$ .

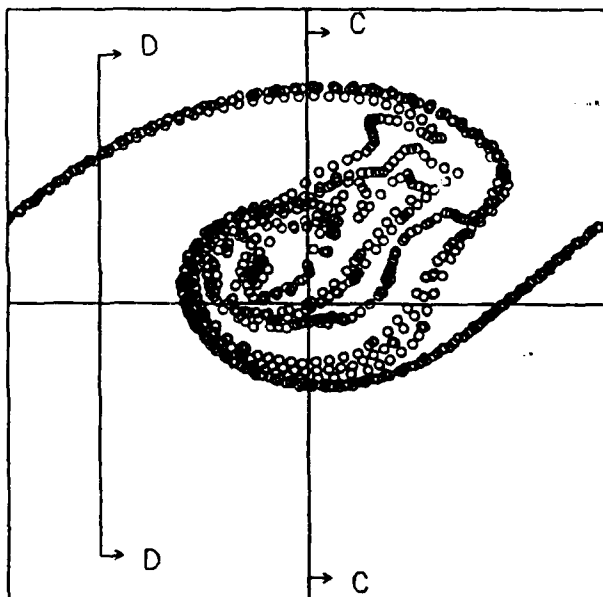




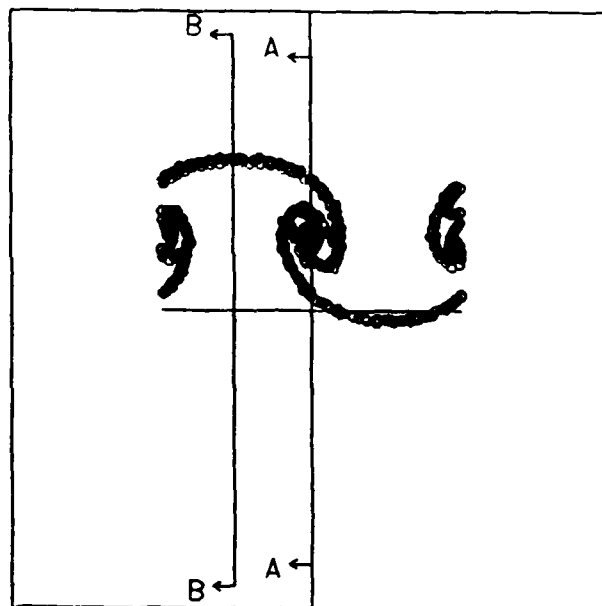
(a)  $y = 3.3$ , (AA)



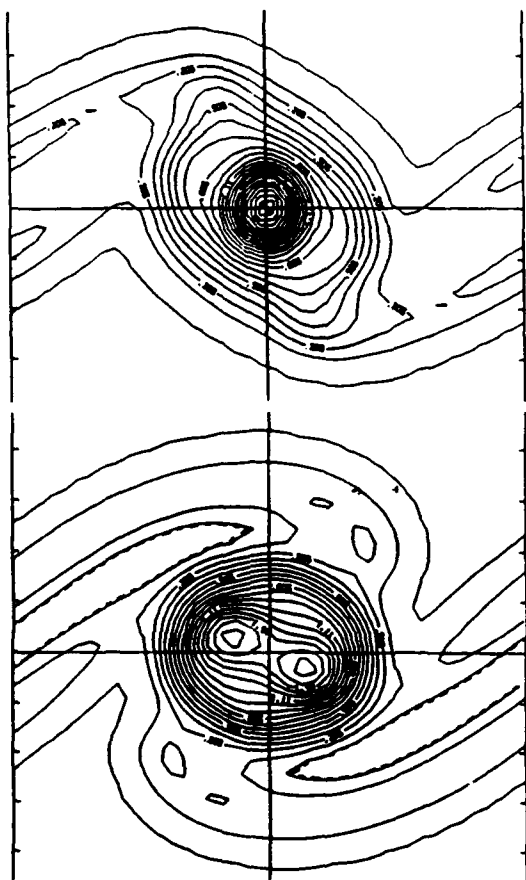
(c)  $x = 6.6$ , (CC)



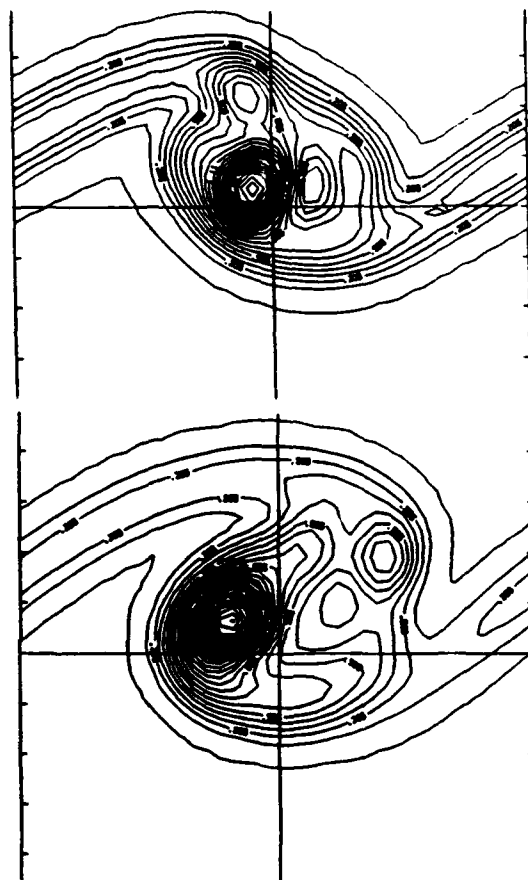
(b)  $y = 1.6$ , (BB)



(d)  $x = 2.0$ , (DD)

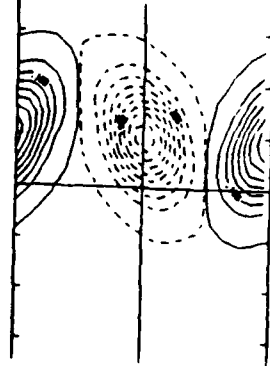
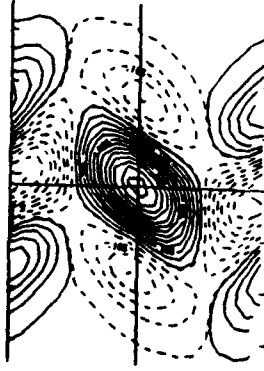


$t = 12.0$

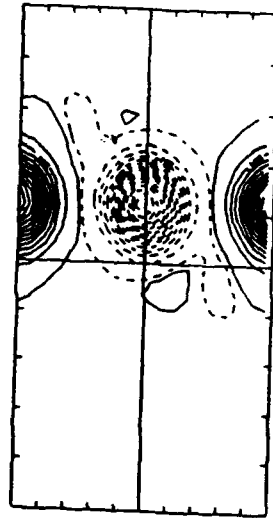


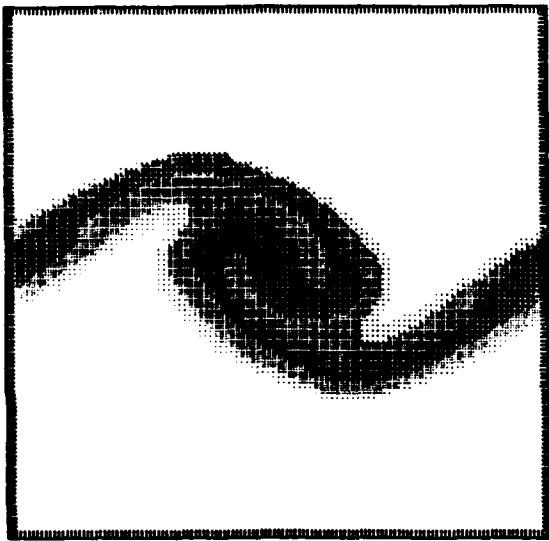
$t = 16.0$

$t = 12.0$

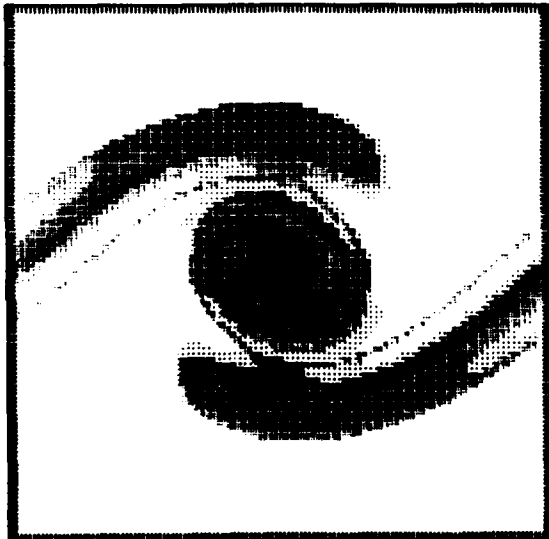
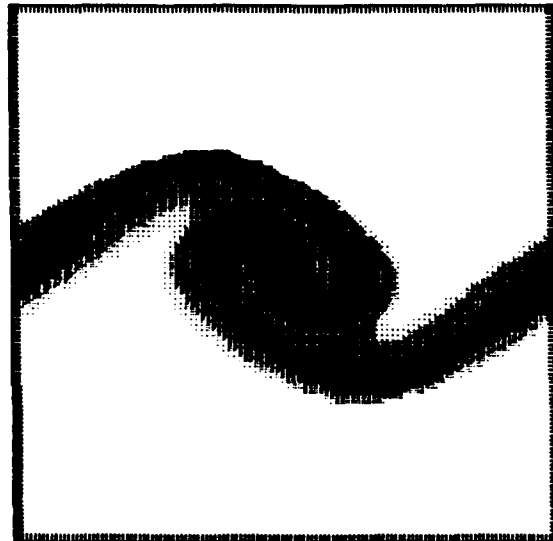


$t = 16.0$

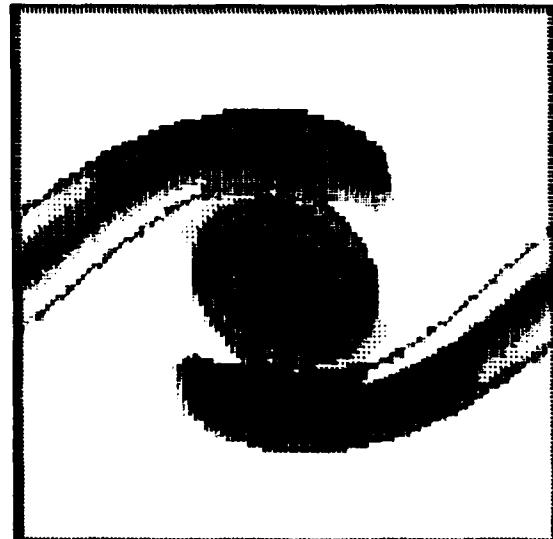




$t = 12.0$

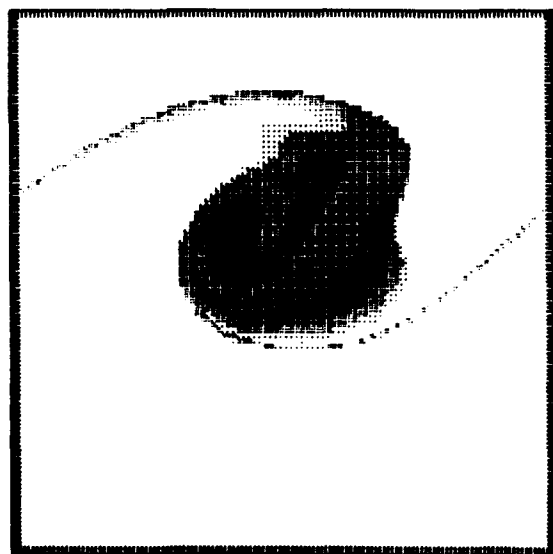
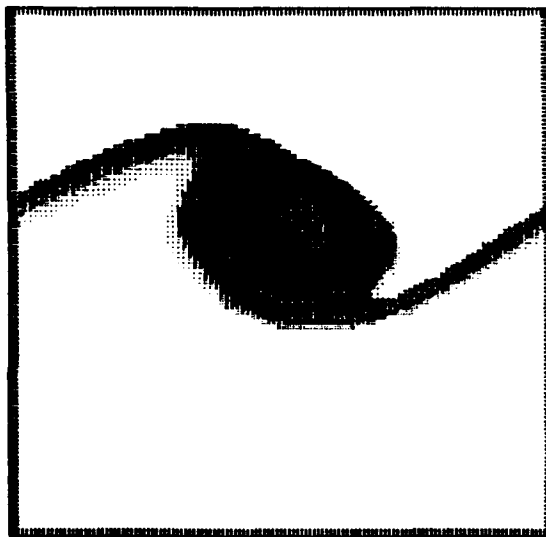


$t = 16.0$

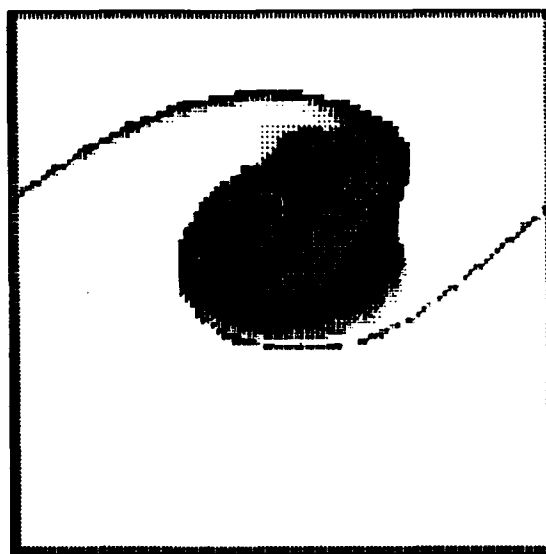


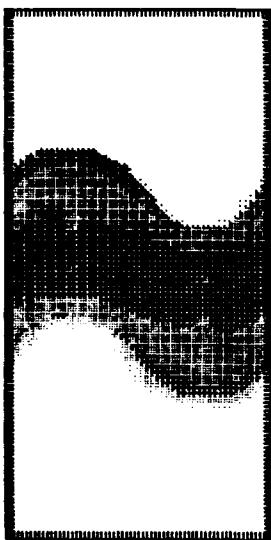


$t = 12.0$

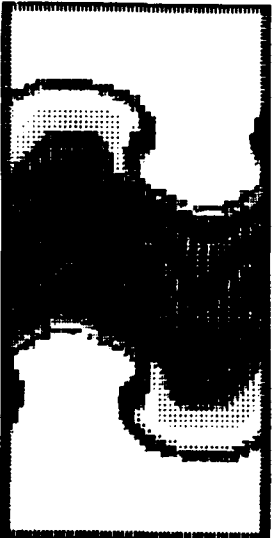
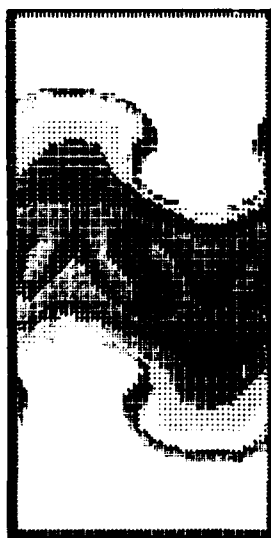
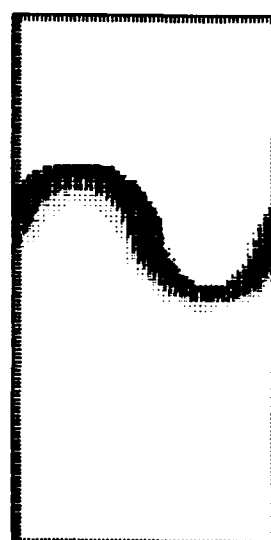
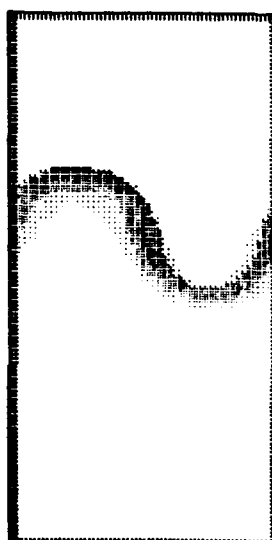


$t = 16.0$

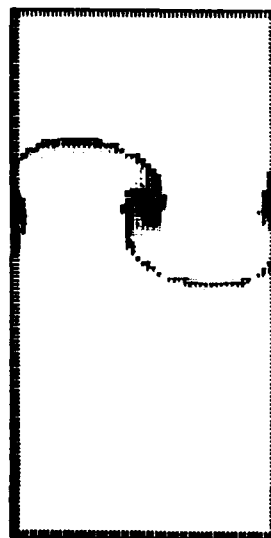




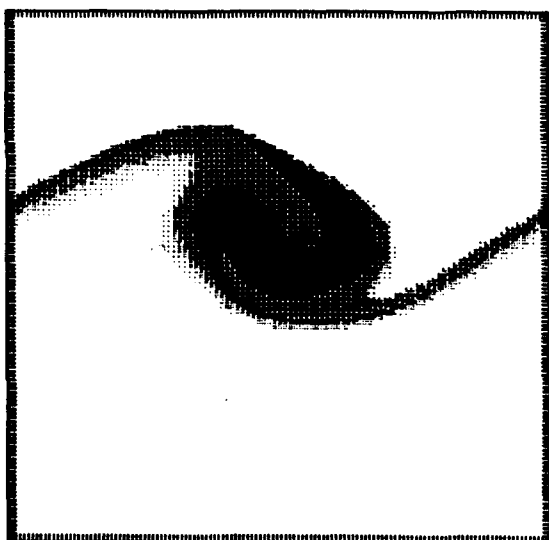
$t = 12.0$



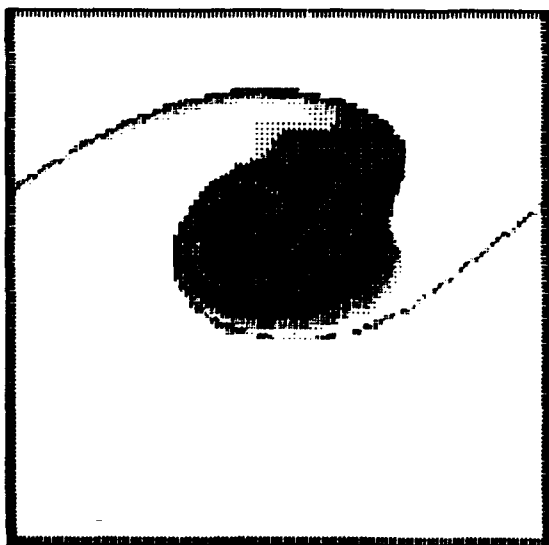
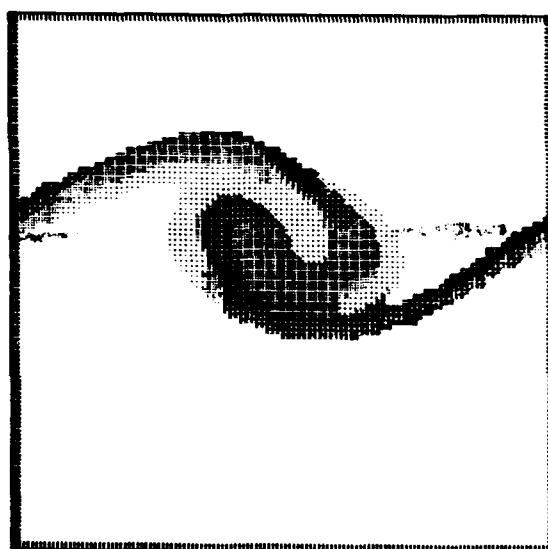
$t = 16.0$





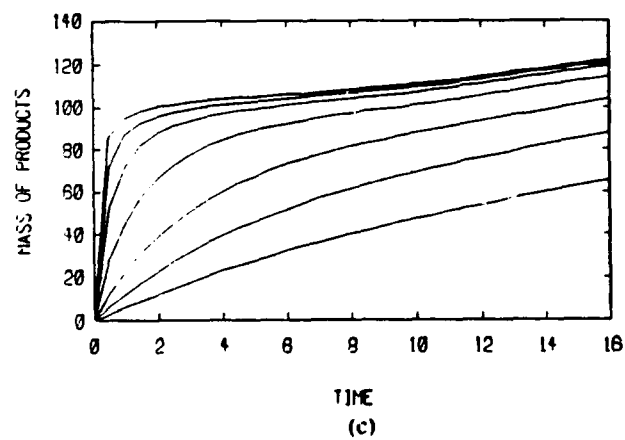
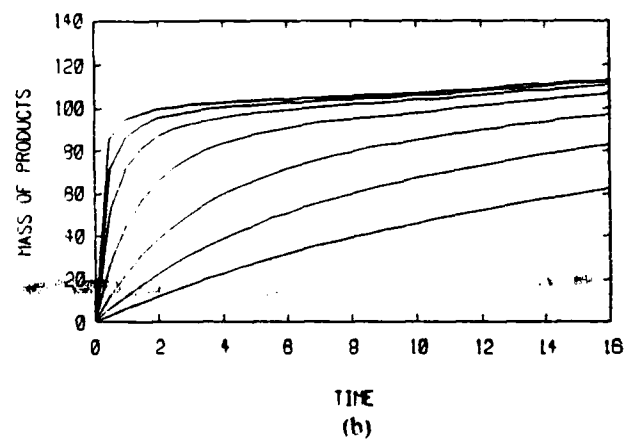
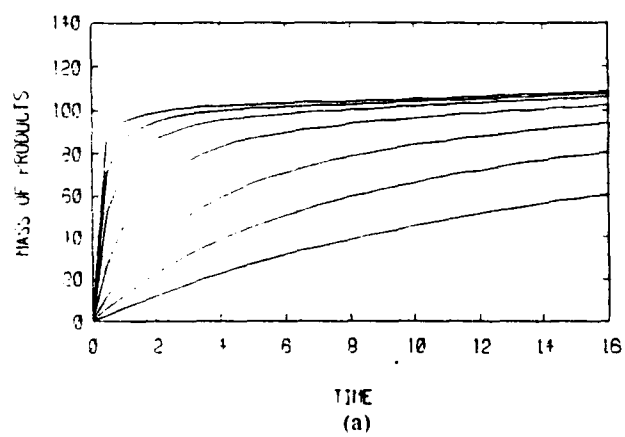


$t = 12.0$



$t = 16.0$





## APPENDIX III

# SIMULATION OF FLOW-COMBUSTION INTERACTIONS IN A SPATIALLY DEVELOPING MIXING LAYER

Marios C. Soteriou<sup>1</sup>, Omar M. Knio<sup>2</sup>, and Ahmed F. Ghoniem<sup>3</sup>  
Massachusetts Institute of Technology  
Cambridge, MA 02139

and

Baki M. Cetegen  
University of Connecticut, Storrs, CT<sup>4</sup>

## ABSTRACT

The transport element method, a Lagrangian, grid-free scheme based on the extension of the vortex method to reacting compressible flow at low Mach number, has been applied to simulate a spatially developing, reacting shear layer with unmixed reactants. The method employs computational elements which move along particle trajectories and transport vorticity and scalar gradients. In the case of a reacting flow, vorticity changes due to density variation, scalar gradients change due to the chemical reaction, and volumetric expansion adds an expansion field. Solutions are obtained for a forced shear layer at different Damkohler numbers and enthalpy of reaction to study the effect of combustion heat release rate on the development of the large scale structures. Forcing is used to ensure roll-up within the computational domain. We show that heat release enlarges the size of the fundamental eddies, stretching their streamwise dimension and slightly reducing their cross stream dimension, while their overall size remains almost the same. Along with forcing at the fundamental and subharmonic frequencies, heat release increases/decreases the size of the in-phase/out-of-phase eddies. The non-uniform acceleration of the eddies in the streamwise direction causes their relative locations to deviate from that of a uniform-density layer and thus modifies the pairing process into a tearing/gulping process. Results also show that the enthalpy of reaction is more important than the reaction frequency factor in affecting the flow dynamics. For the same parameters, the variable-density layer grows slower than its uniform-density counterpart.

## I. INTRODUCTION

Reacting shear flow at high Reynolds number is of fundamental importance to the physics of combustion and to a wide range of engineering applications. Due to the complexity of the problem, numerical simulation has been recognized as an important tool in studying the different phenomena governing turbulent reacting flows [1,2]. To perform these simulations accurately, we have developed a Lagrangian-based, grid-free, adaptive method to simulate reacting shear flow and applied this methodology to several configurations of fundamental and practical significance. This method, the transport element method, has been developed by extending the vortex element method so that compressible flow effects and scalar transport can be included in the simulations. So far, the focus of the application of this method, and most other numerical methods, has been the idealized, temporally evolving layer in which one assumes that a reference frame moving at the phase speed of the fundamental structures follows the evolution of the layer [3-6]. This idealization, however, leaves out several important effects, which the spatially developing shear layer possesses, that have been detected experimentally and recognized in modeling analysis. The purpose of this paper is to apply the transport element method to a spatially developing shear layer and to investigate the effect of heat release on the fluid flow in this problem.

Spatially developing shear layer exhibits an asymmetric entrainment behavior which tends to drift the composition of the large scale structures towards the species convected by the high-velocity stream [7,8]. If the two streams have different densities, or different momenta, that also contributes to the exact composition of the mixed fluid inside the large eddies in ways similar to that of the velocity ratio although through a different mechanism [9]. We found in previous simulations that forcing can alter this composition in a way which depends on the momentum ratio between the two streams. Most of these findings were supported by linear stability analysis and several experimental studies. While it is possible to capture the effect of the density ratio on the change of the composition of the large structures in a temporal simulation, it is not possible to study the effect of the velocity ratio, or the combined effects of the velocity and density ratios, in such a configuration. This is because a temporal simulation assumes perfect dynamic symmetry across the mean velocity contour and any subsequent changes in the layer structures are limited by this restriction. Our analysis of the spatially developing

---

Copyright © 1992 by A.F. Ghoniem. Published by the American Institute of Aeronautics and Astronautics, Inc., with permission.

<sup>1</sup> Graduate research assistant.

<sup>2</sup> Currently, assistant professor, Johns Hopkins University, Baltimore, MD, member AIAA.

<sup>3</sup> Associate professor, associate fellow of AIAA.

<sup>4</sup> Assistant professor, member AIAA.

variable-density shear layer showed that the results of the temporal analysis are either limited to a narrow range of parameters or are literally wrong if the effect of forcing is considered. We conclude that it is necessary to perform spatially developing shear layer simulations if the physics of the reacting flow are to be properly modeled.

The simulations of reacting, spatially developing mixing layers with uniform density, i.e., when the dynamic effects of heat release were neglected, have been used before to discern the structure of the reaction zone and the effects of the Damkohler number on the relative location of the reaction zone with respect to the large structures. It was concluded that at small Damkohler number, the reaction is most intense near the center of the large eddies, while as the Damkohler number increases, the reaction zone moves outwards towards the outer edges of the eddies. The exact thickness of the reaction zone, which resembles that of a strained diffusion flame, is a function of the Damkohler and Reynolds numbers. It was also found that, under conditions of unity stoichiometry, a strong similarity exists between the products concentration field and the vorticity field, suggesting a possible modeling approach for this problem. In all these simulations, the flow was restricted to uniform density. The results of the spatially developing, nonreacting, variable density shear layer showed that even without volumetric expansion, density variation can influence the layer dynamics in a nontrivial way. Thus, it is important to introduce the dynamic effects of heat release into the spatially developing layer simulations.

Dynamic effects of heat release have been demonstrated before in a temporally developing shear layer. There are two controversial issues regarding the effect of combustion on the flow dynamics: (a) whether heat release reduces the growth rate of the layer via baroclinic vorticity generation or via volumetric expansion; and (b) whether there is actually a substantial reduction in the size of the eddies or it is just a delay in the instability development. Although it has been established that heat release at the early stages can reduce the growth rate of the layer, it was also found that forcing beyond the linear range can be used to overcome this effect. This was demonstrated in the temporal layer only and will be investigated in the spatial case in this paper. Deciding on the separate role of baroclinic vorticity and volumetric expansion requires simulations in which one mechanism is disabled while the other is active. This will be the subject of future work. The second issue could not be resolved by the temporal simulations only since the behavior of the spatially developing layer differs from that of the temporal layer especially in the pairing mode which dominates the activities in the downstream section.

In this paper, we present simulations of a spatially developing shear layer and use our results to answer some of these questions. We introduce the extension of the transport element method to a reacting compressible flow and its application to the spatially growing shear layer. We then present results of a nonreacting and reacting shear layer at different rates of heat release.

## II. FORMULATION AND NUMERICAL SCHEME

We consider the motion of a two-dimensional, compressible, chemically reacting flow at low-Mach number and high Reynolds number. We assume that both reactants and products behave as perfect gases with equal molecular weight and constant transport properties, that the reaction is single step and the kinetics are of the Arrhenius type. Under these assumptions the governing equations in non-dimensional form are:

$$\frac{D\rho}{Dt} + \rho \vec{\nabla} \cdot \vec{u} = 0 \quad (1)$$

$$\rho \frac{D\vec{u}}{Dt} = -\vec{\nabla} p \quad (2)$$

$$\frac{Ds_j}{Dt} = \frac{1}{Pe_j} \nabla^2 s_j + Q_j \dot{\omega} \quad (3)$$

$$\rho T = 1 \quad (4)$$

where  $\nabla = (\frac{\partial}{\partial x}, \frac{\partial}{\partial y})$  is the gradient operator,  $\frac{D}{Dt} = \frac{\partial}{\partial t} + \vec{u} \cdot \nabla$  is

the material derivative,  $\rho$  is the mixture density,  $t$  is time,  $\vec{u} = (u, v)$  is the velocity vector in an  $(x, y)$  right-handed coordinate system and  $p$  is pressure. The model requires the transport of three scalars  $s_j, j = 1, 2, 3$ : the temperature,  $T$ , and the reactants' mass fractions,  $Y_1$  and  $Y_2$ . The product mass fraction is  $Y_p = 1 - (Y_1 + Y_2)$ . The reaction rate is

$\dot{\omega} = A_f \rho Y_1 Y_2 \exp(-\frac{T_a}{T})$  where  $A_f$  is the non-dimensional frequency factor and  $T_a$  is the normalized activation energy. For temperature transport  $Pe_j = Pe$ , the Peclet number, and  $Q_j = Q \phi$  where  $Q$  is the enthalpy of reaction and  $\phi$  is the mass stoichiometry. For the reactants  $Pe_j = Pe Le$  where  $Le$  is the Lewis number. For  $Y_1, Q_j = -\phi$  and for  $Y_2, Q_j = -1$ . Both the Lewis number and the stoichiometry are assumed equal to unity.

The vorticity equation is obtained by taking the curl of equation (2):

$$\frac{D\omega}{Dt} \vec{k} = \frac{\vec{\nabla} \rho \times \vec{\nabla} p}{\rho^2} - (\vec{\nabla} \cdot \vec{u}) \omega \vec{k} \quad (5)$$

and the scalar gradient equation by taking the gradient of equation (3):

$$\frac{D\vec{g}_j}{Dt} = -\vec{g}_j \cdot \nabla \vec{u} - \vec{g}_j \times (\omega \vec{k}) + \frac{1}{Pe_j} \nabla^2 \vec{g}_j + Q_j \frac{d\dot{\omega}}{ds_j} \vec{g}_j \quad (6)$$

where  $\omega = \frac{\partial v}{\partial x} - \frac{\partial u}{\partial y}$  is the vorticity,  $\vec{g}_j = \vec{\nabla} s_j$  the scalar gradient and  $\vec{k}$  is a unit vector normal to the plane of motion. The density gradient is obtained from the temperature gradient using equation (4) and the pressure gradient from the velocity field using equation (2). The velocity is decomposed into a vorticity induced solenoidal component and two irrotational components; one induced by volumetric expansion and the other by the boundary conditions ( $\vec{u} \cdot \vec{n}$  prescribed at the boundaries,  $\vec{n}$  denoting the unit vector normal to the boundary), i.e.,

$$\vec{u} = \vec{u}_\omega + \vec{u}_e + \vec{u}_p \quad (7)$$

where  $\vec{u}_\omega = \vec{\nabla} \times (\psi \vec{k})$ ,  $\vec{u}_e = \vec{\nabla} \phi_e$ ,  $\vec{u}_p = \vec{\nabla} \phi_p$  and  $\psi, \phi_e, \phi_p$  satisfy:

$$\nabla^2 \psi = -\omega \quad (8)$$

$$\nabla^2 \phi_e = -\frac{1}{\rho} \frac{D\rho}{Dt} \quad (9)$$

$$\nabla^2 \phi_p = 0 \quad (10)$$

respectively.

The numerical integration of the vorticity transport equation starts by writing the vorticity as a summation over the fields of a finite number of vortex elements of finite overlapping circular cores:

$$\omega(\vec{x}, t) = \sum_{i=1}^N \Gamma_i(t) f_\delta(|\vec{x} - \vec{\chi}_i(t)|) \quad (11)$$

where  $\Gamma_i(t) = \omega_i(t) h_i^2(t)$  is the circulation of the  $i$ th element,  $\omega_i(t)$ ,  $\vec{\chi}_i(t)$ , and  $h_i^2(t)$  denote its vorticity, location, and area, respectively, and

$$f_\delta(r) = \frac{1}{\pi \delta^2} \exp\left(-\frac{r^2}{\delta^2}\right) \quad (12)$$

is the second-order Gaussian core function with core radius  $\delta$  used to obtain a second-order discretization of the vorticity field

The vortical velocity,  $\vec{u}_\omega$ , induced by the vorticity field in equation (11) is given in terms of the desingularized Biot-Savart law:

$$\vec{u}_\omega(\vec{x}, t) = \sum_{i=1}^N \Gamma_i(t) K_\delta(\vec{x} - \vec{\chi}_i(t)) \quad (13)$$

where

$$K_\delta(\vec{x}) = \frac{(y, -x)}{2\pi r^2} (1 - \exp(-\frac{r^2}{\delta^2})) \quad (14)$$

is the desingularized kernel of the Biot-Savart integral and  $r = |\vec{x}|$ .

The evolution of the vorticity field is found by updating the locations of the vortex elements, and their associated vorticity values according to equation (5). The locations of the elements are determined by advecting the vortex elements with the local velocity vector along particle trajectories. This is done by integrating:

$$\frac{d\vec{\chi}_i}{dt} = \vec{u}_i \quad (15)$$

with initial condition  $\vec{\chi}_i(\vec{X}_i, 0) = \vec{X}_i$ , i.e.  $\vec{\chi}_i$  is the Lagrangian coordinate of the particle originally located at  $\vec{X}_i$ . Meanwhile, the evolution of the vorticity associated with the elements is established by considering the latter's circulation which evolves according to:

$$\frac{D\Gamma_i(t)}{Dt} = -\frac{\vec{\nabla} \rho_i}{\rho_i} \times \frac{D\vec{u}_i}{Dt} \quad (16)$$

Equation (16) is integrated in two fractional steps. In the first step, the convection step, we have:

$$\frac{D\Gamma_i(t)}{Dt} = 0 \quad (17)$$

and in the second step we add the contribution of the baroclinic torque while approximating the material acceleration of the particle by a two-step iteration forward difference scheme.

Note that the evolution of the vorticity field requires knowledge of the density field which is coupled to the former via the mechanisms of baroclinicity and volumetric expansion. The density field is obtained from the temperature field via a discrete equivalent of equation (4). Similarly, the density gradient is obtained by taking the gradient of equation (4). The expansion velocity  $\vec{u}_e$  can be obtained using equation (9) in a similar fashion to the calculation of the vortical velocity from the vorticity field, i.e.,

$$\vec{u}_e(\vec{x}, t) = \sum_{i=1}^N \left(-\frac{1}{\rho} \frac{D\rho}{Dt}\right)_i h_i^2(t) \nabla G_\delta(\vec{x} - \vec{\chi}_i(t)) \quad (18)$$

where

$$\nabla G_\delta(\vec{x}) = \frac{(x, y)}{2\pi r^2} (1 - \exp(-\frac{r^2}{\delta^2})), \quad r = |\vec{x}| \quad (19)$$

is the desingularized gradient of the kernel of the Poisson equation.

The integration of the scalar gradients transport equation (6) is initiated by discretizing the gradient fields amongst a finite number of transport elements in a similar fashion to the discretization of the vorticity field, i.e.,

$$\vec{g}_f(\vec{x}, t) = \sum_{i=1}^N \vec{\zeta}_{ji}(t) f_\delta(|\vec{x} - \vec{\chi}_i(t)|) \quad (20)$$

where  $\vec{\zeta}_{ji}(t) = \vec{g}_{ji}(t) h_i^2(t)$ , is the weighted scalar gradient of the  $i$ th element and  $\vec{g}_{ji}$  the corresponding gradient.

The scalar fields can be reconstructed from their gradients via a convolution over the discretized field:

$$s_{pf}(\vec{x}, t) = \sum_{i=1}^N \vec{\zeta}_{ji}(t) \cdot \nabla G_\delta(\vec{x} - \vec{\chi}_i(t)) + s_{pf}(\vec{x}, t) \quad (21)$$

where  $s_{pf}(\vec{x}, t)$  is a component added to satisfy the boundary conditions.

To simulate the evolution of the scalar gradient fields, the transport elements are advected in a similar fashion to the vortex elements and their gradients are updated according to equation (6) which is integrated in two fractional steps. In the first step, the convection and reaction step, we consider:

$$\frac{D\vec{g}_j}{Dt} = -\vec{g}_j \cdot \nabla \vec{u} - \vec{g}_j \times (\omega \vec{k}) + Q_j \frac{d\psi}{ds_j} \vec{g}_j \quad (22)$$

Rather than integrating numerically equation (22) an alternative approach is considered. The scalar gradients are related to the Lagrangian deformation of elementary surface elements whose normal coincides with the direction of the gradient. If  $\delta$  denotes such an elementary surface, then the evolution of its absolute value is governed by:

$$\frac{d(\rho|\vec{\delta}|)}{dt} = -\rho|\vec{\delta}| \vec{n} \cdot (\nabla \vec{u} \cdot \vec{n}) \quad (23)$$

where  $\vec{n}$  is a unit vector lying in the direction of the scalar gradient. By considering the dot product of  $\vec{n}$  with equation (22) and utilizing equation (23) it can be shown that:

$$\frac{D}{Dt} \left( \frac{|\vec{g}_j|}{\rho|\vec{\delta}|} \right) = Q_j \frac{d\dot{w}}{ds_j} \left( \frac{|\vec{g}_j|}{\rho|\vec{\delta}|} \right) \quad (24)$$

Equation (3) also suggests that

$$\frac{D(\delta s_j)}{Dt} = Q_j \frac{d\dot{w}}{ds_j} \delta s_j \quad (25)$$

where  $\delta s_j$  is the variation of the scalar. Comparison of equations (24) and (25) implies that:

$$\frac{|\vec{g}_j|}{\rho|\vec{\delta}| \delta s_j} = \text{constant} = C \quad (26)$$

Assuming negligible directional effects of diffusion on the scalar gradients the constant  $C$  depends only on initial conditions. Thus, knowledge of this constant, of the material surfaces (which are readily available in this Lagrangian scheme and should yield both  $\vec{n}$  and  $\vec{\delta}$ ) and of  $\delta s_j$  (via numerical integration of equation (25)) establishes the time evolution of the scalar gradient due to convection and reaction.

In the second fractional step we add the effect of diffusion:

$$\frac{D\vec{g}_j}{Dt} = \frac{1}{Pe_j} \nabla^2 \vec{g}_j \quad (27)$$

This is done by expanding the cores of the elements according to:

$$\delta^2 = \delta_0^2 + \frac{4}{Pe_j} t \quad (28)$$

where  $\delta_0$  is the core radius at time zero.

Previous application of the vortex and transport element method to the spatially-developing, uniform density shear layer has been used to validate the scheme by comparing the numerical results for velocity and scalar concentration statistics to experimental measurements.

### III. FLOW GEOMETRY AND BOUNDARY CONDITIONS

The reacting shear layer is formed by the merging, downstream of a semi-infinite splitter plate of vanishingly small thickness, of two streams of reactant fluids of unequal velocity ( $x=0$ ). The two fluids which are assumed perfect and with the same molecular weight are at the same pressure and temperature, thus, same density. The top stream has velocity  $U_1$  and consists of reactant  $Y_1$ , while the bottom stream has velocity  $U_2$  and consists of reactant  $Y_2$ . Variables are normalized with respect to  $U_1$ ,  $T_0$ , and  $H$ , the top-stream

velocity, the ambient temperature, and the channel height, respectively. The solution domain consists of the channel region lying downstream of the splitter plate and bounded at  $X_{max}$ ,  $0 < x < X_{max}$ ,  $0 < y < H$ . The top and bottom walls are modelled as rigid, slip, impermeable planes, so that the

boundary conditions  $v = 0$  and  $\frac{\partial s_j}{\partial y} = 0$  at  $y = 0$  and  $y = H$  are imposed, where  $s_j$  is any of the three transported scalars  $T$ ,  $Y_1$ ,  $Y_2$ . These conditions are satisfied by conformally mapping the entire channel region on the upper half of a complex plane, and using the appropriate image system of the transport elements. At the downstream section, a condition of vanishing vorticity and scalar gradient is used as outflow boundary condition, and is applied by removing the transport elements which cross the  $x = X_{max}$  plane. At the inlet section, the vorticity, velocity, top reactant mass-fraction-gradient and mass-fraction profiles are specified as follows:

$$\omega(x=0, y, t) = -\frac{U_1 - U_2}{\sqrt{\pi} \sigma} \exp\left(-\frac{(y-0.5H)^2}{\sigma^2}\right) \quad (29)$$

$$U(x=0, y, t) = \frac{U_1 + U_2}{2} + \frac{U_1 - U_2}{2} \operatorname{erf}\left(\frac{y-0.5H}{\sigma}\right) \quad (30)$$

$$\frac{\partial Y_1}{\partial y}(x=0, y, t) = \frac{1}{\sqrt{\pi} (3\sigma/4)} \exp\left(-\frac{(y-0.5H-dy)^2}{(3\sigma/4)^2}\right) \quad (31)$$

$$Y_1(x=0, y, t) = \frac{1}{2} \left( 1 + \operatorname{erf}\left(\frac{y-0.5H-dy}{(3\sigma/4)}\right) \right) \quad (32)$$

where  $\operatorname{erf}$  denotes the error function. The bottom reactant's mass-fraction-gradient and mass-fraction profiles are mirror images of the top reactant's profiles. In equations (29-32),  $\sigma$  denotes the standard deviation of the Gaussian profile which describes the initial vorticity profile. Thus the mass-fraction profiles are thinner than the vorticity-velocity profiles and are displaced about the centerline of the channel by a distance  $dy$ .

The inlet product profiles can be obtained from the reactant profiles via  $Y_p = 1 - (Y_1 + Y_2)$ . The temperature and product profiles are assumed to be similar thus the latter are used to define the former.

$$\frac{\partial T}{\partial y}(x=0, y, t) = T_{fl} \frac{\partial Y_p}{\partial y}(x=0, y, t) \quad (33)$$

$$T(x=0, y, t) = 1 + T_{fl} Y_p(x=0, y, t) \quad (34)$$

where  $T_{fl}$  is the adiabatic flame temperature. The thickness of the vorticity layer,  $2\sigma$ , is scaled so that the height of the channel,  $H$ , equals twice the wavelength of the most unstable fundamental mode of the initial vorticity distribution of the uniform-density layer. For the profiles considered here,  $2\sigma = 0.08 H$ .

Initially the layer is assumed to be flat and the above inlet conditions are assumed valid throughout the domain. The vorticity and scalar-gradient fields are discretized by distributing transport elements over nine material surfaces (lines) lying within the region of significant vorticity and gradient variations. The layers are equally separated with a separation distance  $dy = 0.0234$ , yielding a total thickness of the discretization domain  $\Delta = 0.1875H$  (i.e.  $\Delta > 2\sigma$ ). The initial streamwise separation distance between neighboring elements lying on the same material line,  $dx = dy$ , so that a square Lagrangian mesh is obtained (Fig. 1.). The vorticity and scalar-gradient values associated with the transport

elements are found by matching the discretized and assumed profiles at their centers, i.e., by solving the linear system obtained by equating the left-hand side of equation (11) to that of equation (29) (or that of equation (20) to (31) or (33)), evaluated at  $\bar{X}_i$ . The value of the core radius is found by iteration over those values which ensure strong initial overlap so as to minimize the integral error between the assumed and discretized profile. For the assumed vorticity profile and for the specified mesh, this procedure gives  $\delta = 0.0273$ . This collocation scheme was found to yield more accurate results on the initial growth of the instability waves.

The severe stretching of the Lagrangian mesh used to discretize the vorticity and scalar gradients, which increases the distance between neighboring elements, may lead to the deterioration of the accuracy of the discretization. To overcome this problem, a scheme of local mesh refinement is adopted whereby transport elements are continuously introduced and deleted to ensure overlap of the elements. In our computation, strong overlap is enforced near the inlet of the domain by allowing a small maximum separation between neighboring elements. This condition is relaxed as we approach the exit of the domain by increasing this threshold value, thus allowing for efficient computations without compromising the accuracy of the numerical scheme.

#### IV. RESULTS

The model described in Section III has been used to study the effect of heat release on the dynamics of the spatially growing shear layer and the influence of that on the rate of product formation. In previous studies of temporally growing shear layers and jets, it has been found, especially in a nonpremixed shear layer, that heat release reduces the growth rate of the instability and slows down the roll-up in the linear range. It has been postulated that the volumetric expansion in the reaction zone, which, in the early stages, lies within the vorticity layer, leads to the thickening of the vorticity layer and thus slows down the roll-up. It has also been established by our previous studies on a reacting jet that forcing at relatively large amplitudes can be used to overcome this effect. If the layer is forced into its nonlinear stages via large amplitude oscillations, the effect of heat release on the growth rate of the large eddies is unnoticeable. Thus, in this work, we use large amplitude forcing at the splitter plate to initiate the roll-up before any measurable heat release and thus avoid the suppression of the instability due to exothermic energy. The focus of the current study is, therefore, on the effect of heat release on the large-scale structure.

The forcing function, shown in Fig. 2, consists of a fundamental frequency and its subharmonic frequency. The former is chosen to correspond to the most unstable mode of the uniform density, spatially developing shear layer. It should be noted that it is not possible, within the framework of the linear stability theory, to find the most unstable mode in the variable-density, reacting shear layer since the profiles change with time as energy is deposited. The amplitude of both modes is taken to be the same and is 0.015. Note that, as will be seen, forcing at such high amplitude affects the layer structure in a fundamental way. We observe that due to the presence of two frequencies, one being the subharmonic of the other, two eddies form and then pair. The eddy which forms during the part of the cycle in which the fundamental and the subharmonic components are in-phase is bigger than that which forms in the second part of the subcycle during which the two components are out-of-phase. The difference between the size of the two eddies increases as the amplitude of forcing increases. As we will show, this has an important effect of the pairing dynamics of the reacting shear layer.

We have performed several runs in which the velocity ratio was kept constant,  $r = 1/2$ . The Damkohler number was maintained low by keeping  $A_f = 50-100$ , while the heat release was maintained high by using  $Q = 4-6$ . The non-dimensional activation energy was kept at  $T_a = 10$  in all runs. Calculations of the reacting layer were also performed for a uniform-density flow, i.e., when heat release is not allowed to affect the flow dynamically, to isolate the effect of density variation. Keeping the reaction frequency factor low limits the reaction zone structure to that of a distributed zone in which most of the exothermic energy is deposited inside the large structures. We have shown before that increasing the Damkohler number causes the reaction zone, which starts inside the cores of the large structures, to move towards the outer edges of the eddies and to become a thin reaction zone of the flamelet type. Limiting the simulations to low Damkohler numbers, which is not the general case, is representative of the early stages of development of the reacting layer at an arbitrary Damkohler number since the reaction starts always in the well-mixed zone, i.e., inside the cores of the structures. Thus, we believe that the conclusions of the study apply to a wider range of  $D_a$ .

Figure 3 shows a comparison between the reacting shear layer without and with density variation, in both cases with temperature variation due to the chemical reaction. The computations were performed with  $A_f = 50$  and  $Q = 6$ . The shear layer is depicted using all the vortex elements and their velocity vectors at three time steps. The velocity is plotted with respect to the mean velocity across the shear layer to highlight the boundaries of the large eddies better. We note that density variation, if coupled to temperature variation via the equation of state, leads to the generation of vorticity via the baroclinic effect and to an additional velocity field by the volumetric expansion. The effect of volumetric expansion is clear in the larger velocity vectors in the downstream sections of the shear layer. The cross sections of the eddies in the variable-density shear layer are larger than in the uniform-density layer. If the cross section of the eddy is modeled by an ellipse with a major axis in the streamwise direction and a minor axis in the cross-stream direction, the figure shows that heat release causes the eddies to expand in the streamwise direction so that their major axis increases. On the other hand, the minor axis of the variable density eddies decreases slightly giving the appearance that the roll-up of the fundamental eddies has been suppressed.

The expansion of the eddies in the streamwise direction, and the overall acceleration of the structures as the flow moves downstream, brings the large eddies closer than in the case of the uniform-density case. This has the effect of changing the phase relationship among the neighboring eddies from that imposed by the upstream forcing, i.e., the relative locations of the large eddies are different than that in the uniform-density layer. Since pairing dynamics depend strongly on the phase relationship among neighboring eddies, this change of phase due to energy release, as expected, leads to modifying the pairing dynamics. This is seen in Fig. 3 as the eddies in the uniform-density case pair and form structures which protrude significantly in the cross-stream direction while in the variable-density case, the structures formed by pairing seem to remain flat. The mechanisms by which the two eddies merge in the variable-density case seem to be a merging or "gulfing" more than pairing. It also appears that small eddies are torn between their larger neighbors. The reduction of the cross-stream growth of the layers can be attributed in part to the larger phase velocity of the eddies due to the volumetric expansion.

Figure 3 shows that although heat release contributes to the growth of the structures, it does so primarily in the streamwise direction and thus the growth of the layer, as measured by the cross stream divergence of the boundaries of the vorticity layer, seem to be reduced by heat release. This is



confirmed in Fig. 4 where we compare the results of three cases for which  $A_f = 50$  and  $100$  at  $Q = 4$ , and  $A_f = 50$  at  $Q = 6$ . In these figures we distinguish between the effect of the rate and the amount of energy deposition due to combustion. In the first and last cases, we observe the peculiar behavior that the difference between the sizes of the two eddies which form during one cycle of subharmonic forcing becomes larger. Note that during each cycle of subharmonic forcing, two subcycles of fundamentals exist: one in-phase and one out-of-phase with the subharmonic. Even in the uniform-density layer, the eddy forming during the in-phase subcycle is larger than the eddy which forms during the out-of-phase subcycle. With heat release, the "in-phase" eddies become larger and the "out-of-phase" eddy becomes smaller. This imbalance is clearly seen in Fig. 4 where in the downstream part of the domain, the small, out-of-phase eddies seem to get gulped by the large, in-phase eddies.

The reason why heat release contributes to the faster growth of the in-phase eddy and the slower growth of the out-of-phase eddy is not clear at this point and requires further investigation. What is clear is that as the rate of energy release, as determined by  $A_f$ , or the amount of energy released, as defined by  $Q$ , increase, the difference between the size of the two eddies becomes more pronounced. In both cases, near the downstream end of the domain, the small eddies disappear faster as they are either torn between the two larger neighboring eddies or gulped by either of them. On the other hand, as more heat is deposited inside the large eddies, they expand both in the streamwise and cross stream directions. This expansion is exhibited by the faster growth of the layer with higher heat release than with the lower heat release.

The effect of heat release on the physical size of the layer is depicted in Fig. 5 where we show (a) the product thickness, defined as  $ly(Yp^- = 0.01) - y(Yp^+ = 0.01)$ , and (b) the reaction thickness, defined as  $ly(\dot{w}^- = 0.01 \dot{w}_{max}) - y(\dot{w}^+ = 0.01 \dot{w}_{max})$ , both averaged over 100 time steps, where superscripts + and - indicate increasing and decreasing values of the variables, respectively. These plots, especially the uniform-density and low-heat-release cases, exhibit the trend

previously found in forced shear layers: the thickness first increases due to the formation of the fundamental eddy, stays flat where the structures are essentially convected without interaction, then increases again during pairing. However, as the rate of heat release increases, the size of the structures continues to increase beyond the first stage due to the volumetric expansion resulting from the heat release inside the structures. Moreover, the sudden transition where pairing starts in the uniform-density case disappears. Instead, the thickness seems to keep its gradual rise into the third stage. This corroborates our previous observation that pairing in the uniform density case is replaced by a gradual process of tearing/gulping that leads to the development of the large eddies.

Plots of the layer thickness show that as the rate of heat release increases, the size of the layer grows. Since the growth of the layer is, to a large extent, due to volumetric expansion, one can infer that as the layer thickness grows faster, the amount of product formed also increases. It is interesting to note that while small rates of heat release can reduce the size of the structures and delay the overall growth of the layer with respect to the uniform density layer, as the rate of heat release increases both the overall size of the layer and the rate of product formation become higher. It should be emphasized that this is only true when high amplitude forcing is applied. When we did not force the layer, we found that increasing the heat release rate suppressed the instability leading to the roll-up, and the rate of product formation was reduced. It is probable that stronger subharmonic forcing

would have led to pairing. However, investigating this possibility is left for future work.

The detailed structure of the reacting layer is shown in Fig. 6 for the uniform-density case and Figs. 7 and 8 for the variable-density cases. In these figures, the results within two sections of the computational domain are shown in terms of the product mass-fraction, the reaction rate, and the vorticity. For comparison, Fig. 6 shows the product mass-fraction, reaction rate and vorticity for the uniform-density case with  $A_f = 50$  and  $Q = 6$ . In these computations, the temperature was allowed to vary while the density was maintained constant. The left-hand side of the figure shows the results at the early stages, where the fundamental mode dominates the dynamics, and the right-hand side shows the results in the downstream part where pairing is the dominant mechanism in the dynamics. The results in this figure will be discussed in connection with the results of the variable-density cases.

In Fig. 7, we focus on the fundamental mode and show the above variables in the section  $1.43 < x < 2.43$  at time  $t = 20$  for  $A_f = 50$  and  $Q = 4$  and  $6$ . In Fig. 8, we concentrate on the subharmonic mode and show the same variables in the section  $2.82 < x < 3.82$  at time  $t = 15.5$  for  $A_f = 50, 100$  and  $Q = 4$ . In general we find that increasing the amount of heat release by using larger values of  $Q$  has a stronger effect on the dynamics of the layer than increasing the rate of energy release which is achieved by using larger  $A_f$ . This is exhibited by the extra flattening of the eddies, and their further expansion in the streamwise direction, as the heat release increases by increasing  $Q$  in Fig. 7 than by using higher values of  $A_f$  in Fig. 8. In both figures, increasing the rate of heat release leads to: (a) flattening the eddies although the total cross section remains the same or increases; (b) decreasing the size of the out-of-phase eddy with respect to that of the in-phase eddy; (c) maintaining higher rates of heat release in the braids due to the weaker roll-up; and, (4) modifying the vorticity distribution inside the eddies extensively. Both the product mass-fraction and the reaction rate remain high within the braids as the rate of energy deposition increases indicating that the strain there is reduced, thus the flame is not extinguished to the same degree as in the uniform-density case. In the second section, the fate of the out-of-phase eddies, as they are strained and gulped by the larger, in-phase eddies is also shown. The relative location of the eddies is much different than it was in the uniform density case.

The similarity between the product mass-fraction and the vorticity is observed in these results albeit to a lesser degree than what we observed in the uniform-density case. This is because vorticity generation due to the baroclinic torque, produced as a thin zone of low-density fluid forms within the reaction zone, substantially distorts the original vorticity within the layer. The area where the vorticity is most disturbed by the combustion process is where the reaction zone is. There, the vorticity is intensified around the reaction zone on one side of the eddy and changes sign across the reaction zone on the other side of the eddy. This indicates that baroclinic vorticity plays a significant role in the developing structures of the shear layer. The complex structure of the vorticity field resembles qualitatively that observed in the case of a nonreacting, variable-density shear layer. It is difficult at this stage to distinguish between the role played by the baroclinic vorticity and volumetric expansion since they are strongly connected with the reaction.

The plots of the reaction rate show that the reaction zone becomes almost a ring around the large eddies. While it is clear that at the early stages the reaction starts inside the eddies where the mixed fluid exists, the reaction zone moves outwards in the large eddies as the original mixed reactants are burned and are replaced by two newly entrained streams. The same reaction-zone structure is observed in the downstream

part of the domain where the interaction between the fundamental eddies produce larger structures. Clearly, heat release does not affect the relative position of the reaction zone to the vorticity structures as it changes the latter.

## V. CONCLUSIONS

Reacting shear layer simulations using the transport element method has been used to investigate the effect of heat release on the flow dynamics in a spatially developing flow of nonpremixed reactants. Results were obtained for a uniform-density reacting shear layer and three cases of variable-density reacting shear layers with different enthalpy of reaction and reaction frequency factor. In all cases, a single step, Arrhenius chemical reaction was used to model the combustion process. In all of our calculations, forcing was used to initiate the roll-up process. This is because we found that without forcing, heat release may completely suppress the instability leading to roll-up.

Results indicate that the overall growth rate of the shear layer is reduced due to the heat release when density variation is considered. Increasing the amount of energy deposited is more effective in reducing the growth rate than the rate of energy deposition. In the reacting shear layer, as the rate of energy deposition increases, the rate of growth and the rate of product formation increase. The size of the eddies increases due to the volumetric expansion, and the strain field induced in their braids becomes smaller than that experienced in the uniform density case. Thus, while the reaction rate inside the eddies is reduced due to the slower roll-up, it is increased due to the reduction of strain. Pairing, a process responsible for the growth of the shear layer downstream the roll-up stage, is suppressed. This is due to the change of phase relationship among neighboring eddies due to the acceleration associated with heat release. Pairing is replaced by a process of tearing/gulping in which in-phase eddies exert a strong strain on out-of-phase eddies and absorb their vorticity.

## ACKNOWLEDGEMENT

This work is supported by the Air Force Office of Scientific Research grant 89-0491 and the Gas Research Institute. Computations were performed at the Illinois National Supercomputer center.

## REFERENCES

1. Ghoniem, A.F., "Vortex Simulation of Reacting Shear Flow," Chapter 10 in *Numerical Approaches to Combustion Modeling*, ed by E. Oran and J. Boris, Progress in Aeronautics and Astronautics, Vol. 135, pp. 305-348, 1991.

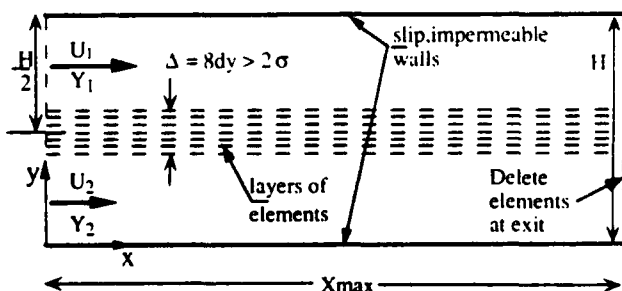


Figure 1. Schematic diagram showing the computational domain and the initial location of the computational elements.

2. McMurtry, P.A. and Givi, P., "Spectral Simulations of Reacting Turbulent Flows," Chapter 9 in *Numerical Approaches to Combustion Modeling*, ed. by E. Oran and J. Boris, Progress in Aeronautics and Astronautics, Vol. 135, pp. 257-303, 1991.
3. Ghoniem, A.F., Knio, O.M. and Krishnan, A., "Lagrangian Simulation of the Initial Stages of a Reacting Jet" the 23rd Symposium (International) on Combustion, The Combustion Institute, Pittsburgh, PA, pp. 699-705, 1990.
4. Ghoniem, A.F., and Krishnan, A., "Origin and Manifestation of Flow-combustion Interactions in a Premixed Shear Layer," the 22nd Symposium (International) on Combustion, the Combustion Institute, Pittsburgh, PA, pp. 665-675, 1988. 22nd Symposium
5. P.A. McMurtry, J.J. Riley and R.W. Metcalfe, *J. Fluid Mech.* **199**, 297 (1989).
6. Knio, O.M. and Ghoniem, A.F. *AIAA Journal*, to appear.
7. A.F. Ghoniem and G. Heidarinejad, "Effect of Two-dimensional Shear Layer Dynamics on Mixing and Combustion at Low Heat Release," *Comb. Sci. Tech.* **72**, 79 (1990).
8. A.F. Ghoniem and G. Heidarinejad, *Comb. Flame* **83**, 1, 1991.
9. Soteriou, M.C., Knio, O.M. and Ghoniem, A.F., "Manipulation of the Growth Rate of a Variable Density, Spatially Developing Mixing Layer via External Modulation," AIAA-91-0081.
10. A.F. Ghoniem and K.K. Ng, "Numerical Study of the Dynamics of a Forced Shear Layer," *Phys. Fluids* **30**, 706, (1987).

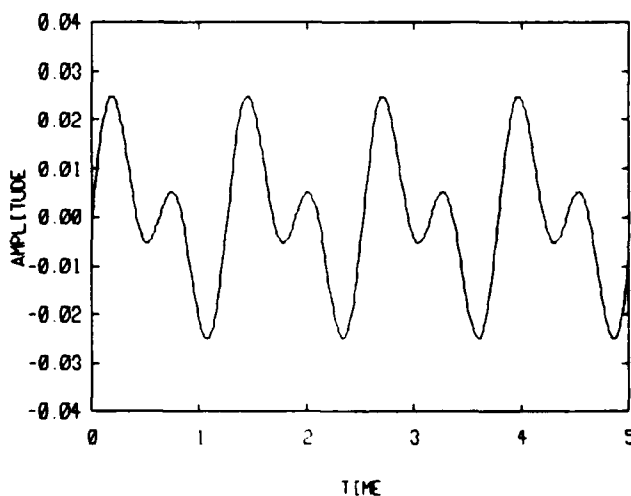


Figure 2. The forcing function used to accelerate the initiation of roll-up and pairing. The displacement shown in the figure represents the location of the computational elements immediately downstream the splitter plate.

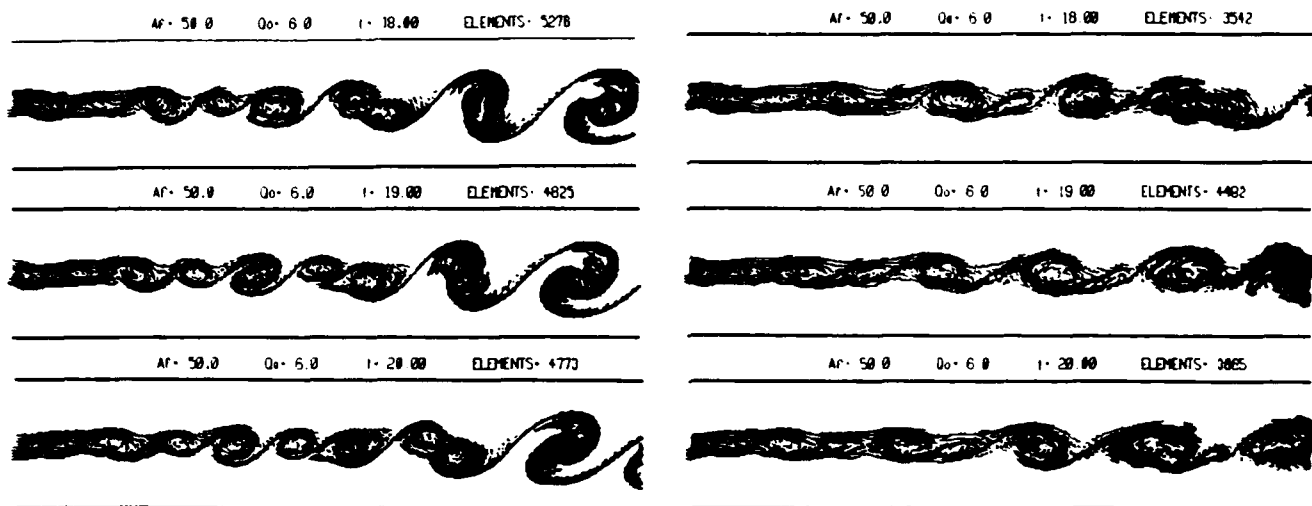


Figure 3. The location and velocity vectors of the vortex elements of the uniform-density (left) and variable-density (right) reacting shear layers, both with  $A_f = 50$  and  $Q = 6$ .

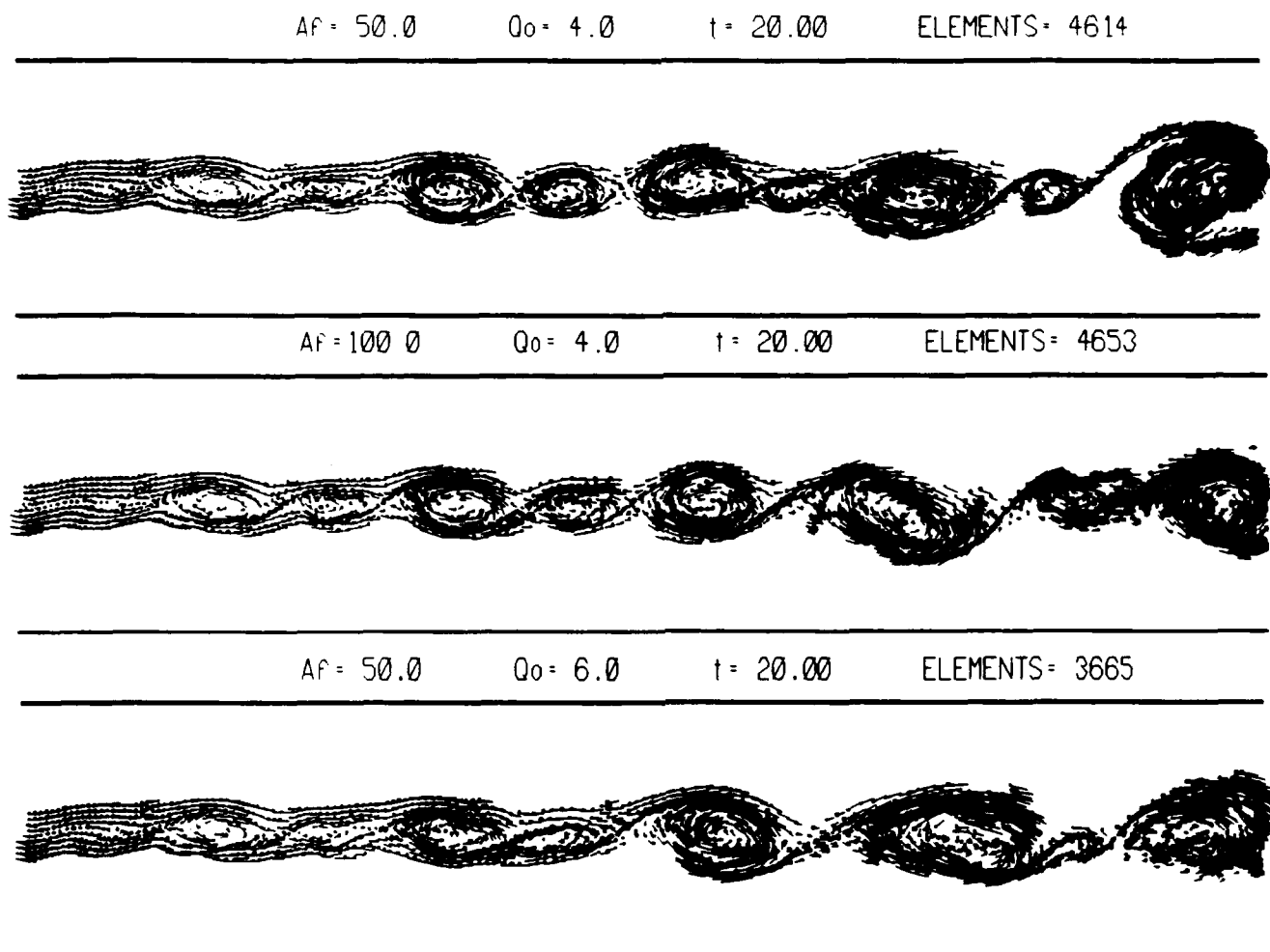


Figure 4. Comparison between three cases of variable density reacting shear layers at different frequency factor and heat release.

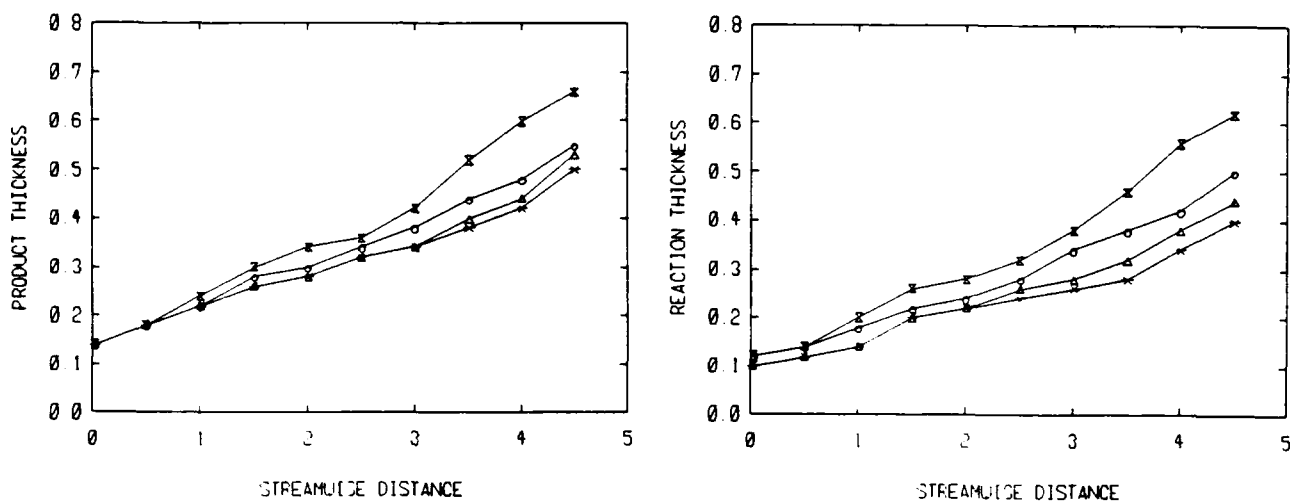


Figure 5. The growth of the reacting shear layer shown in terms of the product thickness (left) and the reaction thickness (right).

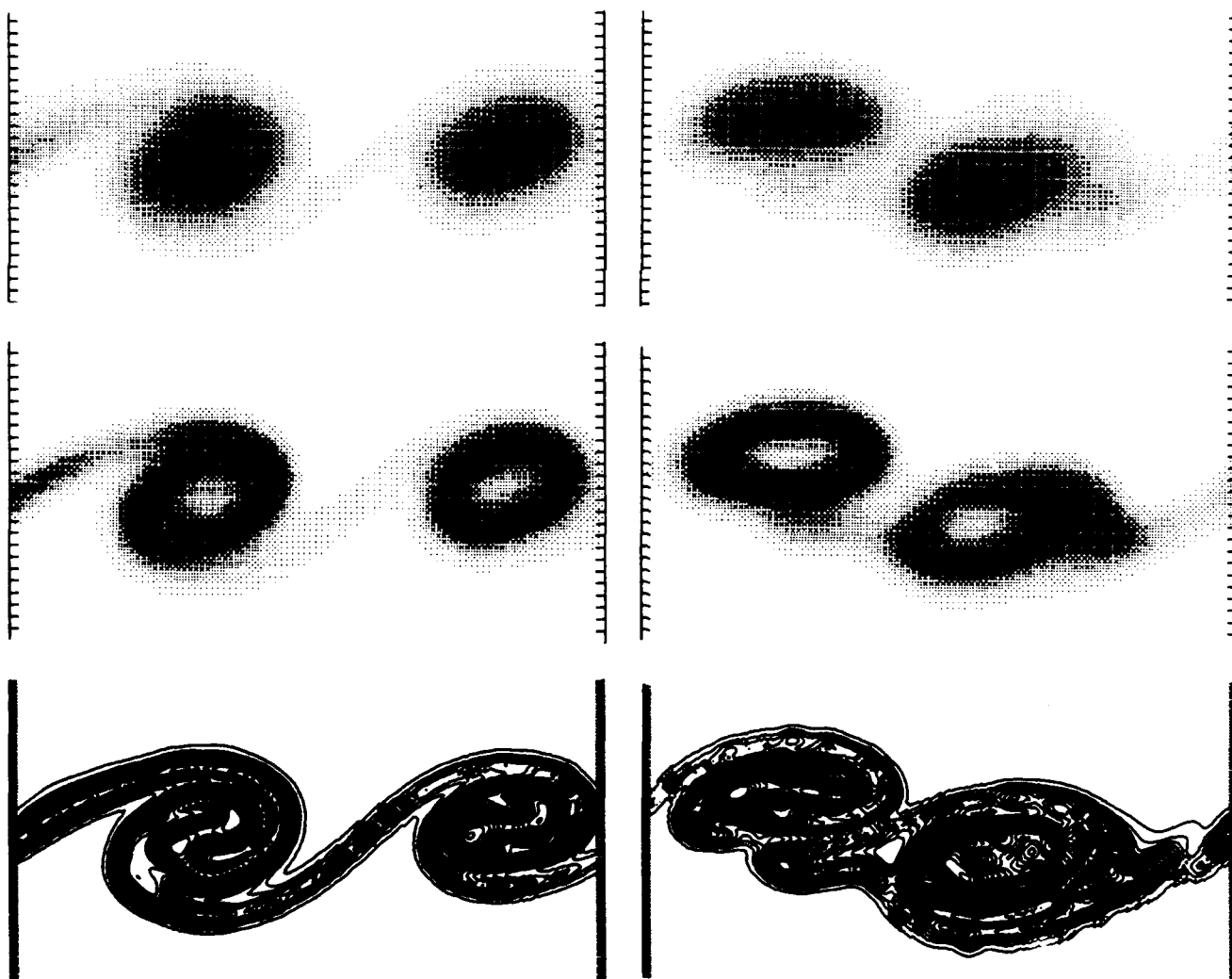


Figure 6. From top, the product mass-fraction, reaction rate and vorticity for the reacting shear layer at  $A_f = 50$  and  $Q = 6$  for the uniform density case, shown for  $1.43 < x < 2.43$  (left) and  $2.45 < x < 3.45$  (right). In all cases  $0.25 < y < 0.75$ .

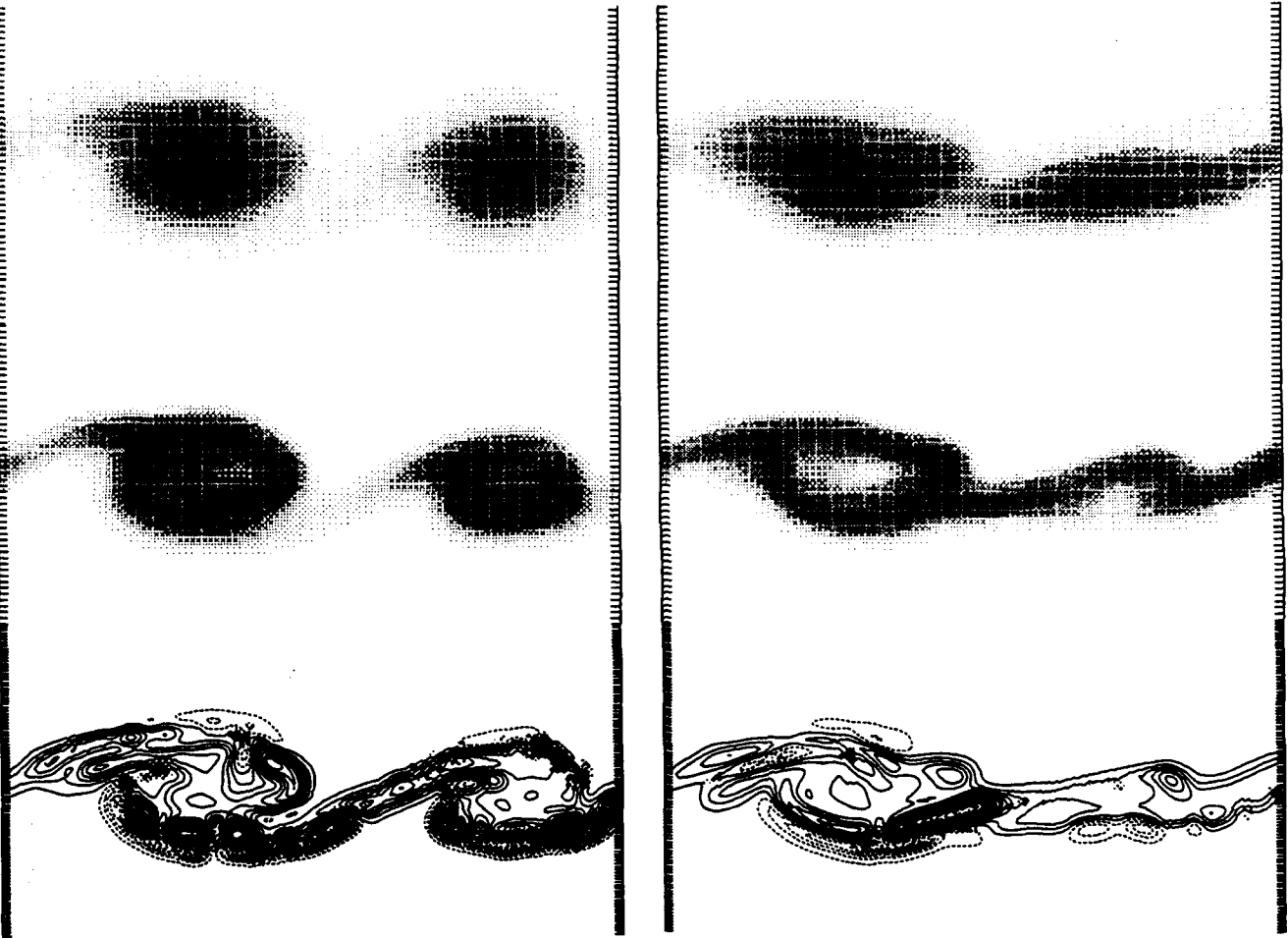


Figure 7. From top, the product mass-fraction, reaction rate and vorticity for the reacting shear layer at  $A_f = 50$  and  $Q = 4$  (left) and  $Q = 6$  (right). The results are shown for  $1.43 < x < 2.43$ . In all cases  $0.25 < y < 0.75$ .

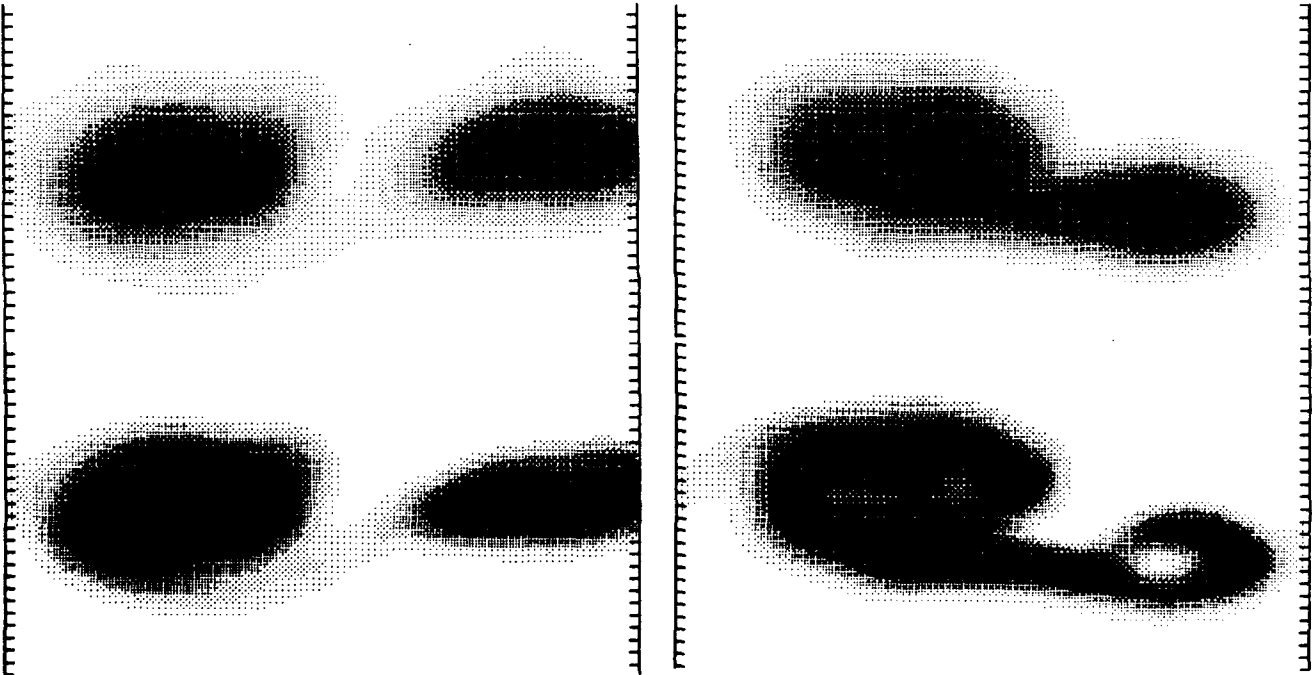


Figure 8. from top, the product mass-fraction and reaction rate for  $Q = 4$  and  $A_f = 50$  (left) and  $A_f = 100$  (right). The results are shown for  $2.82 < x < 3.82$ . In all cases  $0.25 < y < 0.75$ .